Universidade de Santiago de Compostela

Departamento de Física de Partículas

A complete method to obtain the energy spectrum of inclined cosmic rays detected with the Pierre Auger Observatory.

Víctor Manuel Olmos Gilbaja

Santiago de Compostela, marzo - 2009

Universidade de Santiago de Compostela

Departamento de Física de Partículas

A complete method to obtain the energy spectrum of inclined cosmic rays detected with the Pierre Auger Observatory.

Memoria presentada para optar
al Grado de Doctor en Física por
D. Víctor Manuel Olmos Gilbaja

Santiago de Compostela, marzo 2009

Fdo. Víctor Manuel Olmos Gilbaja

D. Enrique Zas Arregui, catedrático de Física Teórica del Departamento de Física de Partículas de la Universidad de Santiago de Compostela.

CERTIFICA

que la memoria titulada "A complete method to obtain the energy spectrum of inclined cosmic rays detected with the Pierre Auger Observatory" ha sido realizada bajo su dirección por D. Víctor Manuel Olmos Gilbaja en el Departamento de Física de Partículas de la Universidad de Santiago de Compostela y constituye el trabajo de tesis que presenta para optar al Grado de Doctor en Física.

Santiago de Compostela a 3 de marzo de 2009

Fdo. Enrique Zas Arregui

A mi niña

Agradecimientos

Después de una revisión bibliográfica entre los agradecimientos de otras tesis doctorales más extensa si cabe que la realizada para llevar a cabo este trabajo que constituye mi tesis doctoral, he encontrado aún más similitudes entre todas ellas en esta sección, que las existentes entre los distintos textos en los primeros capítulos.

Se tiende a agrupar a los seres a los que se siente agradecido de un modo muy similar independientemente del país de origen del espécimen o del sexo del doctorando: pareja, familia, amigos, director de tesis, compañeros de trabajo y agencia financiadora. Así mismo, el motivo del agradecimiento a cada uno de estos colectivos se parece de una manera cuando menos sorprendente. En mi caso, he decido no desentonar demasiado con las referencias bibliográficas consultadas en materia de agradecimientos. Este mismo principio es el que he seguido en el capítulo dedicado al maravilloso mundo del rayo cósmico y al experimento con el cual unos cuantos científicos han decidido aprender algo más sobre ellos, muy a pesar, de que los directores de tesis se empeñen en que innovemos en este capítulo presente en TODAS las tesis sobre temática similar.

Antes de comenzar, me gustaría hacer una aclaración porque la gente tiende a dar mucha importancia al orden en el que aparecen mencionados, por esto quiero dejar claro, que el orden de aparición no tiene nada que ver con la importancia que cada uno de ellos tiene en mi vida. Dicho esto vamos al toro no sin pedir disculpas a la gente de quien me olvide y a aquellos que no sean agradecidos por todo aquello que han hecho por mí.

En primer lugar a mi niña. No existe manera de describir todos los agradecimientos que te mereces, ni lo mucho que te quiero. Por aguantarme, por estar a mi lado, por reírte conmigo y de mí, por ser como eres, por salir y por quedarte en casa, por animarme día a día, mes a mes, por apoyarme siempre y en todo momento en mis decisiones, por los cuatro meses y por el fin de semana de después, por tu habilidad natural con la electrónica, por todo ello y por mucho más.

A mis padres, por su apoyo, por su paciencia, por su graciosa incomprensión sobre mi trabajo, por sus ánimos, por su cariño, por su comprensión y por su apoyo. Por extensión a toda mi familia, abuelos, tíos, primos, suegros, cuãdos, sobrinas,.... por no extrañarse demasiado de seguir a los 30 en la universidad.

A Frodo, Nasa, Pizca y Sombra por esa gran cualidad que tienen los animales de no hablar pero ser capaces de expresarse y por hacer realidad la frase de que cuanto más conozco a la gente más quiero a mis animales. Aprovecho para mencionar a toda la gente que trabaja en la "Fundación Refuxio de Animais" y en la asociación "Abeiro", a ellos no les doy las gracias por lo que haya hecho por mí, sino por lo que hacen por cientos de seres de los que poca gente de acuerda y que se merecen un futuro y una oportunidad. Por su trabajo y su dedicación y porque todo el mundo que ojee esta tesis se decida a adoptar un animalillo (www.refuxio.org).

A mis amigos que nada tienen que ver con la radiación cósmica. A todos ellos les debería escribir otra tesis completa aunque lo más probable, es que dado mi natural despiste, me olvide de casi todo por lo que les estoy agradecido. A Chito, Pedro, Alejo, Gema, Tere, Vero, Manolo y todos los demás por todo el tiempo que me han dedicado, por todos los ánimos que siempre me han dado, por todos los cafés y por esa eterna pregunta de: ¿Y esto de los rayos cósmicos ultraenergéticos para qué sirve?

A todos mis compañeros de trabajo. A mi director de tesis, Enrique, por haberme dado la oportunidad de trabajar para él durante estos 6 años que ha durado la realización de mi tesis doctoral, por todo lo que he aprendido de él que es mucho menos de lo que él ha intentado enseñarme. A los que siempre han estado: Jaime, Ricardo, Ángeles y Gonzalo. A los que estuvieron: Lorenzo, Pedro, David, Patricia, Inés y Gonzaliño. A los que están ahora: Iago, Rodrigo y Alejandra. A todos ellos, por todo lo que me han enseñado y he aprendido, por todos los kilómetros que hemos viajado juntos, por las habitaciones que hemos compartido. Por las discusiones que han dado fruto y por las que han quedado en nada, de todas ellas es fruto esta tesis. En definitiva, por ser grandes compañeros de trabajo. Cómo no mencionar a TODOS los compañeros de despacho que he tenido: Teresa, Diego, Paloma, Tarrío, Anabel, Edu, Lucas, Irais,.... a todos ellos, y a más que han pasado por las mesas de al lado, por haber aguantado mis horas de teléfono, mis conversaciones en voz alta, mis exclamaciones y mis quejas. No habría sido lo mismo sin vosotros. También tengo que mencionar a mis compis del máster, Andrea, María y Elena. Por todos los buenos momentos que hemos pasado juntos, por los malos

y, sobre todo, por lo que nos hemos reído de ellos.

Al personal no docente de la facultad de física de la universidad de Santiago: Merce, Bea, Jorge, Charo, Ana, Vivi, Carmen, Gema, Mercedes, Berta, Mosi y todos cuantos han pasado por el zulo del café. Por tantas risas, por tantos años (alguno ya habríamos devengado un sexenio), por tantos momentos, por tantas críticas y cotilleos fundados o no, por tanto apoyo, por los ánimos, por la comprensión, por los pagos y los anticipos realizados a una velocidad vertiginosa para tratarse de una administración pública. Por todo lo que ya saben.

Al personal del observatorio y a la gente que he conocido durante estos años. A la gente de Karlsruhe, a la de Roma y a Alan por animarte a llegar al final de este camino. A la ficha roja, a la ficha verde, a la ficha azul, a la ficha amarilla, al dado y al cubilete por tantos y tantos comentarios (suscitados). Muy especialmente a la gente de Madrid. Qué habría sido de mí sin Diego y sin su estoica tranquilidad que jamás se ha visto quebrantada y sin María y los "minutos" de chat o de skype o de teléfono directamente. Sin las llamadas cruzadas por intereses mutuos, porque los días grises eran menos grises con los interminables "aaaaaaayyyyyyyyyy" y porque gracias a ellos, viajar a Malargüe no era tanto llegar a Macondo, sino llegar a un lugar de donde traer un buen recuerdo cada vez. Porque además del título de doctor, me llevo algún amigo que otro.

A los daikiris de frutilla, de durazno y de ananá, a la Andes y a la Quilmes, al José Cuervo y al ¿tequila económico?, por estar siempre dispuestos a hacernos olvidar la vida de becario a las tantas de la noche, yendo del observatorio al Turismo. Por permitirnos reír y cantar "Los Pecos" y "Karina" hasta olvidar las horas que llevábamos trabajando.

A Iberia, por tantos kilómetros, por sus retrasos, cancelaciones, pérdidas de equipaje, agresión en pleno vuelo Madrid-Buenos Aires por habernos dado tanto de qué hablar y de qué reírnos y por tener un archivador repleto de reclamaciones sin contestar.

Al Ministerio y a la Xunta, por los dineros aportados a través de múltiples planes y programas que han financiado tanto mi cesta de la compra con la nómina, como la posibilidad de viajar con el pago de dietas, billetes de avión y hoteles.

A TODOS ELLOS Y MUCHOS OTROS, POR ESTO Y POR MUCHO MÁS, **GRACIAS**.

Contents

List of Figures

Chapter 1

Introduction

In 1912, Victor F. Hess found that the rate of discharge of the ionization chambers that he flew on several balloon flights increased with altitude. This observation was interpreted as an evidence that ionizing radiation was continuously reaching the Earth from outer space. From the charge spectrum of this radiation it was shown that nuclei from hydrogen to iron were present in cosmic rays. Moreover, new elementary particles such as positrons, muons or pions were discovered in cosmic rays.

Twenty six years after Hess discovery, P. Auger and collaborators showed that particle cascades of high energy caused the correlated detections of particles at counters widely separated at ground. As low fluxes demand large collection areas, extensive air showers discovered by Auger (and suspected by Rossi two years earlier) allow the detection of Ultra High Energy Cosmic Rays (UHECRs) using the atmosphere as target medium as well as a calorimeter.

To characterize the properties of UHECRs and to enlighten the knowledge about their origin, their chemical composition and their energy spectrum, the Pierre Auger Observatory was born at the beginning of the 1990's. It is a hybrid detector that combines a surface detector array of 1600 Cherenkov water tanks with a fluorescence detector of 24 telescopes to measure with unprecedented accuracy and statistics and with a full sky coverage the extensive air showers initiated by cosmic rays with energies above $10^{18}\ eV$.

The southern site of this observatory is already built in the Argentinian province of Mendoza and has been taking high quality data for more than 5 years. The northern site will be built in the American state of Colorado. The Pierre Auger Observatory

is well suited for the detection of inclined showers because the water Cherenkov tanks used in the surface detector act like volume detectors. The transverse area of $4.3\ m^2$ for completely horizontal showers is enough to detect particle fluxes at relatively large distances from the shower axis. Besides, the fact that the number of stations within a given distance to shower axis rapidly increases as the zenith angle rises above $60°$, improves the capacity of detecting inclined showers.

The present work is devoted to the analysis of inclined air showers detected by the surface detector of the Pierre Auger Observatory and to determine the flux of UHECRs. It is presented as a complete guide of the reconstruction procedure of inclined events, so my contributions are sometimes merged with the contributions of other people to give a global view of the whole procedure. For this reason I will briefly point out how my main contributions to obtaining the energy spectrum fit in the general overview of this project which has taken over ten years.

The first analysis of inclined showers was done for the Haverah Park data in 2000 by M. Ave *et al.* [1]. A FORTRAN code was developed to analyze inclined showers being called *"efit"*. Some predictions about the Auger Observatory were already done at that time. A new C++ code was developed within the USC astroparticle physics group coordinated by R. Váquez for the analysis of inclined air showers detected by the surface detector of the Pierre Auger Observatory. This code was based on the older FORTRAN version but it includes all the works developed within the group during those years. For instance, the time model for the propagation of muons of the shower done in L. Cazón PhD thesis [2], a new set of the profiles of the muon density at ground and the simulation of the response to crossing muons of the Auger surface detector tanks done by G. Rodríguez in his PhD thesis [3] and the parameterizations of the electromagnetic signal in inclined showers derived by I. Valiño as a part of her doctoral work [4].

All these previous works established the basis of the next step towards the measurement of the energy spectrum of cosmic rays using inclined events, the energy calibration. This calibration between the shower size as measured by the surface detector and the calorimetric energy measurement performed by the fluorescence detector has been one of my main contributions to the estimate of the cosmic ray flux using inclined events, being the first energy spectrum of inclined cosmic rays based on this calibration presented in the collaboration meeting of November 2005 [5]. This has been followed up steadily since then and I have contributed significanly to this task in which the group of USC

has played a prominent role.

Besides the energy calibration, the exposure is a crucial ingredient to obtain the energy spectrum. I have detemined the energy saturation of the trigger efficiency following one of the approaches already used in the analysis of vertical events using hybrid events with a zenith angle over 60°. Above this threshold, the exposure can be calculated from geometrical arguments and related to the work done by another analysis group of the Pierre Auger Observatory [6].

Apart from my contributions to the measurement of energy spectrum using inclined showers, other of my contributions to the analysis of inclined cosmic ray events are the checks of the model for the arrival time variance using twin tanks, the collaboration with the software development and bug fixing of the *"efit"* program or the development of the first seed of the code ported to the offline which I did in collaboration with J. González and M. Roth during a stay within the Karlsruhe group that ended with a presentation of the first inclined spectrum within the offline framework in the Chicago analysis meeting in 2006.

The thesis is organized as follows: In chapter 2 a brief introduction to the cosmic rays and to the extensive air showers as well as a description of both detectors of the Pierre Auger Observatory are given. The latest published results of the Pierre Auger collaboration are briefly discussed. In chapter 3 we describe the general procedure for the reconstruction of the incoming direction of the detected inclined showers. The time model that it is used to describe the shower front and to obtain the variance on the measurement of the start time is presented. Making use of the data collected in twin stations, the time variance is shown to describe data with a high accuracy. In chapter 4, the algorithms for the reconstruction of the impact point and of the energy are presented. Two methods are applied consecutively: a minimum χ^2 procedure and a maximum likelihood method. The inputs for both of them, such as the tank response to muons or the electromagnetic contribution to the total signal are also discussed. In chapter 5, the energy spectrum of UHECRs is obtained. Firstly we obtain the acceptance of the surface detector to inclined events assuming that above the energy of trigger saturation the exposure of the array is completely geometrical. From the files containing the information on the trigger rate, its active area each second is computed and adding these areas for the whole period of data taking the exposure to inclined events is obtained. Once the exposure is obtained, the flux is directly calculated from the data. Finally in

chapter 6, main conclusions of this thesis are presented.

Bibliography

[1] M. Ave, R. A. Vázquez & E. Zas, Astropart. Phys. **14** (2000) 91.

M. Ave, R. A. Vázquez, E. Zas, J. A. Hinton & A. A. Watson, Astropart. Phys. **14** (2000) 109.

[2] L. Cazón PhD Thesis, "Modelling the muon time distribution in extensive air showers", Universidad de Santiago de Compostela (2004).

[3] G. Rodríguez-Fernández PhD Thesis, "Horizontal air showers at the Pierre Auger Observatory", Universidad de Santiago de Compostela (2007).

[4] I. Valiño PhD. Thesis, "Detection of Horizontal Air Showers and Neutrino induced Showers with the Pierre Auger Observatory", Pierre Auger Collaboration Internal Document, GAP Note 2008-024.

[5] N. Busca, V.M. Olmos-Gilbaja, P. Privitera, G. Rodriguez, R.A. Vazquez & E. Zas, "An estimate of the cosmic ray spectrum using inclined data of the Pierre Auger Observatory", Pierre Auger Collaboration Internal Document, GAP Note 2006-025.

[6] Acceptance working group. ipnweb.in2p3.fr/ auger/AugerProtected/AcceptWork.html

Chapter 2

Cosmic rays and extensive air showers: their detection, the Pierre Auger Observatory and its recent results

In this chapter a general review of cosmic rays and their detection is given. After a description of the Pierre Auger Observatory, several of its most recent results are presented.

2.1 Cosmic rays and extensive air showers

Cosmic rays are the particles that reach the Earth from all directions in the space and with an energy spectrum that spans for more than ten orders of magnitude (fig. 2.1). Almost 100 years ago, Victor H. Hess flying a balloon to more than $5\ km$ high, discovered that the ionization of the air increases with altitude, explaining this fact with the entrance of penetrating radiation into the atmosphere [1]. This discovery was awarded with the Nobel prize in 1936. The name of cosmic rays was given to this radiation by R. Millikan after several experiments which tried to disprove Hess results.

Even now, several features related to cosmic rays such as the tail of its energy spectrum, their production mechanisms and their sources or their composition are still

unsolved. This three features affecting the ultra high energy cosmic rays are being investigated by the Pierre Auger Observatory.

2.1.1 General features of cosmic rays

The energy spectrum of cosmic rays over more than ten orders of magnitude follows almost a simple power law:

$$\Phi = \frac{dN}{dE} \propto E^{-\gamma} \tag{2.1}$$

Some of the features of this spectrum and the deviations from a simple power law become evident multiplying the flux by a power of energy. In fig. 2.1 the flux times $E^{2.7}$ is shown as measured by different experiments (taken from [2]). The main deviations from a simple power law are "the knee" at $\approx 3 \cdot 10^{15}\ eV$ where the spectrum turns steeper and "the ankle" at $\approx 5 \cdot 10^{18}\ eV$ where the spectrum flattens.

These two changes in the spectrum shape can be explained with changes on the acceleration mechanisms, changes in the hadronic interaction models, changes in the composition of the cosmic rays or some propagation effects. Some interpretations of these features in the energy spectrum of cosmic rays can be found in [3].

The UHECR flux has been measured with two techniques. Detectors such as Fly's Eye [5] or HiRes [6] use fluorescence telescopes while experiments as Volcano Ranch [7], Haverah Park [8], SUGAR [9], Yakutsk [10] and AGASA [11] are arrays of particle detectors at ground. The tail of this energy spectrum is a very hard region to study due to the systematic uncertainties of energy measurement and to the low available statistics because of the extremely low flux. Measurements in this energy range before Auger observatory analysis were compatible within their uncertainties but two trends were present. The first one reported by the AGASA collaboration was a continuation of the energy spectrum as a power law [11]. The second one given by the HiRes collaboration was a flux suppression above $5 \cdot 10^{19}\ eV$ [12]. At the beginning of the nineties J. Cronin and A. Watson proposed to build an observatory to measure the UHECR flux with unprecedent precision and statistics: The Pierre Auger Observatory [13]. The first result of the Auger observatory in this subject is commented in section 2.4.1.

The power law behavior of the energy spectrum is expected from stochastic acceleration processes as first proposed by Fermi [14] in which the particles are accelerated

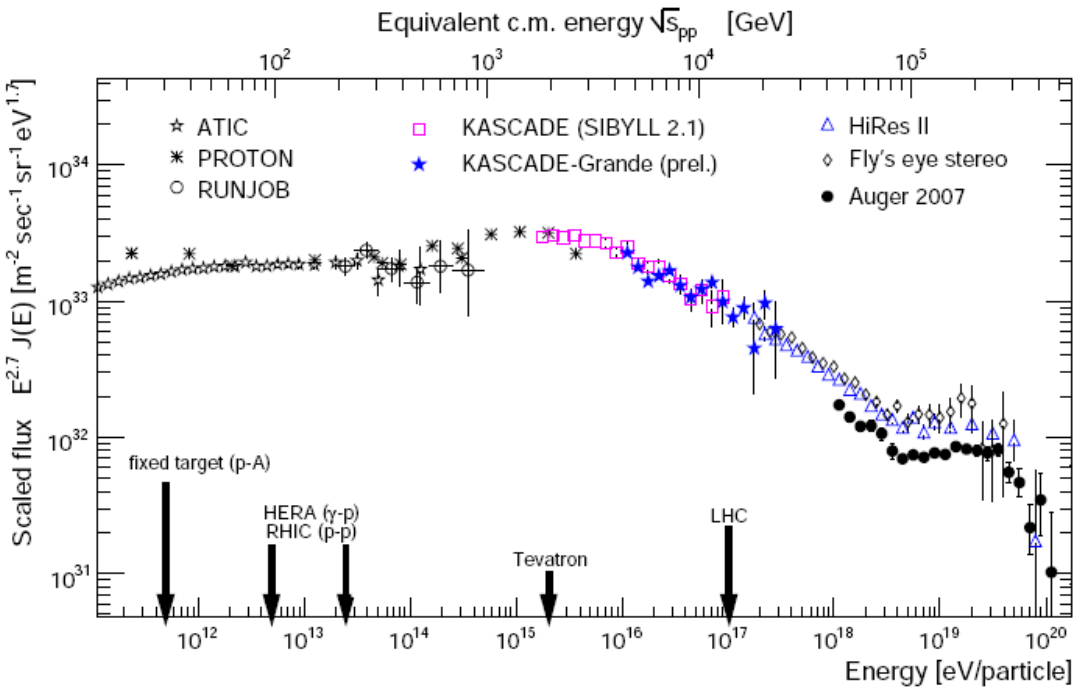

Figure 2.1: Cosmic ray energy spectrum as measured by several experiments over a wide range in energy [4]. The flux is multiplied by $E^{2.7}$ to emphasize its structures. The knee at several PeV, the ankle around $\approx 3\ EeV$ and the cutoff above $\approx 50\ EeV$ can be very clearly seen. While the lower axis reflects the energy of the primary cosmic ray nuclei, the upper axis denotes the corresponding center-of-mass energy per nucleon. Some typical energies, which can be accessed by accelerators, are emphasized.

through interactions with magnetic plasmas. The maximum achievable energy through this mechanism depends on the magnetic field strength and on the size of the region the acceleration takes place in. Hillas provided an argument based on the size and on the strength of magnetic field to show that very few sources could accelerate cosmic rays up to measured energies of more than $10^{20}\ eV$ [15]. The argument is based on the requirement that the Larmor radius of the accelerated particle must be at the most half the size of size of the accelerating region:

$$E_{max}[EeV] \leq \frac{\beta Z}{2} BL[\mu G\ kpc] \tag{2.2}$$

where E_{max} is the maximum energy that a particle of charge Z can reach being ac-

celerated in a region with a magnetic field B and with a characteristic size L. β is a characteristic speed of the accelerating region as a fraction of the speed of light.

The Hillas plot shown in 2.2 gives the value of B versus L for several candidate objects to accelerate ultra high energy cosmic rays through this acceleration mechanism. Only objects above the diagonal lines which depend on the charge of the particle to be accelerated and on the energy, are able to accelerate that particles above the considered energy.

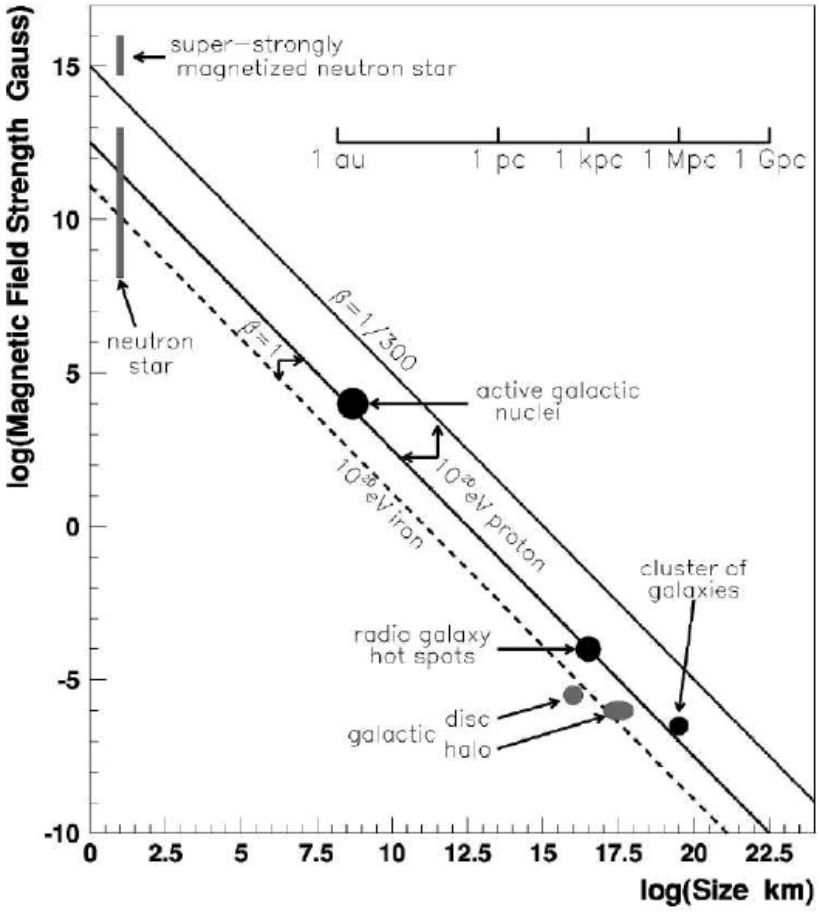

Figure 2.2: Hillas plot of possible accelerating sources. Objects below the diagonal lines are excluded as possible sources. The dashed line corresponds to the acceleration of a 10^{20} eV iron nuclei while full lines correspond to 10^{20} eV protons with $\beta = 1$ and $\beta = 1/300$ as indicated.

As cosmic rays propagate through the space from their production points, they suffer many interactions that affect their energy as well as their direction of movement. After the discovery of the cosmic microwave background by Penzias and Wilson in 1965 [16], Greisen, Zatsepin and Kuzmin pointed out that protons with energy above $5 \cdot 10^{19}\ eV$ should interact with the photons of the microwave background losing part of their energy [17]. Consequently there will be a limit on the distance to the Earth of the sources of ultra high energy cosmic rays. In the left panel of fig. 2.3 we can see how protons lose part of their energy as they propagate through the microwave background. Protons with an energy over $10^{20}\ eV$ are not expected to propagate more than $\approx 100\ Mpc$ before losing this energy level.

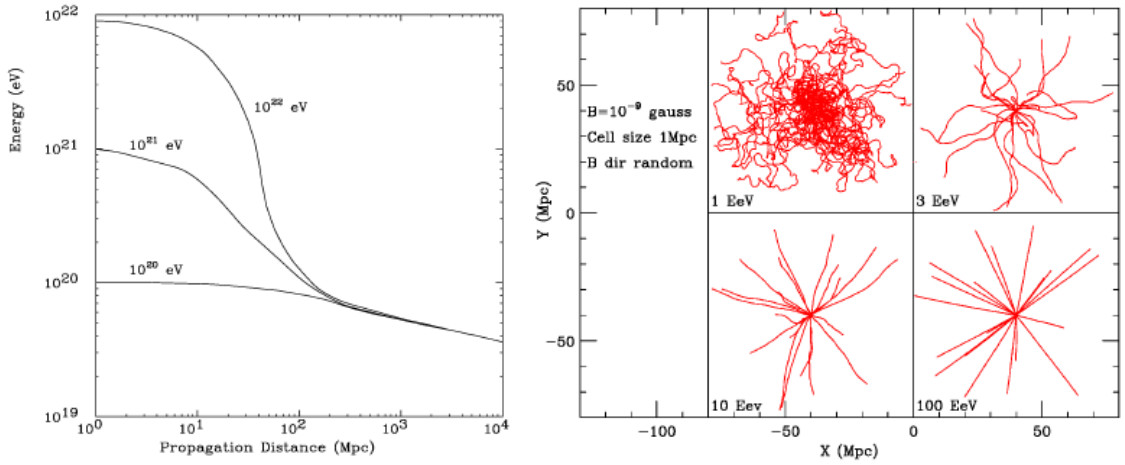

Figure 2.3: Left panel: Energy of protons as a function of the distance traveled through the microwave background for three different initial energies (taken from [18]). Right panel: Trajectories of 20 protons of four energies propagating up to 40 Mpc from the source in a magnetic field of $1\ nG$ (taken from [19]).

If the distance to the sources of this kind of ultra high energy protons is limited to tens of Mpc, their paths are not likely to be much deviated from their direction by galactic or extragalactic magnetic fields and hence they could point back to their production point as it is shown in the right panel of fig. 2.3. This feature would make possible the identification of sources.

Heavy nuclei will also lose their energy not only due to interactions with the cosmic

microwave background but also with the infrared background. The distance of production points of nuclei with energy above $10^{20}\ eV$ is reduced also to $\approx 100\ Mpc$ [20].

The interactions of cosmic rays with background radiation during their propagation from their sources to the detection point at the Earth, have a direct effect in the energy spectrum. The observed flux should suffer a great reduction beyond $E_{GZK} \approx 5 \cdot 10^{19}\ eV$. This expected suppression is often referred to as the GZK cutoff. The evidence of events above the limit imposed by the GZK effect proves that if it exists, the spectrum should not cut off sharply but it should present a smooth suppression.

The GZK effect also implies a nearby origin for particles with energy above the GZK cutoff. If the distance to their sources is limited to several tens of Mpc, charged particles of energies above E_{GZK} should traverse cosmic magnetic fields with little deviation and in consequence they should point back to their sources. Such cosmic ray astronomy would make possible to identify the sources with known astrophysical objects or to establish the existence of new sources which are not visible at lower energies.

2.1.2 Extensive air showers

In 1934, Rossi noticed that the coincidences between several counters exceeded the expected rate from pure chance coincidences [21]. In 1938, Pierre Auger and collaborators, after a systematic investigation, discovered *extensive air showers* (EAS) [22] which are huge cascades initiated by cosmic rays when they enter the Earth's atmosphere. Due to the very low flux of high energy cosmic rays, EAS are the only way they can be observed because using EAS, the effective area of detection is orders of magnitude larger than that of detectors that can be flown on balloons or satellites.

When the primary cosmic ray enters the Earth's atmosphere, it interacts with a nucleus of the air typically in the first $\approx 100\ g\ cm^{-2}$ from the top of the atmosphere. Part of the primary energy is used in the production of secondary particles which acquire transverse momenta traveling with an angle with respect to the direction of the primary particle. If the decay mean free path is longer than the interaction mean free path, the interaction process dominates creating more and more particles of lower energies. Decay can also contribute to the particle creation process. These particles also interact or decay as the cascade propagates in the atmosphere.

For a hadron primary, secondary particles are mainly mesons that may decay into

muons, electrons and photons. It is convenient to group the particles of the air shower into three categories often referred to as *components*: electromagnetic, muonic and hadronic. Neutral pions created during the shower development, almost immediately decay into two photons that initiate an electromagnetic subshower. These cascades from π^0 decays continously feed the electromagnetic component of the shower. Charged mesons produce muons and neutrinos when they decay. Muons form the muonic component while neutrinos go through undetected carrying away a fraction of the primary energy. Finally, the hadrons that have not decayed form the hadronic component of the air shower.

Electromagnetic and hadronic components increase in number of particles reaching a maximum after which the shower size attenuates. The muonic component does not suffer a great attenuation after its maximum as muons lose energy mainly by ionization and not too many are lost by decay. The general features of the air showers development can be easily reproduced with the toy model proposed by Heitler in [23] for pure electromagnetic cascades.

In the schematic diagram of fig. 2.4 each segment represents a particle that at each vertex shares half of its energy with a new particle. Splitting occurs after an interaction length λ. After n interaction lengths the total number of particles is $N(x) = 2^{x/\lambda}$ being the energy per particle $E(x) = E_0/N(x)$ where E_0 is the energy of the first particle. The creation of new particles ends when the average particle energy is below the critical energy E_c. After this point, particles are ignored as they are more likely to lose energy, be absorbed or decay.

The maximum number of particles within this model is $N(x_{max}) = E_0/E_c$ being reached at $X_{max} = \lambda \frac{ln(E_0/E_c)}{ln2}$. The basic features of this model which hold for electromagnetic cascades and also approximately for hadronic showers are:

$$N_{max} \propto E_0 \;\; and \;\; X_{max} \propto ln(E_0)$$

Electromagnetic cascades

The theory of electromagnetic cascades was developed at the end of the thirties after the discovery of the positron in 1932 [24]. The processes that dominate electromagnetic showers are pair production and bremsstrahlung and their behavior can be described quite accurately in terms of quantum electrodynamics. For particles with energies greater than

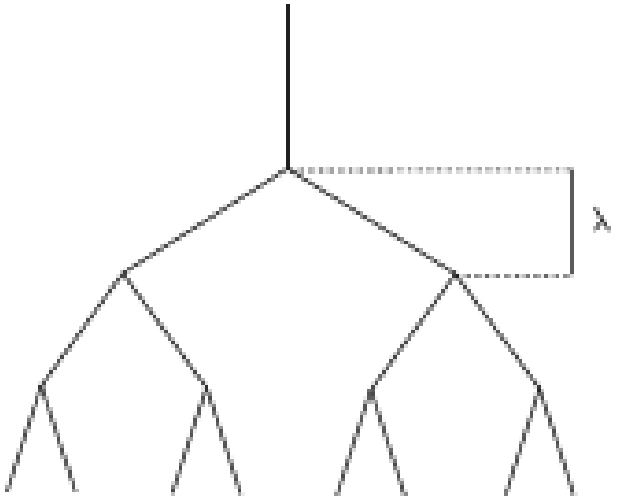

Figure 2.4: Heitler model for the development of electromagnetic cascades. After an interaction length λ each particle (straight line) creates a new one sharing half of its energy with it.

their critical energy in air, collision losses and Compton scattering can be neglected.

High energy photons interact with an air nucleus creating an electron-positron pair. Electrons emit high energy photons by bremsstrahlung which produce again more electron-positron pairs. At each stage of the shower, the number of particles increases while the energy per particle decreases.

With several approximations to solve the cascade equations, the total number of charged particles for an electromagnetic shower initiated by a photon of energy E_0 as a function of depth t in units of radiation lengths is given by the Greisen formula [25]:

$$N_e(E_0, t) = \frac{0.31}{\beta_0^{1/2}} e^{t(1-\frac{3}{2}\ln(s))} \tag{2.3}$$

where $s \approx \frac{3t}{t+2\beta_0}$ is called the *age* of the shower, $\beta_0 = \ln(E_0/\epsilon_0)$ and ϵ_0 is the critical energy. Shower maximum is reached at $s = 1$, the number of particles grows for $s < 1$ and decreases for $s > 1$. This formula is an approximation of the average shower behavior and individual showers behave differently due to fluctuations in the interaction point and in the shower development.

The lateral spread of the shower particles depends on the transverse momentum transmitted to the secondary particles created by pair production or bremsstrahlung and

particularly on the Coulomb scattering of electrons (multiple elastic scattering). An approximate solution for the *lateral distribution function* (LDF) of electrons at a depth t is given by the NKG formula [25,26]:

$$\rho_e(r,t) = N_e(t)\frac{C(s)}{r_1^2}\left(\frac{r}{r_1}\right)^{s-2}\left(1+\frac{r}{r_1}\right)^{s-9/2} \tag{2.4}$$

where N_e is the total number of electrons, $C(s)$ is a normalization coefficient, s is the age of the shower and r_1 is the Molière length in units of radiation lengths from the theory of multiple scattering.

The differences of the electromagnetic component of a shower initiated by a hadron with a pure electromagnetic cascade are quite subtle. Gaisser and Hillas proposed in [27] a parameterization for the number of electrons at a depth X initiated by a hadron as:

$$N_e(X) = N_{max}\ \left(\frac{X-X_0}{X_{max}-X_0}\right)^{\frac{X_{max}-X_0}{\lambda}}\ exp\left(\frac{X_{max}-X}{\lambda}\right) \tag{2.5}$$

where N_{max} is the number of particles at the shower maximum, X_{max} is the depth of the shower maximum in $g\ cm^{-2}$, and X_0 and λ are parameters that depend on the point of first interaction and on the shower development.

Regarding the lateral spread of the electromagnetic component of an extensive air shower initiated by a hadron, the NKG function stated in eq. 2.4 is a reasonable approximation to it. However, different exponents are given from experimental measurements of the LDF that can not be described by just one age parameter.

The muonic component and inclined cascades

The muonic component that accounts for $\sim 10\%$ of the total number of particles in an extensive air shower is due to the decay of charged pions and kaons according to the following decay modes:

$$\pi^{\pm} \rightarrow \mu^{\pm} + \nu \tag{2.6}$$

$$K^{\pm} \rightarrow \mu^{\pm} + \nu \tag{2.7}$$

$$\rightarrow \pi^{\pm} + \pi^0 \tag{2.8}$$

As muons travel practically in straight lines from their production points, the lateral spread of the muonic component is mainly due to the transverse momentum of the parent pions and kaons. This lateral spread has a dependence on the energy as the opening angles for mesons are smaller for high energy particles. There is no standard parameterization for the LDF of muons as there is the NKG formula for the electrons. In any case, one of the first LDF for muons as a function of the depth t was also given by Greisen in [28]:

$$\rho_\mu(t,r) = N_\mu(t) \left(\frac{r}{r_G}\right)^{-0.75} \left(1+\frac{r}{r_G}\right)^{-2.5} \tag{2.9}$$

where $r_G = 320\ m$ plays a similar role than the Molière radius. As this value is greater than the Molière unit for electrons ($\approx 100\ m$), muons spread to larger distances from the shower core than electrons, being the main part of the particle density at large distances to the core.

Besides its importance at large distances from the shower core, the muonic component becomes crucial for inclined showers. The grammage that a shower must cross before hitting the ground at the southern site of the Pierre Auger Observatory varies from $\approx 880\ g\ cm^{-2}$ for a completely vertical shower to $\approx 1760\ g\ cm^{-2}$ for a 60° zenith shower.

After the shower maximum the electromagnetic component is rapidly attenuated in the atmosphere as it is shown in fig. 2.5 while the attenuation length for the muonic component is much larger. For horizontal showers, the muonic component dominates at ground level because of the absorption of the electromagnetic cascades from π^0 decays [29]. However, there is still an electromagnetic component due to muon decay and hard muon interactions. This component follows the behavior of the muonic one as also shown in fig. 2.5.

For this reason, the muonic component and the muonic signal are crucial for the reconstruction of inclined showers with a surface detector as the main part of the signal is due to the muons at ground.

2.2 Detection techniques of extensive air showers

Array of detectors

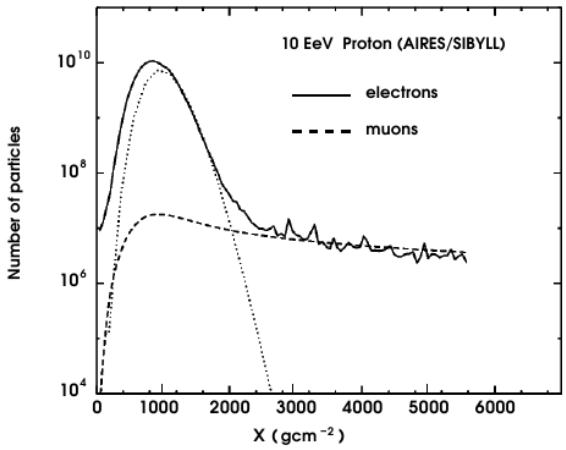

Figure 2.5: Longitudinal development of the muonic and electromagnetic components of an extensive air shower of $10^{19}\ eV$. From $\approx\ 2500\ g\ cm^{-2}$ the electromagnetic component is due to muon decay.

The first technique used to detect extensive air shower and the one they were discovered with, is to sample the secondary particles of the shower when they reach the ground with an array of detectors.

When a shower triggers an array of detectors, the particle densities and the arrival times in all detectors are registered. The shower arrival angle is generally obtained by fitting the arrival times of the shower particles to a shower front moving at the speed of light. The shower energy is obtained comparing to shower simulations of the signals produced in each detector. One of the biggest problems analyzing data from arrays of particle detectors is the need to use simulations. These require assumptions about the nature of the primary cosmic ray and also about the behavior of interactions at energies well beyond those being explored with current particle accelerator experiments. The latter are usually made by choosing a given model for hadronic interactions. These are large inherent uncertainties associated to the simulations because of these unknowns. On the other hand, their duty cycle of $\sim 100\%$ is essential to gain the enough statistics needed to study the very low flux of high energy cosmic rays.

Fluorescence telescopes

The detection of the nitrogen fluorescence was proposed to follow the longitudinal development of extensive air showers in [30]. The idea is to detect the isotropic nitrogen

fluorescence light emitted by the deionization of these air molecules that get ionized at the passage of the air shower.

Every electron of the shower produces in average about 4 fluorescence photons per meter so only high energy showers with a huge amount of electrons produce enough light to generate a detectable signal. Emitted photons have wavelengths between $300\ nm$ and $400\ nm$ corresponding to energies of the transition levels of the nitrogen molecule. This detection technique also requires a clean atmosphere and a moonless nights for operation.

The arrival direction of the showers is determined from the timing measurements and with the information of the pointing direction of the light detection system. The integral of the total light emitted along the longitudinal profile is a measurement of the energy of the shower though several corrections have to be made to take into account the attenuation of the light in the atmosphere due to absorption and scattering processes.

2.3 The Pierre Auger Observatory

The Pierre Auger Observatory has been designed as a hybrid detector to take advantage of both techniques and to reduce systematic effects due to any of them. An example of the relative strengths are the high statistics provided by the array of detectors with its large detection area and its almost 100% duty cycle and the nearly calorimetric measurement of energy of the fluorescence telescopes.

Besides combining the strengths of each detection technique the hybrid approach provides some new features as the intercalibration of energy measurements with each technique, the enhancement of the sensitivity to composition and a better resolution in the determination of the arrival direction of the detected air showers.

In the next sections, each of the detectors that constitute this hybrid observatory is briefly described. To maximize the hybrid performance, the fluorescence detector eyes are placed at the edges of the surface detector array as shown in fig. 2.6, allowing the detection of the events by the two techniques simultaneously. All showers above $E \approx 8 \cdot 10^{18} eV$ that fall inside the surface detector area when the fluorescence detector is active are detected by the two techniques simultaneously. Events which are recorded and can be reconstructed with both techniques deserve a special consideration because they are the key for intercalibration of the energy measurements. They are referred to

as *Golden Hybrid Events*. One of these events is shown in fig. 2.7.

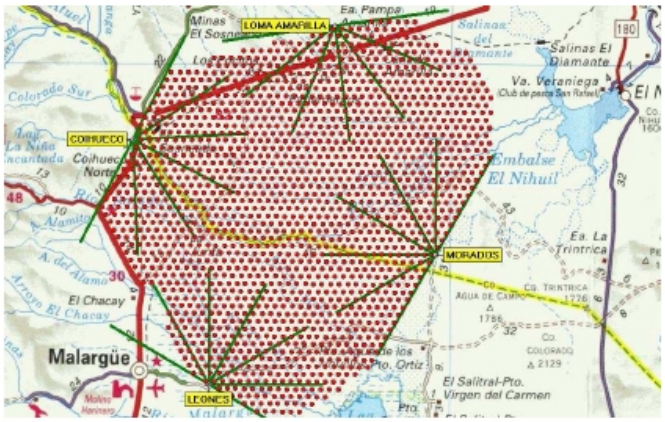

Figure 2.6: Layout of the hybrid detector of the Pierre Auger Observatory. Red dots are the stations of the surface array. The four buildings of the fluorescence detector are also shown.

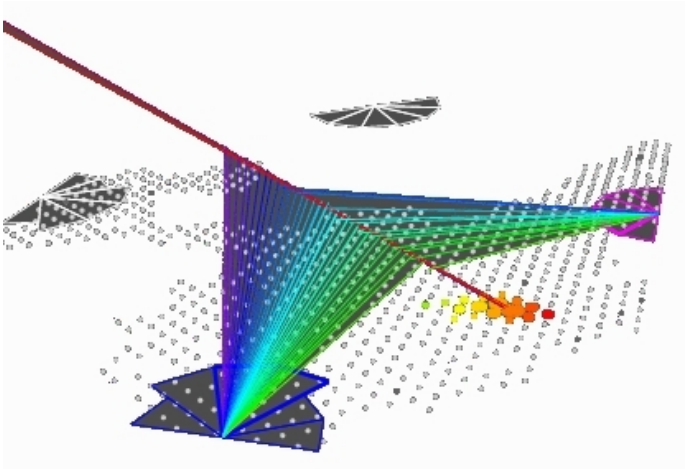

Figure 2.7: Golden hybrid event detected simultaneously with the fluorescence and surface detector techniques. Seventeen SD tanks are triggered by the shower. The event is also "stereo" because it is detected with two eyes of the fluorescence detector.

2.3.1 The Fluorescence Detector

Description of the Fluorescence Detector

The Fluorescence Detector of the Pierre Auger Observatory is a set of four "eyes" each one housing six telescopes which are enclosed in a building. Each telescope has a field of view (FoV) of $30°$ in azimuth x $28.6°$ in elevation between $2°$ and $30.6°$ above the horizon. One of the buildings is shown in fig. 2.8.

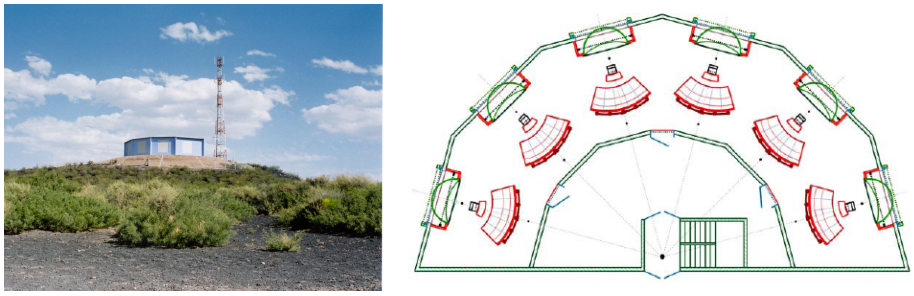

Figure 2.8: Picture (left) and schematic view (right) of "Los Leones", one of the four buildings that constitute the fluorescence detector. The six telescopes are also shown in the schematic view.

The telescopes, as the one shown in fig. 2.9, use adapted Schmidt optics to achieve a high optical quality in the whole FoV reducing the coma aberration [32]. Each telescope consists of an aperture system, a spherical mirror ($3.4\ m$ curvature radius) and a camera with 440 photomultipliers (PMTs) placed at the focal surface [33].

Fluorescence light enters the telescope through a $0.85\ m$ radius diaphragm equipped with a corrector ring to increase the effective radius to $1.1\ m$ [34]. After traversing an UV filter to remove much of the sky light background. The light is focused onto the camera by a $3.5\ m$ x $3.5\ m$ spherical mirror.

The camera, described in [35] and shown in the left panel of fig. 2.10, is an array of 440 hexagonal PMTs placed at the telescope focal surface. To adapt the camera to the spherical focal surface, a honeycomb configuration has been adopted arranging the PMTs in a 22x20 matrix. Each pixel of the camera has a FoV of about $1.5°$. Due to the spacing between PMTs and to the inefficiency of the region of contact between adjacent PMTs, a system of 'Wiston cones" [36] complements the PMTs at the camera to optimize the

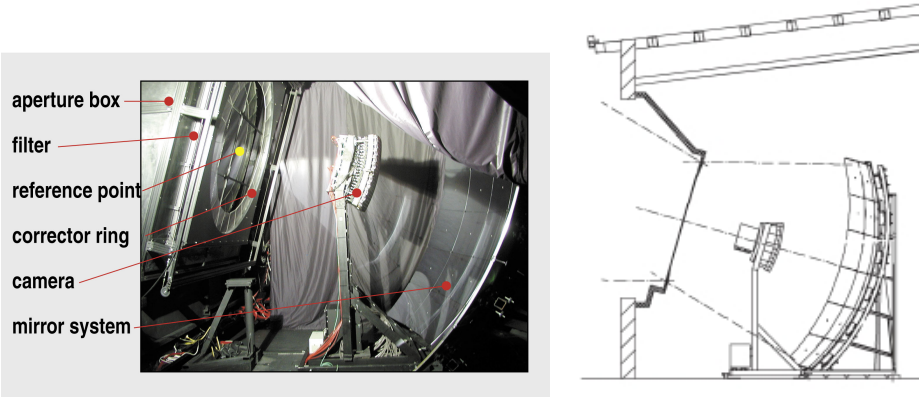

Figure 2.9: Picture (left) and schematic view (right) of one of the fluorescence telescopes.

light collection. The unit element of this system is the so-called "mercedes" star shown in the right panel of fig. 2.10 which has been shown to increase the light collection efficiency from 50% up to 93% [37].

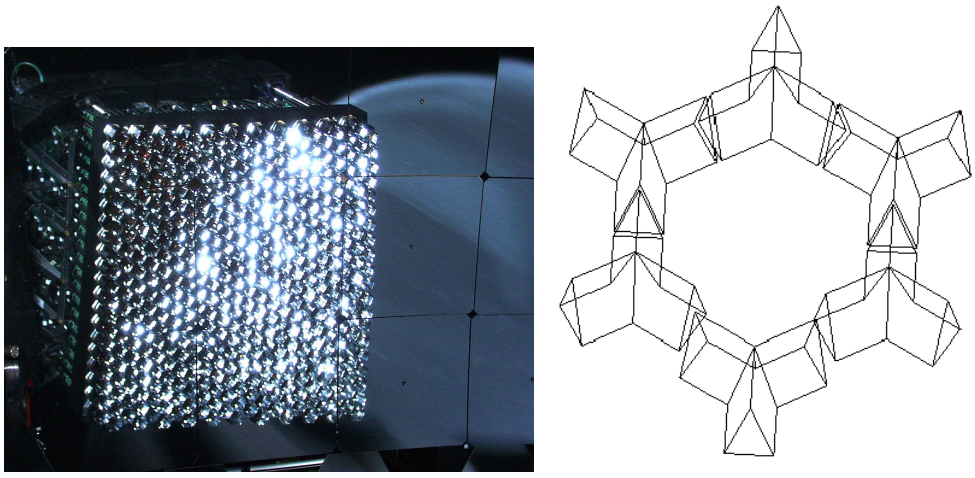

Figure 2.10: PMT camera (left) and mercedes ring (right).

Trigger levels

The trigger system of the fluorescence detector is a four level trigger described in [38,39]. The first level trigger is located on the front-end board and makes decisions at the PMT

or pixel level. The pixel is marked as triggered if the collected signal in the last 10 bins exceeds an adjustable threshold. This mark lasts for $20\ \mu s$ to allow the search of coincidences between pixels. The threshold for decision is tuned continuously to achieve a trigger rate of $100\ Hz$.

The pixel triggers are bussed into the second level trigger board which generates a trigger if the pattern of triggered pixels looks like a straight track generated by the fluorescence light of an extensive air shower. Five predefined patterns are regarded as straight tracks. The rate of this trigger is about $0.1\ Hz$ per mirror.

The third level trigger is implemented in software and searches for time correlation within the pixel tracks that have fired the second level trigger. The rate of this trigger is at the level of $0.02\ Hz$ per mirror. Every time a third level trigger occurs all the data of triggered pixels and of their neighbors are stored in a so-called "Eye-PC" that merges different mirror triggers that might correspond to the same event.

The eye PC performs a preliminary event reconstruction of the arrival direction and of the time of impact of the shower. Pixels with a high χ^2 contribution are removed and events with more than four pixels remaining are selected as T3. The arrival time is then sent to the CDAS to allow the hybrid detection by the collection of all SD data within a time window of $120\ \mu s$ centered in the T3 trigger time.

Calibration and monitoring of the Fluorescence Detector

The objective of any calibration procedure is to convert the measured ADCs counts into light flux. An absolute calibration procedure is performed using a calibrated diffuse light source at the detector aperture [40]. This procedure takes into account the effects of all detector components. The uncertainty is $\sim 12\%$ but it is possible to achieve an uncertainty of $\sim 8\%$ with this method.

The relative calibration procedure described in [41] is based on the distribution of light through an optical fibers system into three different parts of the optical system. The detected charge in each pixel is then compared with the results of the absolute calibration allowing to monitor the timing and gain of each PMT as well as the long and short term stability of the detector.

A cross check of the calibration procedure can be performed using the Central Laser Facility (CLF) [18]. The CLF is a laser station placed at the center of the array firing $355\ nm$ (purity over 99.5%) laser beams. A portion of the emitted laser light is scattered

in the atmosphere and detected by the fluorescence telescopes allowing an end-to-end calibration by the reconstruction of these laser shots as cosmic ray events [43].

2.3.2 The Surface Detector

Description of the Surface Detector

The surface detector of the Auger observatory is an array of detectors arranged in a triangular grid with an spacing of $1500\ m$ and covering an area of $3000\ km^2$ in the Argentinian province of Mendoza. An altitude of $\approx\ 1400\ m$ assures a measurement of the air shower at a shower age close to the maximum of the shower development of UHECR at $10^{19}\ eV$. The mean ground slope of this area is below 1%.

A $1.2\ m$ deep water Cherenkov detector is placed at each node of the grid [44]. These detectors have a higher sensitivity to the electromagnetic component of the showers than scintillators and they also allow the detection of inclined and horizontal showers. Besides, an array of deep water tanks gives twice sky coverage than an array of scintillators allowing full sky coverage with two arrays at appropriate latitudes. One of the 1600 stations that form the surface detector is shown in fig. 2.11.

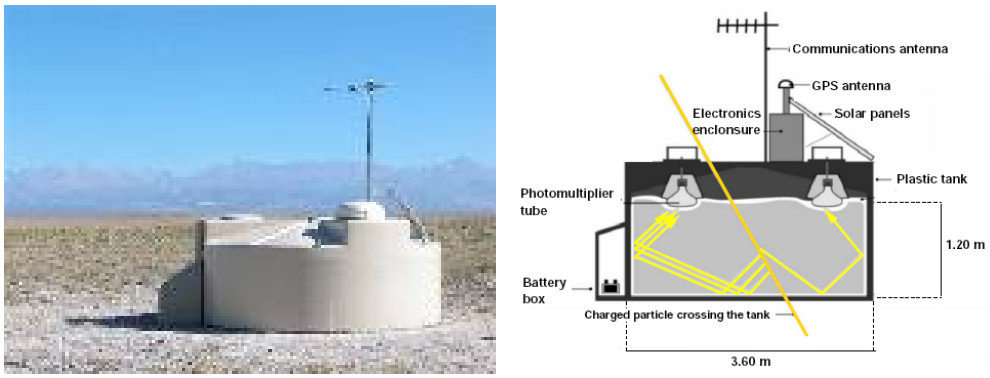

Figure 2.11: Picture (left) and schematic view (right) of a deep water Cherenkov tank of the surface detector.

Each detector is a cylindrical plastic tank with a diameter of 3.6 m and a height of 1.55 m filled with 12000 l of ultra pure water ($\sigma\ \approx\ 7 \cdot 10^{-8}\ \Omega\ m^{-1}$). The water is contained in a Tyvek® liner of 1.2 m depth and viewed by three Photonis XP1805

9" PMTs. From each PMT, two signals are read out and digitized with a 10 bit Flash Analog to Digital Converter in slots of 25 ns: the one from the anode, and the one from the last dynode amplified 32 times. These six signals are sent to a Programmable Logic Device that implements the local trigger conditions.

Each station is also equipped with a commercial GPS, that provides the time of local trigger with an $8\ ns$ uncertainty [45, 46], and with a radio system to communicate and send data to the Central Data Acquisition System [47]. Two $53\ W$ solar panels and a pair of $12\ V$ batteries that supply power to the electronics make each station a stand alone system.

Calibration and monitoring of the Surface Detector

When the particles of the cascade enter a water tank of the array, Cherenkov radiation is emitted. This Cherenkov radiation, which is propagated in the water and diffusively reflected by the liner, is detected by the three PMTs which give rise to an electronic signal.

The signal measured by a given tank may differ from the one measured by another one even if the Cherenkov light is produced in the same conditions. This difference is due, between other factors, to differences in the quality of the water, in the gains of the PMTs, in the Tyvek® reflectivity, in the coupling of the PMT to the water, etc. To make the measured signals independent of the measuring tank, a unit called Vertical Equivalent Muon (VEM_{charge}) is defined as the signal produced in a tank by a vertical crossing muon that travels along the axis of the tank and crosses it completely. The calibration procedure fully described in [48] has to accurately measure the VEM_{charge} for each PMT.

The quite constant flux of atmospheric muons is used to calibrate each tank of the array. The charge histogram of this flux shown in black in fig. 2.12 has two peaks. The first peak is due to detection threshold effects and varies between detectors. The second and larger peak is quite stable with respect to the charge of a vertical crossing muon. This has been measured with muon telescopes [49] and the corresponding histogram is shown in red in the same figure. The position of the second peak has a signal charge which is 1.05 times the VEM_{charge}. By measuring the FADC counts of this peak, all charge signals measured can be easily converted to VEM_{charge} units.

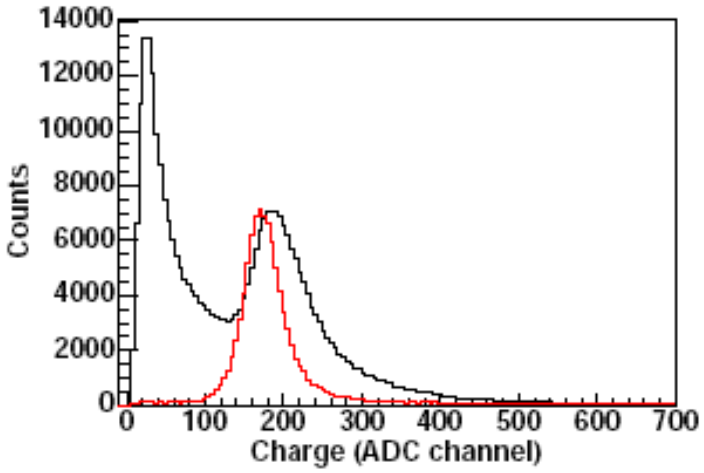

Figure 2.12: Charge histograms of atmospheric muons (black) and of vertical muons (red). Figure from [49].

Once the conversion from "measured charge" to VEM units can be performed, the gains of the PMTs are matched to get a given trigger rate. Every 4 hours the charge histogram of atmospheric muons is made to compute the position of the peak of vertical muons.

Besides the value of the charge of the peak produced by vertical muons, histograms of the maximum values of the FADC traces are also stored. The mean value of these histograms is the VEM_{peak} which is used as reference for trigger levels.

The number of second level triggers produced in each second by each station of the surface array are stored in special files (T2 files). These files are the key to compute the active area of the array counting the unitary cells active every second. Besides, every ten minutes the tank reports to the CDAS the values of sensors of voltages, currents, temperature and trigger levels. An online tool has been developed to monitor the second level trigger rate and the other parameters [1].

[1] http://apcpaox.in2p3.fr/AugerMonitoring/

Trigger conditions

The triggering system of the Surface Detector is designed in a hierarchical way from the local trigger decision made at the tanks ($T1$ and $T2$) to the highest level trigger ($T5$) that ensures a high quality in the reconstruction parameters of the detected air shower [50]. A schematic diagram of the complete trigger chain is shown in fig. 2.13.

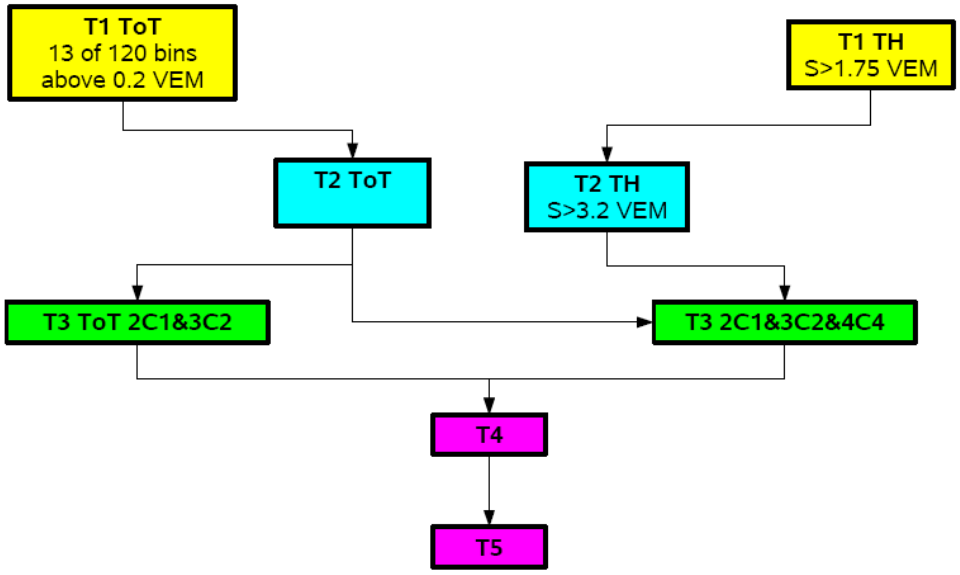

Figure 2.13: Diagram of the trigger chain implemented in the surface detector of the Pierre Auger observatory.

Local triggers

Two levels of local trigger have been set up. These two triggers are implemented in the stations and are defined on a basis of coincidences between signals in the PMTs.

- **First level trigger (T1)**

  This trigger tags stations which could be relevant for shower analysis. It has two implementations, the first one, called *"Time Over Threshold"* (ToT), requires that 13 bins in a window of $120\ \mu s$ are above 0.2 VEM_{peak} in two PMTs. The rate of this trigger is below 2 Hz and it is designed to select small signals spread in time. The second one, called *"Threshold"* (Th), is a 3-fold coincidence between PMTs

with a signal above 1.75 VEM_{peak}. The rate of this trigger is about 100 Hz and it is needed to detect fast narrow signals such as those produced by muons.

- **Second level trigger (T2)**

  Signals that are likely to be part of a detected cascade are promoted to second level trigger and sent to the *Central Data Acquisition System* (CDAS) to check for coincidences between detectors which determine that an extensive air shower has been detected by the array. All of the ToT first level triggers are promoted directly to this second level. The threshold first level triggers are promoted if and only if the measured signal is greater than $3.2\ VEM_{peak}$. The trigger rate is reduced to $20\ Hz$ at the $T2$ level. Only second level trigger tanks are used to check if there is a third level trigger.

Detector triggers

- **The third level trigger (T3)**

  Only tanks with a second level trigger (T2) are used to check if the T3 conditions are fulfilled. This trigger is a requirement on the time a geometrical pattern of the T2 triggered stations. The requirement is made up of conditions labeled *nCm*. The nomenclature for theses conditions is based on the number of stations triggered within the first hexagons (up to four) around a given tank called *"central station"*. The expression *nCm* means that *n* tanks within the first *m* hexagons around the central station have a second level trigger. Similar requirements for tanks with ToT local triggers only are labeled with the postfix *ToT* (*nCmTOT*).

  All the T2 triggers sent to the CDAS within a time window of $50\ \mu s$ are temporarily ordered. For each T2 triggered tank, the number of second level triggers in each hexagon is counted. A third level trigger is fired when at least one of two conditions (*2C1TOT & 3C2*) or (*2C1 & 3C2 & 4C4*) is found. Once a central trigger is found, all tanks up to the sixth hexagon around every T2 that had been sent to the CDAS to search for the T3 pattern, are asked to send their data in a time window of $(6 + 5n)\mu s$ around the central trigger time where n is the hexagon number around the central station [51]. This procedure is however inefficient as there are indications that not all T1 tanks are kept.

Besides this pattern search, an external third level trigger condition has been set up to use the hybrid performance of the Auger observatory as described in the FD detector section. Whenever a T3 is detected by the fluorescence detector, all the stations are requested by the CDAS to send their data within a time window of $120\ \mu s$ of the event time. This event time has to be corrected by the time it takes to the light to travel from the impact point to the detection eye. This time has been fixed to the time it takes the light to travel from the center of the array (Celeste tank) to the corresponding eye. The SD event is flagged as an FD T3 trigger.

- **Physical trigger (T4)**

  This trigger is intended to select the events produced by extensive air showers from the bulk of detected showers than could have been produced by chance coincidences of local triggers. This trigger has a different implementation for vertical and for inclined showers.

  The physical trigger for vertical showers uses two main characteristics of vertical air showers. The first one is a certain compactness of triggered tanks, the second one is the fact that most of the detected signals are spread enough in time to fulfill the ToT trigger condition. The requirement of a compact 3 ToT (3 neighbor tanks in a triangular configuration) ensures that 99% of the selected showers are physical events [52].

  The requirements of the vertical T4 is too restrictive for inclined events because of their elongated profiles and the fact that ToT triggers are typically due to the electromagnetic component of the shower which is practically absent in inclined showers. A new T4 is demanded to select inclined events out of the T3 data. The fourth level trigger is proposed in [53] as it was defined in [54]. It is based on the search of a plane shower front compatible in time with the maximum number of triggered stations.

  Three criteria are used to accept a configuration. A physical incoming direction has to be found, the residuals of the fit have to be below a certain level and the stations are asked to lie within a cylinder around the shower axis taking into account that the number of stations is rather proportional to the area of the ground footprint

of the shower. Values of the residual tolerance and of the cylinder radius can be tuned to improve the selection criteria.

- **Quality trigger (T5)**

  This last trigger level tries to ensure a good reconstruction of the parameters of the detected air showers as its incoming direction and its energy. This trigger excludes events that hit the ground too close to a hole or the edge of the array. Besides ensuring a high quality of the reconstruction parameters, the fifth level trigger constrains the exposed area because it is very hard to compute the acceptance of the array if we take into account events that hit the ground at an impact point outside the array [55].

  This trigger level ensures that a portion of the array at the area where the air shower hits the ground is properly working at the time it arrives. For vertical showers it is enough that the first hexagon around the tank with the highest signal is active. For inclined showers, and due to their elongated footprints, the highest signal tank is not so representative of the impact point so the station closest to the reconstructed core is asked to be surrounded by a hexagon of active tanks.

2.4 Recent results of the Pierre Auger Observatory

During the five years that the south site of the Pierre Auger Observatory has been taking data, several results have been published. In this section a brief comment about five of them concerning the cosmic ray flux, the study of their arrival directions and some hints about composition is given.

2.4.1 Energy spectrum

The measurement of the energy spectrum of cosmic rays above $2.5 \cdot 10^{18}\ eV$, derived from 20,000 events recorded at the Pierre Auger Observatory was published in [56] and it is shown in fig. 2.14. The spectral index γ of the flux $J\ E^{-\gamma}$, at energies between $4 \cdot 10^{18}\ eV$ and $4 \cdot 10^{19}\ eV$ was quoted to be $2.69 \pm 0.02(stat) \pm 0.06(syst)$, steepening to $4.2 \pm 0.4(stat) \pm 0.06(syst)$ at higher energies.

This measurement is consistent with the prediction by Greisen and by Zatsepin and Kuzmin [17]. With an exposure twice that of HiRes [57] and 4 times that of AGASA [58], our evidence supports the recent report of the former.

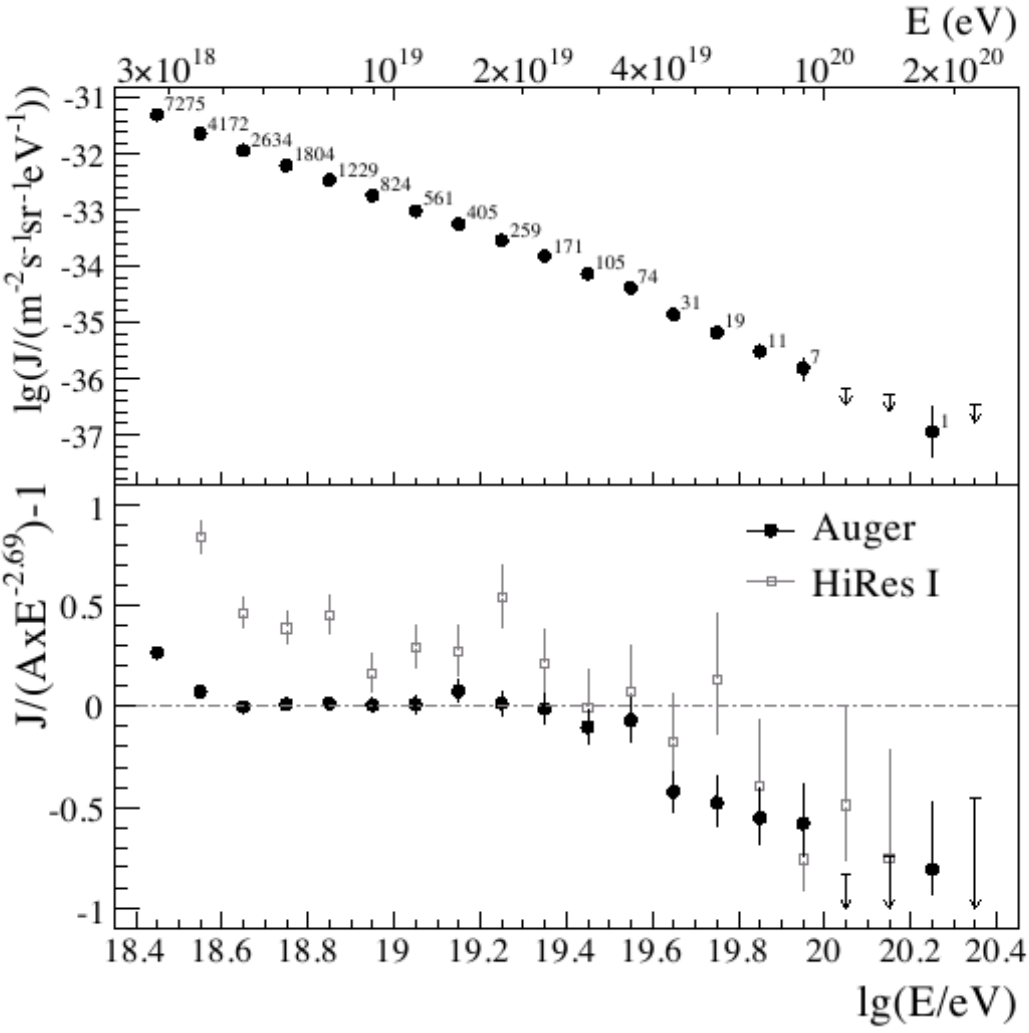

Figure 2.14: Upper panel: The differential flux J as a function of energy. Lower Panel: The fractional differences between Auger (black dots) and HiRes I (grey squares) data compared with predictions of a spectrum with an index of $\gamma = -2.69$. In both panels vertical lines are only statistical uncertainty.

2.4.2 Arrival directions

A great challenge for astroparticle physics today is the identification of the sources of UHECR. If these cosmic rays are nuclei, only sources within $\approx 200\ Mpc$ from the Earth can contribute to the cosmic ray flux. The flux from more distant sources is attenuated mainly due to interactions with the microwave background photons for protons [17] or to photo-desintegration processes for nuclei [59] as has been commented for the suppression of the cosmic ray flux. As nearby sources are not uniformly distributed and given the small magnetic deflections of the trajectories of such high energetic cosmic rays, their arrival directions should be anisotropic pointing back to their origin.

A recent result of the Pierre Auger Observatory shows a correlation of the arrival direction of very high energy cosmic rays with energies above $57\ EeV$ with $3.2°$ windows at the directions of nearby ($z < 0.018$) active galactic nuclei [60]. Active Galatic Nuclei (AGN) which are very active galaxies with supermassive black holes located in their centers have been postulated as sites for cosmic ray acceleration [61]. Fig. 2.15 shows the published arrival direction distribution together with the AGN locations from the Veron-Veron Cetty catalog with $z < 0.018$ [62].

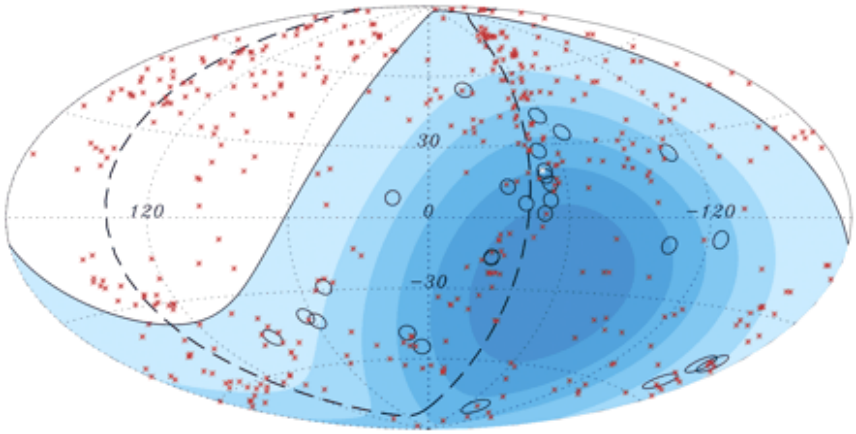

Figure 2.15: Celestial sphere in galactic coordinates with the supergalactic plane indicated by the dashed line. Circles are $3.2°$ radius centered in the arrival direction of the highest energy cosmic rays detected by the observatory. Red stars indicate the position of 472 AGNs with redshift below 0.018 from the 12th catalog of quasar and active nuclei [62].

This result is an evidence of the anisotropy of UHECR which has been tested against a given catalog. Further tests are also in progress.

2.4.3 Mass composition

The cosmic ray composition has been studied by the Auger observatory using the longitudinal profiles of the showers [63]. The depth of the shower maximum X_{max} is directly measured by the fluorescence detector of the observatory. The average X_{max} has been compared with predictions from shower simulations with different hadronic models. The average of X_{max} at a certain energy is related to the mean logarithmic mass as:

$$< X_{max} >= D_p[ln(E/E_0) - < lnA >] + c_p \tag{2.10}$$

where D_p is the elongation rate of a proton and c_p is the average depth of proton with energy E_0. Different models give slightly different values for D_p and c_p.

With more than 4300 events after all the selection cuts, the resulting mean X_{max} as a function of energy is shown in fig. 2.16. A simple linear fit to all the data gives an elongation rate of $54 \pm 2\ g\ cm^{-2}/decade$ but the fit is not very good. Allowing a break in the elongation rate, the fits shown in grey are much better giving elongation rates of $71 \pm 5\ g\ cm^{-2}/decade$ below $10^{18.35}\ eV$ and $40 \pm 4\ g\ cm^{-2}/decade$ above that energy cut.

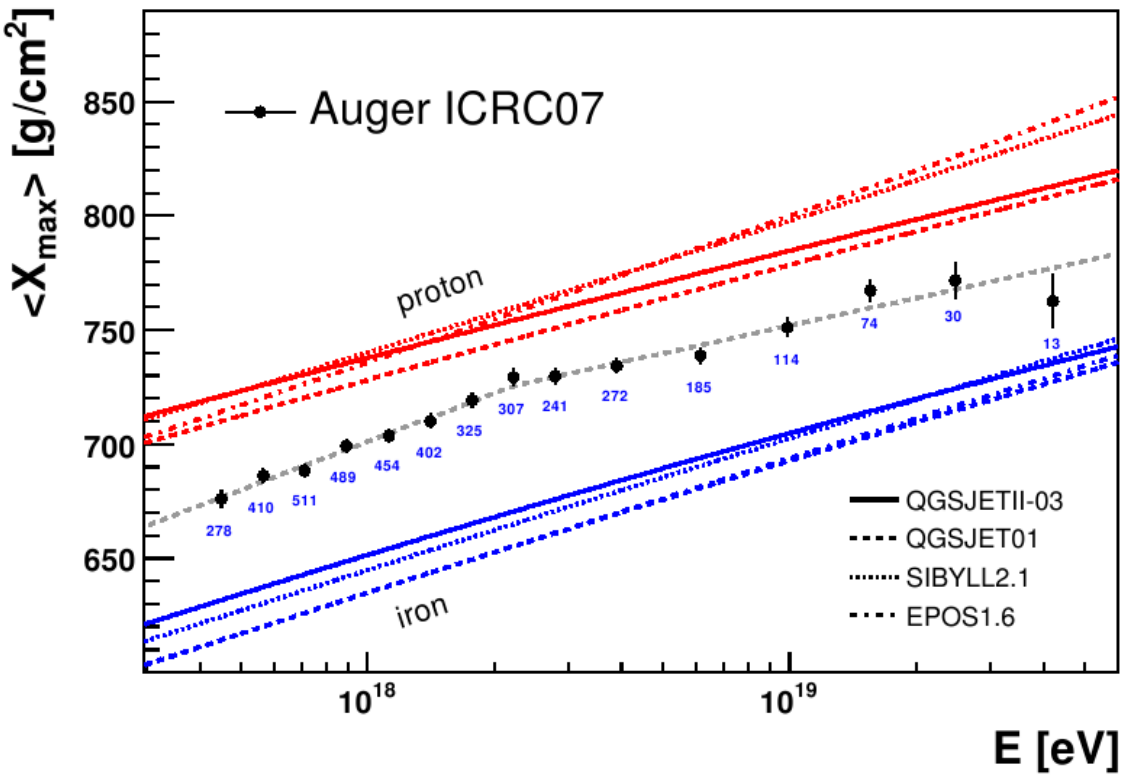

Figure 2.16: Average shower maximum as a function of energy. The change in the elongation rate at $10^{18.35}\ eV$ may be due to a change in the composition of the cosmic rays. Numbers are the available events to find the average elongation rate at that energy bin.

Other parameters such as the fluctuations of X_{max} or the time structure of shower particles can be also used to infer mass composition [64].

2.4.4 Photon limit

Extensive air showers originated by photons have a different development in the atmosphere than those originated by hadrons. They develop over a larger atmospheric depth and the position of their shower maximum X_{max} is deeper. As X_{max} can be directly measured by the fluorescence detector or extracted from measurements of the surface detector, limits to the photon fraction can be set by the Auger observatory as shown

in fig. 2.17. Some models of UHECR production have been discarded with these limits due to the high photon fraction they predicted [65, 66].

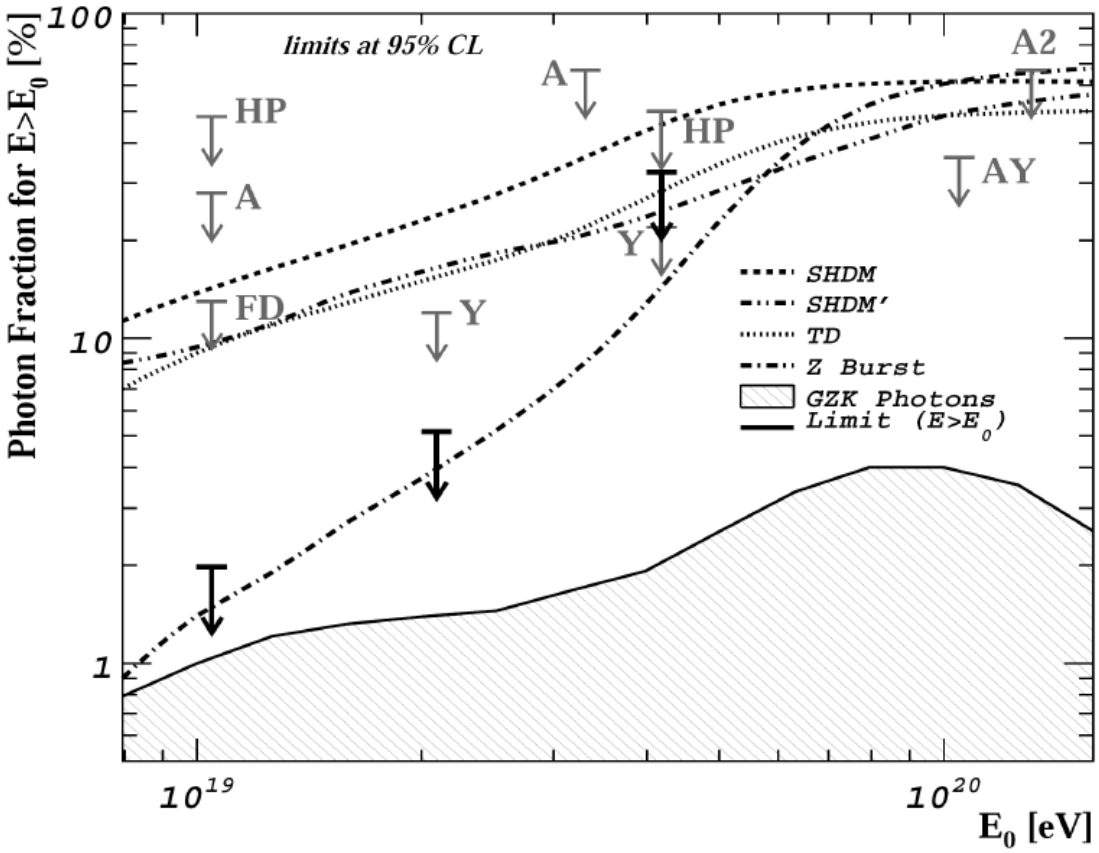

Figure 2.17: Photon limit measured by the Auger observatory. Black arrows are limits placed using measurements of the surface detector [65] while arrows tagged as *FD* are using measurements of the fluorescence detector [66]. Other results from experiments as Haverah Park (HP), AGASA (A), Yakustk (Y) and AGASA-Yakustk (AY) are also shown as well as the photon flux predictions from several top-down models.

2.4.5 Neutrino limit

A limit to the neutrino flux has been set by the Pierre Auger Observatory [67] studying upcoming showers from ν_τ interaction with the Earth's crust. As ν_τ may interact in the Earth's crust under the surface detector of the observatory, the resulting τ lepton can

enter the atmosphere above the array and its decay may be observed. The resulting shower will travel almost horizontally and with differential features from usual hadronic showers. No ν_τ candidates have been observed yet and an upper limit to the neutrino flux has been set as shown in fig. 2.18.

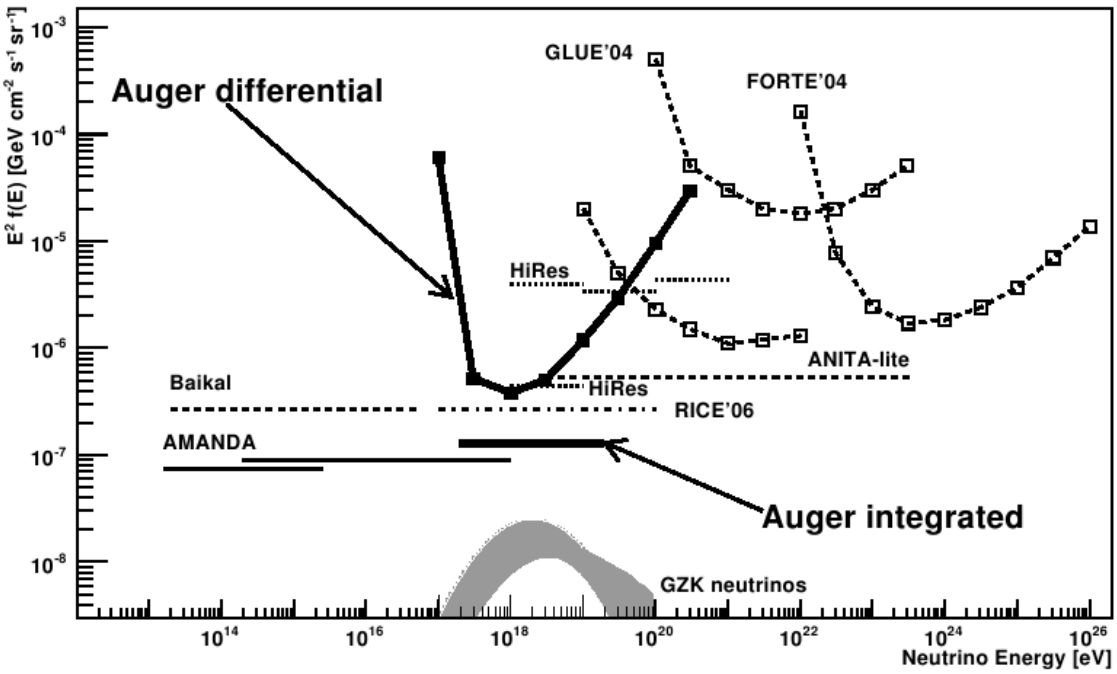

Figure 2.18: Neutrino limit at the 90% of the confidence level measured by the Auger observatory. Other results are also shown as well as the neutrino flux from GZK interactions.

Also several studies are being carried to set a limit to the neutrino flux searching for deep horizontal showers induced by neutrinos in the atmosphere at large zenith angles [68].

Bibliography

[1] V. F. Hess, Phys. Z. **13** (1912) 1804.

[2] R. Ulrich PhD. Thesis, "Measurement of the proton-air cross section using hybrid data of the Pierre Auger observatory", Pierre Auger Collaboration Internal Document, GAP Note 2008-004.

[3] G. A. Medina-Tanco, astroph/0607543.

V. Berezinsky, astroph/07102750

[4] N. L. Grigorov *et al.*, Yad. Fiz. **11** (1970) 1058.

T. Abu-Zayyad *et al.*, Astropart. Phys. **23** (2005) 157.

V. A. Derbina *et al.*, Astrophys. J. **628** (2005) 41.

T. Antoni *et al.*, Astropart. Phys. **24** (2005) 1.

D. J. Bird *et al.*, Astrophys. J. 424 **424** (1994) 491.

T. T. Yamamoto, Proc. 30th International Cosmic Ray Conference, Mérida-México, **4** (2007) 335.

[5] D. J. Bird *et al.*, Astrophys. J. **424** (1994) 491.

[6] S. C. Corbato *et al.*, Nucl. Phys. Proc. Suppl. **28B** (1992) 36.

[7] J. Linsley, Phys. Rev. Lett. **97** (1955) 1292.

[8] M.A. Lawrence *et al.*, J. Phys. G **17** (1991) 733.

[9] M.M. Winn *et al.*, J. Phys. G **12** (1986) 653.

[10] N.N. Efimov *et al.*, "Astrophysical Aspects of the Most Energetic Cosmic Rays", World Scientific, Singapore (1991) 20.

[11] M. Nagano *et al.*, J. Phys. G **10** (1984) 1295.

M. Nagano *et al.*, J. Phys. G **18** (1992) 423.

S. Yoshida *et al.*, Astropart. Phys. **3** (1995) 105.

Takeda *et al.*, Phys. Rev. Lett. **81** (1998) 1163.

[12] R. Abbasi *et al.*, Phys. Rev. Lett. **100** (2008) 101101.

P. Sokolsky, Nucl. Phys. Proc. Suppl. **175-176** (2008) 207.

B. Zhang & Z. Cao, Nucl. Phys. Proc. Suppl. **175-176** (2008) 241.

[13] The Pierre Auger Observatory Design Report, March 1997.

[14] E. Fermi, Phys. Rev. **75** (1949) 1169.

[15] A. M. Hillas, Ann. Rev. Astron. Astrophys. **22** (1984) 425.

[16] A. A. Penzias & R. W. Wilson, Astrophys. J. **142** (1965) 419.

[17] K. Greisen, Phys. Rev. Lett. **16** (1966) 748.

G. T. Zatsepin & V. A. Kuz'min, JETP Lett. **4** (1966) 78.

[18] F. A. Aharonian & J. W. Cronin, Phys. Rev. D **50** (1994) 1892.

[19] J. W. Cronin, Nucl. Phys. Proc. Suppl. **138** (2005) 465.

[20] F. W. Stecker & M. H. Salamon, Astrophys. J. **512** (1999) 521.

[21] B. Rossi, "Cosmic rays", McGrawn Hill (1964).

[22] P. Auger, Rev. Mod. Phys. **11** (1939) 288.

[23] W. Heitler, "Quatum theory of radiation", Oxford University Press (1944).

[24] B. Rossi & K. Greisen, Rev. Mod. Phys. **13** (1941) 240.

[25] K. Greisen, Progr. Cosmic Ray Physics **3** (1956) 1.

[26] K. Kamata & J. Nishimura, Prog. Theor. Phys. Suppl. **6** (1956) 93.

[27] T. K. Gaiser & A. M. Hillas, Proc. 15th International Cosmic Ray Conference, Plovdiv-Bulgary, **8** (1977) 353.

[28] K. Greisen, Ann. Rev. Nucl. Sci. **10** (1960) 63.

[29] M. Ave *et al.*, Astropart. Phys **19** (2003) 47.

[30] K. Greisen, Ann. Revs. Nuclear Science **10** (1960) 63.

[31] Auger Collaboration, "Survey of the Pierre Auger observatory", Proc. 27th International Cosmic Ray Conference, Hamburg-Germany (2001).

[32] A. Cordero *et al.*, "Proposal for the optical system of the fluorescence detector of the Auger project", Pierre Auger Collaboration Internal Document, GAP Note 1996-039.

[33] C. Escobar & R. Sato, "Performance of the fluorescence detectors of the Pierre Auger Observatory", Proc. 29th International Cosmic Ray Conference, Pune-India, **7** (2005) 13.

[34] C. Escobar & R. Sato, "The performance of the corector lenses for the Auger fluorescence detector", Proc. 29th International Cosmic Ray Conference, Pune-India, **8** (2005) 13.

[35] M. Ambrosio *et al.*, Nucl. Instrum. Meth. A **478** (2002) 125.

[36] R. Winston & W. T. Welford, "High collection nominaging optics", Academic Press, New York, 1989.

[37] P. Facal San Luis & P. Privitera, "Measurement of the FD camera light collection efficiency and uniformity", Pierre Auger Collaboration Internal Document, GAP Note 2000-010.

[38] H. Gemmeke *et al.*, IEEE Trans. Nucl. Sci. **47** (2000) 371.

[39] A. Schmidt *et al.*, "New third level trigger for the fluorescence telescopes", Pierre Auger Collaboration Internal Document, GAP Note 2007-118.

[40] P. Bauleo *et al.*, "Absolute calibration of the Auger fluorescence detector", Proc. 29th International Cosmic Ray Conference, Pune-India, **8** (2005) 5.

[41] C. Aramo *et al.*, "Optical relative calibration and stability monitoring for the Auger fluorescence detector", Proc. 29th International Cosmic Ray Conference, Pune-India, **8** (2005) 101.

[42] B. Fick *et al.*, "The first central laser facility", Pierre Auger Collaboration Internal Document, GAP Note 2004-003.

F. Arqueros *et al.*, "The central laser facility at the Pierre Auger observatory", Proc. 29th International Cosmic Ray Conference, Pune-India, **8** (2005) 335.

[43] M. Monasor PhD. Thesis, "Energy calibration of the Pierre Auger observatory. Measurement of the spectrum of ultra high energy cosmic rays", Pierre Auger Collaboration Internal Document, GAP Note 2008-167.

[44] J. Abraham *et al.*, Nucl. Instrum. Meth. A **523** (2004) 50.

[45] C. L. Pryke & J. Lloyd-Evans, Nucl. Instrum. Meth. A **354** (1995) 560.

[46] C. L. Pryke, Nucl. Instrum. Meth. A **394** (1997) 420.

[47] P.D.J. Clarck, D. Nitz *et al.*, "Communications in the Auger Observatory", Proc. 27th International Cosmic Ray Conference, Hamburg-Germany, (2001).

[48] X. Bertou *et al.*, Nucl. Instrum. Meth. A **568** (206) 839.

[49] M. Aglietta *et al.*, "Response of the Pierre Auger Observatory water Cherenkov detectors to muons", Proc. 29th International Cosmic Ray Conference, Pune-India, **7** (2005) 83.

[50] D. Allard *et al.*, "The trigger system of the Pierre Auger surface detector: operation, efficiency and stability", Proc. 29th International Cosmic Ray Conference, Pune-India, **7** (2005) 287.

[51] Pierre Auger Observatory Data Operations E-Log Wed 3 Jan 2007 – 15:33:29.

[52] P. Ghia, "The compact 3ToT as SD physics trigger for vertical ($\theta < 60°$) showers", Pierre Auger Collaboration Internal Document, GAP Note 2004-018.

[53] O. Blanch & J. González, "Aiming for an official T4 above 60 degrees", Pierre Auger Collaboration Internal Document, GAP Note 2007-028.

[54] P. Billoir, "Top-down selection of events and stations in surface detector triggers", Pierre Auger Collaboration Internal Document, GAP Note 2006-072.

[55] E. Parizot, I. Lhenry, D. Allard, P. Ghia, & G. Navarra, "First steps towards the definition of a "quality trigger" (T5) for the SD acceptance calculations", Pierre Auger Collaboration Internal Document, GAP Note 2004-023.

[56] J. Abraham *et al.*, Phys. Rev. Lett. **101** (2008) 061101.

[57] R. U. Abbasi *et al.*, Phys. Rev. Lett. **100** (2008) 101101.

[58] M. Takeda *et al.*, Astropart. Phys. **19** (2003) 447.

[59] J. L. Puget, F. W. Stecker & J. J. Bredekamp, Astrophys. J. **205** (1976) 638.

L. N. Epele & E. Roulet, Phys. Rev. Lett. **81** (1999) 3295.

[60] J. Abraham *et al.*, Science **318** (2007) 939.

[61]

[62] M. P. Véron-Cetty & P. Véron, Astron. Astrophys. **455** (2006) 773.

[63] M. Unger *et al.*, "Study of the cosmic ray composition above 0.2 EeV using the longitudinal profiles of showers observed at the Pierre Auger Observatory", Proc. 30th International Cosmic Ray Conference, Mérida-México, **4** (2007) 373.

[64] B. Smith PhD. Thesis, "The Mass Composition of Cosmic Rays Above 1 EeV Inferred Using the Spread in Arrival Times of Air Shower Particles", Pierre Auger Collaboration Internal Document, GAP Note 2008-161.

[65] J. Abraham *et al.*, Astropart. Phys. **29** (2008) 243.

[66] J. Abraham *et al.*, Astropart. Phys. **27** (2007) 155.

[67] J. Abraham *et al.*, Phys. Rev. Lett. **100** (2008) 211101.

[68] I. Valiño PhD. Thesis, "Detection of Horizontal Air Showers and Neutrino induced Showers with the Pierre Auger Observatory", Pierre Auger Collaboration Internal Document, GAP Note 2008-024.

J. Álvarez-Muñiz *et al.*, "The sensitivity of the surface detector of the Pierre Auger Observatory to UHE Earth-skimming and down-going neutrinos", Proc. 30th International Cosmic Ray Conference, Mérida-México, **4** (2007) 389.

Chapter 3

Reconstruction of the arrival direction of inclined showers.

3.1 General Procedure

A precise reconstruction of the arrival direction of the air showers detected at the Auger Observatory is desirable for several reasons. Good knowledge of the incoming direction is fundamental for the complete reconstruction of the extensive air shower and hence for the determination of the impact point of the shower core and of its energy. This is particularly important for inclined showers because there is a known correlation between reconstructed energy and zenith angle induced by the attenuation of the muonic component [1]. In addition, an accurate reconstruction of the arrival direction is of utmost importance for the search for anisotropies of the ultra high energy cosmic rays what is certainly one of the most important goals of the experiment.

Particles in the extensive air shower propagate through the atmosphere with a complex distribution. The particles spread away from the shower axis approximately keeping cylindrical symmetry. In reality, particles accumulate delays with respect to the *shower plane* defined as that traveling at speed of light perpendicular to the shower axis and in time with the initial cosmic ray. These delays due to the scatter of particle and their deviation from shower axis and the shower makes the front acquire curvature. The distributions of these time delays have been carefully studied for muons in inclined showers in [2]. As the distance to the shower axis rises, both the average and the width of this distribution increase.

At the beginning of the fifties, it was shown that the arrival direction of the cosmic rays can be estimated from the measurements of the arrival time of the signals at different points of an extensive air shower sampled by an array of detectors at ground level [3]. Since then, many other similar ground array experiments have been built, and all of them have used the arrival times of the shower front for the determination of the extensive air shower incoming direction.

The incoming shower direction is obtained by fitting a time associated to the arrival of the shower front at each triggered tank (t^{meas}) to that predicted according to a given model (t^{exp}) that depends on the incoming direction of the shower. Usually this fitting is done by a minimum χ^2 method:

$$\chi^2 = \sum_{i=0}^{i=N} \frac{(\Delta t_i)^2}{\sigma_i^2} = \sum_{i=0}^{i=N} \frac{(t_i^{meas} - t_i^{exp})^2}{\sigma_i^2} \tag{3.1}$$

where i runs through all the array detectors with a detected signal and σ_i corresponds to the uncertainty in the times. Within the Collaboration of the Pierre Auger Observatory, some works have been published with several reconstruction methods of the arrival direction [4–8]. They differ on the choices of the expected arrival time, t_i^{exp}, and of the uncertainty on the arrival time, σ_i. In the analysis of inclined events presented in the following chapters, a different choice than the one made for vertical events will be used. This one is based on the model proposed in [2] and described in section 3.5 that predicts both the curvature of the shower front, t_i^{exp}, and the time variance, σ_i.

The three magnitudes involved in the χ^2 minimization in the different approaches are addressed in the next sections. Section 3.2 deals with the start time and its measurement. Different procedures to estimate the expected time are explained in section 3.3. Section 3.4 is devoted to the variance on the start time. In order to justify the use of the time model described in 3.5, its prediction for the variance will be compared with to that used in vertical events in section 3.6 and the angular resolution obtained with our approach will be validated using hybrid events in section 3.7.

3.2 Start time

Shower particles follow different distributions of arrival time at ground depending on the zenith angle of the shower and on the distance to the shower axis, so several choices can

be made to assign a measured time to the shower front at any distance from the shower axis. At a first glance the mean of the distribution of arrival times could be thought as the natural choice, however this is not favored because the actual time distributions are not known. The onset of the time distribution is thought to be a better choice because an estimator of this time can be extracted directly from the data: the start time of the signal. However, it is a biased estimator due to the stochastic nature of the arrival of shower particles. Particles of the shower front will always arrive at the detector later than expected from the onset of the time distributions which ultimately must be related to causality. The measured start time of the signal is the arrival time of the first particle which will become a better estimator of the onset of the time distribution as the number of detected particle increases. This is often referred as the *"sampling effect"* and it is potentially important for inclined showers because a single muon can produce a second level trigger.

3.2.1 Expectations

The shower front is behind the shower plane and practically tangent to it at the shower axis so the direction normal to this plane can be determined from timing data at relatively small distances from the shower core. In general, it is convenient to measure the arrival time of the shower front at a given point with respect to the arrival time of this plane, t^{plane}.

Due to causality, shower particles can not reach the ground before the shower plane. The more the particles travel in straight lines at speed of light and near the shower axis, the closer they are to this imaginary front. Far from the shower axis, they accumulate more delay due to the angular deflections in their interactions with the medium and to their subluminal velocities.

The arrival time of the first particle can be writen as:

$$T^1 = t^{plane} + T^0 + t^s \tag{3.2}$$

where t^{plane} is the arrival time of the shower plane, T^0 is the delay of the shower front with respect to this plane and t^s is the delay of the first particle within the shower front.

The delay of the shower front with respect to the shower plane, T^0, is related to the curvature of the shower front, whereas the delay of the first particle with respect

to the shower front, t^s can be related to the variance of the start time. This work will follow this distinction between curvature and variance, so the expected arrival time of the shower front at a given point will be $t^{exp} = t^{plane} + T^0$ with a variance $V[t] = V[t^s]$.

3.2.2 Start time measurement

The detection time used in eq. 3.1, t^{meas}, is determined from the *trigger time* of each tank. Detected events are built on a basis of local triggers as it has been described in the chapter devoted to the Auger observatory. For each tank that passes a $T1$ trigger, a trigger time is recorded from the time provided by the GPS receiver which is part of each station of the surface detector. This trigger time is related to the instant when the signal fulfills one of the $T1$ trigger conditions.

An algorithm that runs through the recorded signal traces searches the *Start Bin* associated to the onset of the signal. For each of the three PMTs, sections of the ADC trace with at least two consecutive bins with 3 counts over the baseline ($\approx 0.06\ VEM_{peak}$) are searched. Two sections are merged if they are closer than $20\ bins$ and the ratio of their charges is greater than 30%, if not they are considered as different signals. Once the sections with signal have been found for each PMT, an inclusive merge of them is made between active PMTs: sections with bins in common are taken as parts of a single signal and the earliest (latest) of the bins is assumed to be the start (end) bin of the merged signal. The section with the greatest $area * \frac{area}{peak}$ is selected as the tank signal and its start and end bins are considered as those of the signal. This algorithm improves the start time determination for traces having signals previous to the trigger time and smaller than the trigger threshold and reduces fluctuations on the start time associated with direct light.

In addition to these small signals before the trigger time, it is possible that an isolated atmospheric muon crosses the tank just before the shower front. The start time of the signal will be misrecorded being assigned to the arrival of the isolated muon and not to the arrival of the shower particles. A trace cleaning algorithm has been developed in an attempt to keep the part of the trace that belongs to the detected shower and to remove the signal due to these isolated muons (See fig. 3.1). The trace cleaning procedure described in detail in [9] is already implemented in the data acquisition software used for the work presented in this thesis [10]. The signal trace is searched for different

segments separated by gaps without signal. Segments of consecutive bins are classified as acceptable if their number of bins above a tuning threshold (N_{above}) is greater than a minimum number (N_{min}), or if the sum of the bin signals (S) is greater than a minimum signal (S_{min}). Both minima, N_{min} and S_{min}, as well as the threshold level, can be tuned depending on the aim of the study: evaluation of the start time, rejection of exotics background, etc. The main segment which will define the start bin is the one with the highest product of the number of bins above the threshold times their total signal. After this treatment of the recorded signal, a good fraction of the random muons is eliminated and the start time of the signal is a better estimator of the arrival time of the shower front.

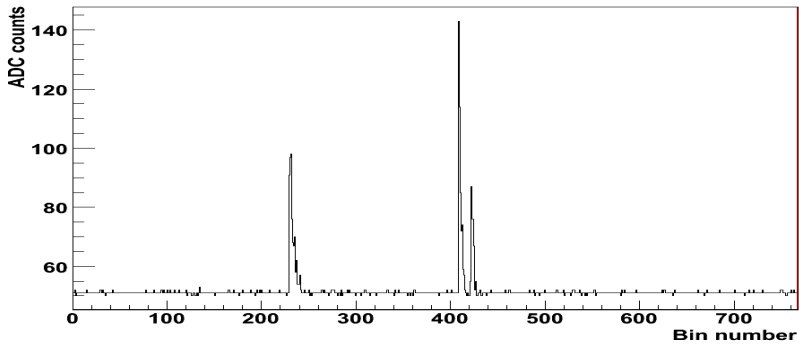

Figure 3.1: FADC trace showing an isolated muon prior to the main signal which distorts the signal start time measurement.

3.3 Fitting the start time

The expected arrival times of the cascade at the locations of the stations are given by an assumption about the behavior of the shower front. The front of the cascade consists of the particles that first pass through a given point which generate start time of the signal. Several hypotheses can be made to estimate the expected arrival time of the first particles that reach each detector of the surface array being the simplest one a plane front ($T^0 = 0$ in eq. 3.2). Other possibilities include spherical fronts, expanding spherical fronts, parabolic fronts, etc. Fig. 3.2 shows the propagation of the actual shower front and two approximations to its real behavior, the plane front and the spherical front. In

the work presented in this thesis we will use a model that predicts the mean delay of muons that reach ground level from [2].

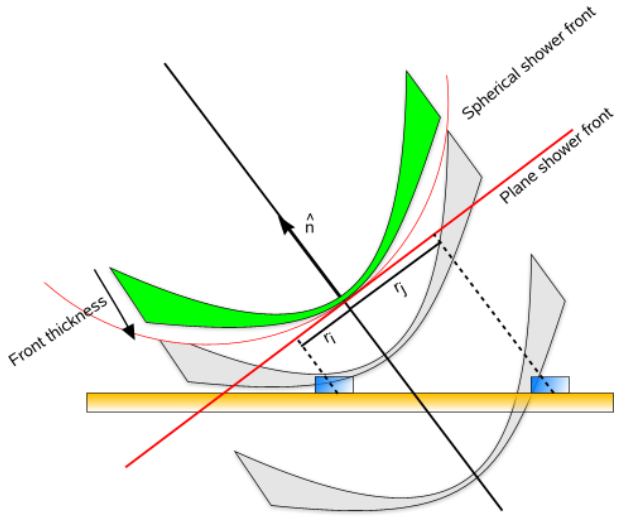

Figure 3.2: The particle swarm of the cascade is shown in green with the shower axis in black. Plane and spherical approximations are shown in red. Two detectors of the array are shown in blue: the former triggered by the early part of the shower and the latter by the late part. Their distances to the shower core measured on the shower plane are also shown.

3.3.1 Shower plane front

In the reconstruction of inclined showers performed in this work, the first determination of the arrival direction is performed assuming that the shower front is a plane moving at the speed of light. It has been shown that for a given distance to the core, the delay of the particles with respect to this shower plane decreases with increasing zenith angle [11], so the assumption of a plane shower front is a better approximation for inclined showers than for vertical showers. The expected time can be written for each station i in terms of its position, $\vec{r}_i$ as:

$$t_i^{exp} = t_0 - \frac{\hat{n} \cdot (\vec{r}_i - \vec{r}_0)}{c} \tag{3.3}$$

where t_0 is the arrival time of the shower at ground and $\vec{r}_0$ its impact point, $\hat{n}$ is an unitary vector pointing towards the incoming direction of the shower and c is the speed of light. The impact point of the shower must be obtained in a more accurate way by other means. At the beginning of the reconstruction procedure, $\vec{r}_0$, is approximated using the barycentre of the tank positions weighted by the square root of the integrated signals.

The time difference between predicted and measured times, for a plane front assumption can be expressed as:

$$\Delta t_i(t_0, \hat{n}) = t_i^{meas} - t_i^{exp} = t_i - [t_0 - \frac{\hat{n} \cdot (\vec{r}_i - \vec{r}_0)}{c}] \tag{3.4}$$

This difference between measured and predicted times is minimized with respect to t_0 and $\hat{n}$, using a minimum χ^2 procedure. For this minimization procedure the additional constraint that $\sum_{i=1}^{i=3} n_i^2 = 1$ will be used. This constraint allows us to perform a three parameter fit. Using this constraint, the expected time can be written for each station as:

$$\begin{aligned} t_i^{exp} &= t_0 - \frac{\hat{n} \cdot (\vec{r}_i - \vec{r}_0)}{c} \\ &= t_0 - \frac{n_x\ (x_i - x_0) + n_y\ (y_i - y_0) + \sqrt{1 - n_x^2 - n_y^2}\ (z_i - z_0)}{c} \end{aligned} \tag{3.5}$$

3.3.2 Front curvature

Different studies of the time structure of extensive air showers [11–14] have shown that arrival time at ground of the shower front cannot be modeled by a plane ($T^0 \neq 0$ in eq. 3.2).

A simple time delay using a spherical shower front with constant curvature can be implemented as $T_i^0 = \frac{d_i^2}{2Rc}$, where d_i is the distance of the station i to the shower axis on the shower plane, R is the radius of curvature of the shower front and c is the speed of light. The radius of curvature, R, can be either fitted through the minimum χ^2 procedure or may be given in advance if the number of stations available is not high enough to allow a four parameters fit. The produced delay with respect to the shower plane is symmetric around the shower axis. For this shower front model, the core position

is essential because the axis is set-up in the core position and adjusted in direction to fit the station times. The time fit and LDF fit are entangled, since change in the core position requires an axis readjustment. This fact leads to a combined "global" fit.

However, we know that the shower front is not spherical and has not a constant curvature. On the contrary, the delay T^0 in eq. 3.2 depends not only on the zenith angle of the shower and on the distance to the shower core but also on the azimuth of the observation point.

In the analysis of vertical events, a spherical shower front model describing a difference in early and late parts of the shower is used. This model incorporates the asymmetric radius of curvature by construction, since the front is not modeled as fixed-radius sphere moving along the axis but it is described as concentrically growing spheres, i.e. like in an explosion. The radius of curvature of the shower front depends on time, and hence on the position at ground, as shown in fig. 3.3.

For this "concentric" shower front, no notion of the shower core is needed. The result of the fit of the station timings is the shower "center". The shower axis, that it is not fitted, is obtained as a normalized vector between the shower "center" and the core position after the core reconstruction. With this model, the LDF part and timing part are fitted separately. Both fits are only entangled by the time variance model that contains a dependence on the zenith angle that couples the two parts of the reconstruction. The radius of curvature when the shower-front goes through the core position corresponds to the one obtained from the constant curvature fit.

The model employed in this thesis work allows us to calculate the mean delay of the muons with respect to the shower plane, which relates to the curvature of the front being the early-late asymmetry of the curvature taken into account. This delay does not arises from any assumption about the shower front structure (plane, spherical, parabolic,...) but from physical arguments about the propagation of the muonic component of the shower in the atmosphere.

Measured times are then corrected for the mean delay T^0 as predicted by the model and shown in fig. 3.5 for certain measurement conditions. These corrected times are fitted to a plane front to obtain the incoming direction of the shower. This time model needs the core position to calculate the delays but, besides being these delays based on physical assumptions about the passage of muons through the atmosphere, the model also provides the start time variance to be used in the fit.

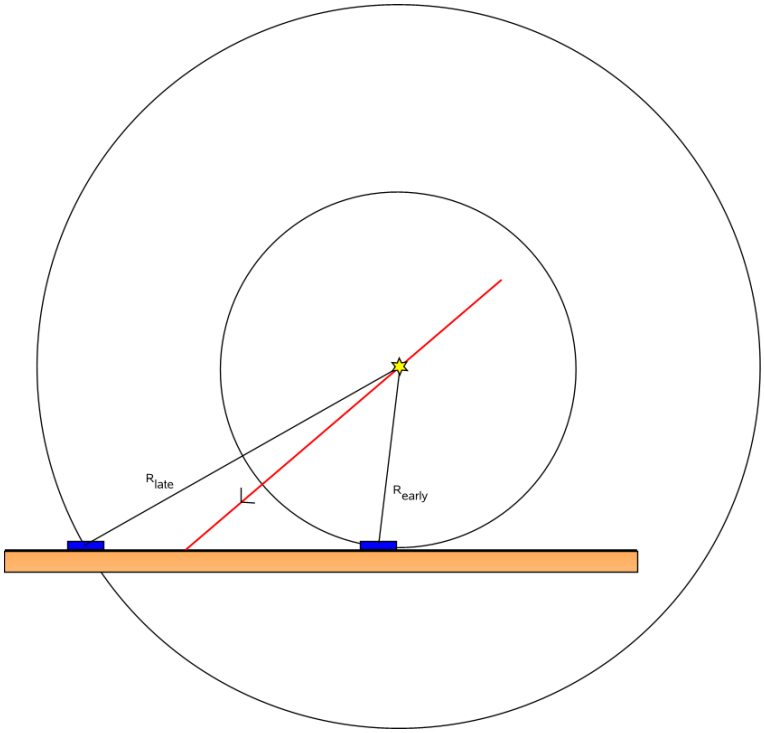

Figure 3.3: Concentric shower front arriving at two tanks (blue squares) of the surface array. The red line is the shower axis and the yellow star tags the "shower center". Different radii of curvature of the shower front will be seen from the early or the late part of the shower.

3.4 Start time variance

Drawing meaningful physical results from the χ^2 fitting procedure requires a proper evaluation of the uncertainty of the incoming direction of the detected air shower. The precision of the arrival direction reconstruction, depends not only on the precision of the clock which measures the arrival times, but also on the fluctuations in the arrival time at ground of the particles which are part of the shower front.

The procedure to obtain the arrival direction from the surface detector data, based on the fitting of the start times of the signals in the tanks to the predicted times from a propagation model of the shower front, has to properly take into account the uncertainties in the start time measurement. The uncertainty in the reconstructed direction, extracted from the fitting procedure, is directly related to these uncertainties so to have

an adequate estimate of that uncertainty, fluctuations in the arrival time have to be properly modeled or parameterized. The start time variance for each signal that enters eq. 3.1, σ_i, takes into account these fluctuations and should give a proper weight to each station in the reconstruction procedure.

The uncertainty in the star time can be considered as a delay in the arrival time of the first particle with respect to a theoretical shower front (t_s in eq. 3.2) and it is related to the arrival time distribution of the particles at ground.

The variance of the start time has a contribution due to the precision of the time measurement device. This contribution is related to the GPS resolution ($10\ ns$) [15] and to the FADC sampling ($25\ ns$) has been estimated in [16] as:

$$V[t^s]_{timing} = 10^2 + \left(\frac{25}{\sqrt{12}}\right)^2 \approx 150\ ns^2$$

In addition to this estimate there are uncertainties associated to the position of the impact point of the particle in the tank which are not accounted for. Besides, there are fluctuations associated to the arrival of the first particles of the shower front at the tanks. These fluctuations, or sampling effect, increase with the distance to the shower core and decrease with the particle density, thus they dominate for stations far away from the shower core. The contribution to the variance of the start time due to the sampling effect, can be obtained from statistical models with a set of assumptions about the distribution of particles in the shower front as it is done in [16, 17] or can be computed from the actual distributions obtained from a model based on the work described in [2]. The parameterizations for the start time uncertainty proposed and tested for the Auger Observatory surface detector tanks in [16, 17] extend, in principle, to the whole zenith angle interval so they can be used, a priori, for the analysis of inclined events.

Given a normalized distribution of arrival times of the particles in the shower front, $f(t_s)$, the probability that the first particle out of n arrives before a time τ is the complementary to the probability that all the n particles arrive later than τ.

$$F_1(\tau) = 1 - (1 - F(\tau))^n \tag{3.6}$$

where $F(\tau)$ is the probability that a single particle arrives before a time τ and it is given by:

$$F(\tau) = \int_0^{\tau} f(t_s) dt_s \tag{3.7}$$

The distribution of the delay of the first particle, τ_1, is just the derivative of $F_1(\tau)$ at τ_1

$$g(\tau_1) = \left(\frac{dF_1}{d\tau} \right)_{\tau=\tau_1} = n \left(1 - F(\tau_1)\right)^{n-1} f(\tau_1) \tag{3.8}$$

Assuming different time distributions of the particles within the shower front ($f(t^s)$), the expected value and the variance of the delay of the first particle with respect to the assumed front can be evaluated directly from the previous distribution $g(\tau_1)$.

$$E[\tau_1]_{sampling} = \int_{-\infty}^{\infty} \tau_1 g(\tau_1) d\tau_1 \tag{3.9}$$

$$V[\tau_1]_{sampling} = \int_{-\infty}^{\infty} (\tau_1 - E[\tau_1])^2 g(\tau_1) d\tau_1 \tag{3.10}$$

For instance, assuming a constant rate of particles within a time interval T (box distribution), the arrival time distribution would be $f(t^s) = \frac{1}{T}$ and hence the expected value and the variance for the delay of the first particle would be:

$$E[\tau_1]_{sampling} = \frac{T}{n+1} \tag{3.11}$$

$$V[\tau_1]_{sampling} = \left(\frac{T}{n+1} \right)^2 \frac{n}{n+2} \tag{3.12}$$

Both models proposed for vertical shower analysis [16, 17] are based on this assumption of a constant rate arrival of particles. They differ on the time interval considered (T in eq. 3.11) and on the dependence on the number of particles.

The model proposed in [16] is given by:

$$V[t^s]_{sampling} \equiv V[\tau_1]_{sampling} = \left(\frac{T_{50} + C}{n+1} \right)^2 \frac{n}{n+2} \tag{3.13}$$

where n is the number of particles crossing the tank calculated from the total integrated signal and T_{50} is the risetime of the signal defined as the time it takes the integrated

signal to reach 50% of its total value. Parameter C, which will be fitted from data, gives an idea of the time interval where the bulk of particles is assumed to arrive at the tank.

The number of particles n can be estimated by:

$$n(\theta) = \frac{Signal[VEM]}{RTL(\theta)} \tag{3.14}$$

where RTL, the relative average track length at the zenith angle of the event, is the ratio of the mean track length for a given zenith angle to the mean track length for a vertical event as eq. 3.15

$$RTL(\theta) = \frac{TL(\theta)}{TL(0)} \tag{3.15}$$

The proposed variance in the start time given in [17] also based on the assumption that particles of the shower front arrive at the tanks uniformly in a given time interval is described by:

$$V[t^s]_{sampling} \equiv V[\tau_1]_{sampling} = \left(\frac{2\ T_{50}}{n}\right)^2 \frac{n-1}{n+1} \tag{3.16}$$

This parameterization, besides having a different definition of the time interval where the majority of the particles arrives at the tank, has a different dependence on the number of particles replacing n by $n-1$. This fact is irrelevant for cases when a large number of particles hits the detector, but it can be quite important for the faint signals detected far away from the shower core. This feature is crucial for inclined events because they have elongated footprints with many fired stations far from the core. A bad estimate of the start time uncertainty for these stations will bias the angular reconstruction.

Both models, instead of adding the timing variance given by eq. 3.4 to the sampling variance, build a global time variance and try to fit the free parameters introduced from twin data.

$$V[t^s] = A + B\ V[t^s]_{sampling} \tag{3.17}$$

where parameter A is directly related to the variance in the start time measurement introduced by the detector $V[t^s]_{timing}$.

There are positions in the array with two or three tanks which are only separated about $10\ m$. These tanks are refered to as *"twins"*. Being tanks in those positions

so close to each other, they can be considered to sample the same region of the air shower. Constants in the previous parameterizations are obtained by maximizing the total likelihood function 3.18 with respect to them.

$$\mathcal{L} = \prod_{i=1}^{N} \frac{e^{-\frac{(\Delta T_i)^2}{2\ V[\Delta T_i]}}}{\sqrt{2\ \pi\ V[\Delta T_i]}} \tag{3.18}$$

where i runs through all the events with twin-data information, ΔT_i is the difference between the residuals of the time fit for both stations in the pair and $V[\Delta T_i] = V[T_{i,1}] + V[T_{i,2}]$ is the total time variance given by eq. 3.17 for both stations in the pair. This likelihood function is built on the assuption that the distribution of $\Delta T / V[\Delta T]$ is gaussian.

The parameters obtained from maximizing the likelihood for the two models proposed are presented in table 3.4.

Model	Eq. 3.16		Eq. 3.13		
Parameter	$A1\ [ns^2]$	$B1$	$A2\ [ns^2]$	$B2$	$C2\ [ns]$
Value	$147\ \pm\ 17$	$0.99\ \pm\ 0.05$	$134\ \pm\ 6\ ns^2$	$2.40\ \pm\ 0.10$	$10\ \pm\ 5$

Table 3.1: Table with parameters.

From the values of $A1$ and $A2$ we see that the constant term which depends directly on the detection device is quite similar in both models and compatible with the addition in quadrature of the uncertainty given by the GPS device and by the digitizing procedure quantified around $150\ ns^2$.

Besides the two parameterizations which assume an arrival time distribution and compute the variance of the arrival time of the first particle, the variance can be also calculated directly from other distributions of the arrival times of the particles. The theoretical model proposed in [2], used to calculate the expected arrival times in the previous section, can be also used to infer the arrival time uncertainties. From the arrival time distributions we can obtain the uncertainty in the arrival time of the first muon when n muons are detected. Sampling the corresponding time distribution n times we get n arrival times out of which we can get the arrival time of the first muon. Repeating this procedure m times, we get the fluctuation, and therefore the uncertainty,

in the arrival time of the first muon out of n.

To implement these ideas one needs to know the number of particles that enter the tank from the detected signal measurement. As the signal from inclined showers is dominated by muons, we estimate this number dividing the signal by the average signal of a muon given the zenith angle and energy. A correction is applied to the signal to remove the small contribution from the electromagnetic component. With an electromagnetic signal parameterization as the one given in [21] for example, we can calculate the muonic signal and then the number of muons.

3.5 Time model

Inclined showers have to cross a very different atmospheric grammage before reaching the ground than vertical showers. As cosmic rays that initiate the air showers interact in the first layers of the atmosphere, the electromagnetic component of the shower is absorbed rapidly and inclined air showers are almost formed by muons when they reach the ground [1].

The arrival time distributions of muons described and characterized in [2] have been used in the angular reconstruction software developed for this work. These distributions at a given point are obtained from the distributions of production height, by modeling the propagation of the air shower muons through the atmosphere using simple geometrical and kinematical arguments. Two of these distributions of the arrival times are shown in fig. 3.4. For this example of a 70° zenith angle proton shower, the mean delay from the shower plane is $\approx 50\ ns$ at $1000\ m$ from the shower core and $\approx 400\ ns$ at $3000\ m$. Besides, the spread of this mean delay is also shown to increase at larger distances from the shower axis.

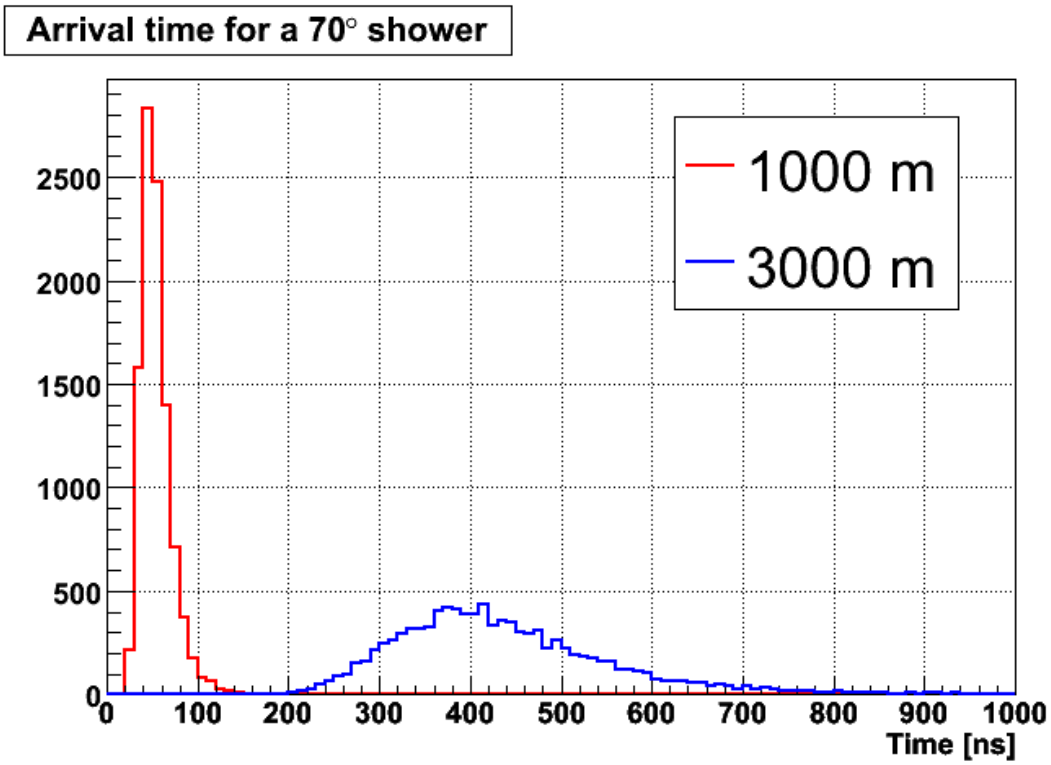

Figure 3.4: Distribution of arrival times at $1000\ m$ (red) and $3000\ m$ (blue) from the shower core for a 70° proton air shower.

The causes of the muon delays are well known and an analytic treatment of them is done in [2]. The two mean mechanisms responsible for the muon delays are the geometrical paths and the subluminal velocities. The first one is due to the deviations of muons from the shower axis and can be evaluated neglecting energy effects and assuming that muons travel in straight lines from their production points at the speed of light. This first delay is referred to as *geometrical delay*. The second one is due to the fact that muons travel at speeds lower than the speed of light. A $1\ GeV$ muon has a delay of $750\ ns$ with respect to a photon after traveling $40\ km$ in vacuum. This second sourde of delay is referred to as *kinematical delay*.

It can be seen that both, geometrical and kinematical, delays approximately behave with the distance to the shower axis as $\sim r^{\delta}$, where $\delta \sim 2$ for the geometrical delay and $\delta \sim 0.8$ for the kinematical delay. This makes the geometrical delay dominate at large distances to the shower axis as it is shown in fig. 3.5.

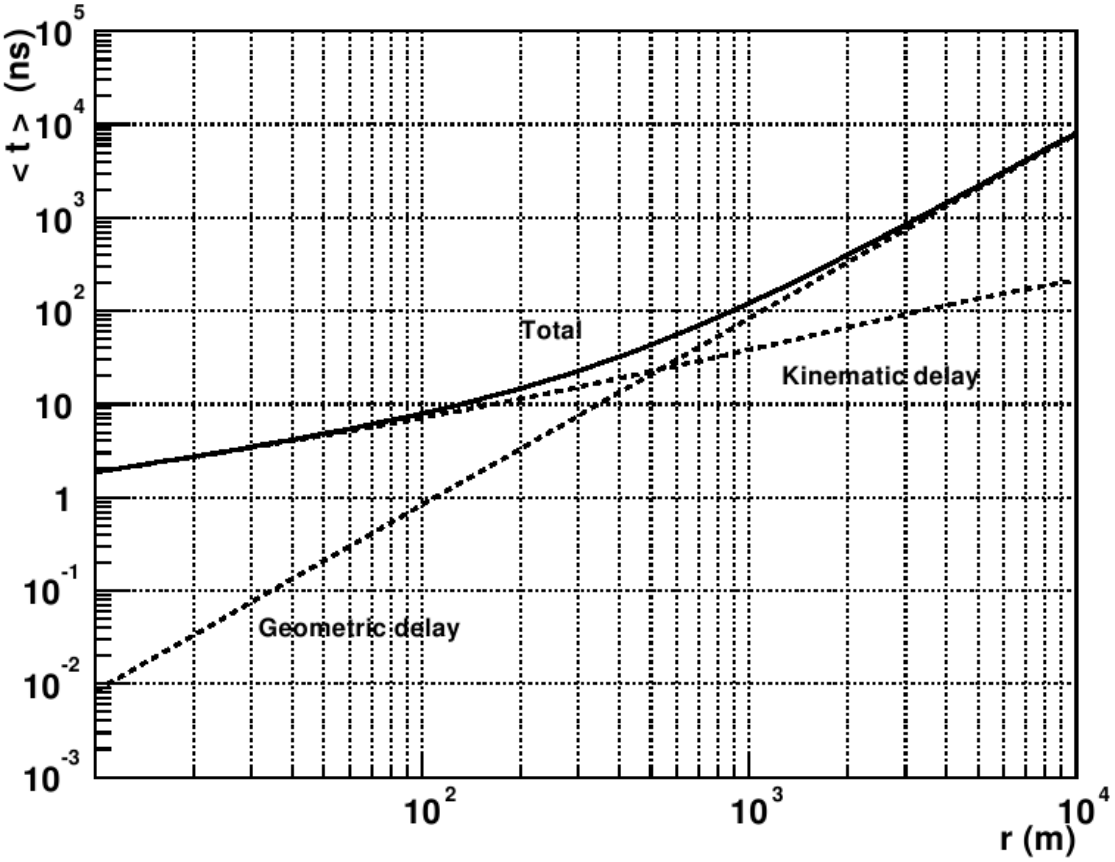

Figure 3.5: Mean muon delay from shower plane as a function of the distance to the shower core, for muons injected at 20 km altitude and its two contributions.

With the time distributions provided with the arguments of this model, the arrival time of the first muon and its uncertainty can be evaluated and used in the reconstruction of the arrival direction of the primary particle. When a surface detector tank is crossed by n muons, it actually samples the time distribution of the arriving secondary particles n times. Keeping the lowest of the n arrival times, the arrival time of the first muon out of n can be obtained. Obviously, it decreases as n increases. When a different set of n muons is chosen, this arrival time fluctuates and the uncertainty in the arrival time of the first muon can be obtained from the RMS width of the distribution of the arrival time of the first muon. The size of this fluctuation is expected to be less important than that arising from the estimate of the average time favoring the choice of the arrival time

of the first particle over the mean arrival time as an estimate of the arrival time of the shower front.

3.6 Testing variance models for inclined events with twin tanks

As it has been already mentioned, several positions of the $1.5\ km$ hexagonal grid which define the surface detector of the Auger observatory, are not only covered by one station but by two or even three tanks. These tanks, referred to as doublets or triplets, are only $\approx\ 10\ m$ far away from each other, therefore they measure roughly the same region of the shower. One of these multiplets of stations of the surface detector is shown in fig. 3.6. These tanks are one of the keys to study the variances in the start time measurement.

Figure 3.6: Picture of one of the doublets deployed around the surface array. Proximity of the tanks ensures that the same region of the shower is measured by both stations.

Inclined events with at least two tanks in one of the multiplets triggered and with a zenith angle distribution shown in fig. 3.7 have been analyzed to check the validity of the parameterizations of the start time uncertainty for inclined showers. In this analysis, triplets with all the three tanks triggered are treated as three couples of doublets. Over 5000 pairs have been analyzed.

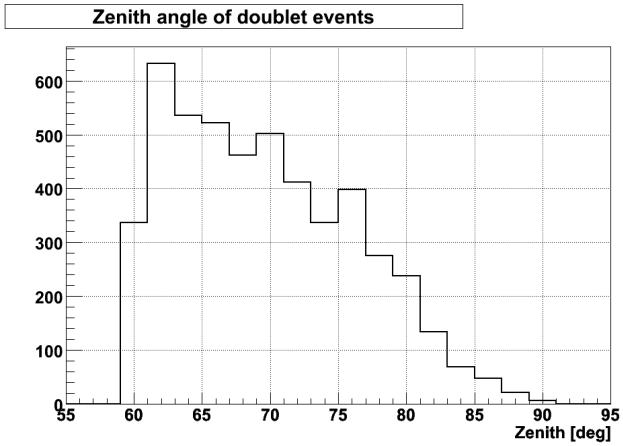

Figure 3.7: Distribution of the zenith angle of the reconstructed events with at least one doublet or triplet triggered. Both stations in the same doublet or at least two in the same triplet are requested to be fired by the shower.

Signals and distances to the reconstructed core of both tanks in the doublet and the difference between both time measurements are shown in fig. 3.8 where solid red and dashed blue lines are used respectively for the first or the second detector triggered in the pair.

From these plots, the following cuts are applied to enhance the quality of the data set getting rid of the outliers of the distributions which are assumed to be fluctuations, badly reconstructed events or events for which random muons spoil the start time determination in one or more tanks.

1. The signal in each tank must be below $500\ VEM$ to get rid of saturation effects (top panel fig. 3.8).

2. The distance of both stations to the shower core on the shower plane must be over $100\ m$ to get rid of the steepness of the lateral development of the shower close to its core (middle panel fig. 3.8).

3. The difference between start time measurements must be below $100\ ns$ to ensure that both tanks are measuring the same shower and not an isolated muon or a coinciding smaller air shower (bottom panel fig. 3.8).

Around 10% of the events are rejected when applying these cuts.

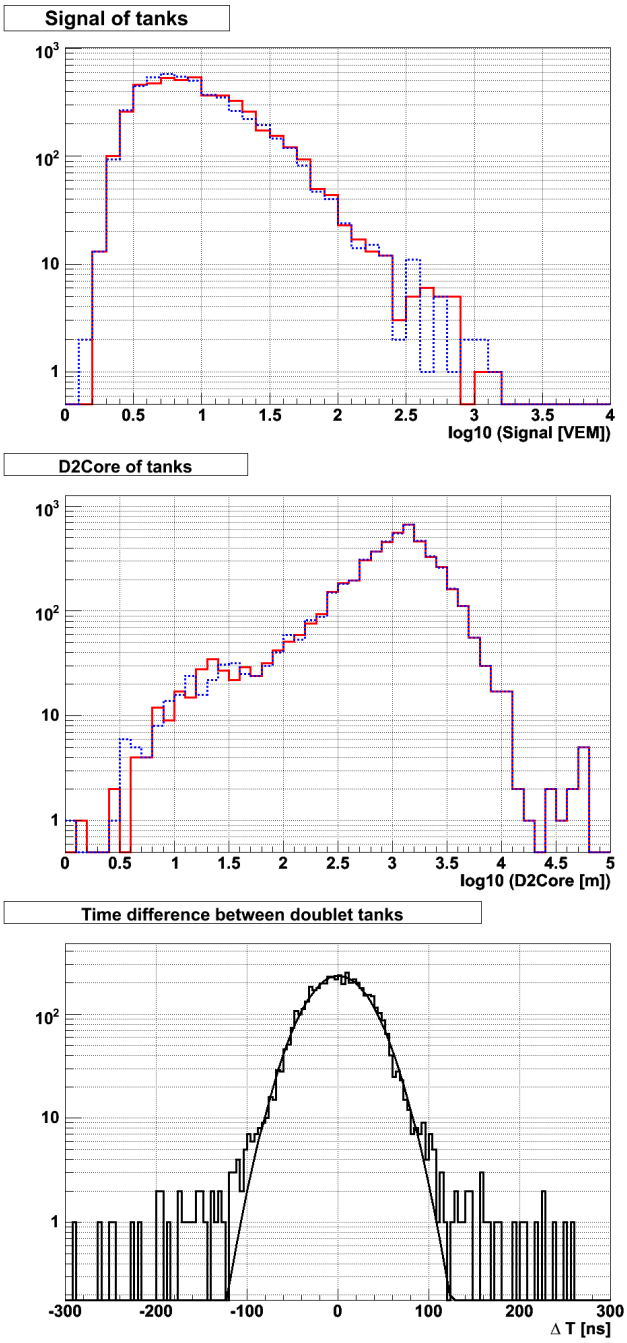

Figure 3.8: Top: distribution of the signals in each tank of the doublet. Center: distance to core distribution. Bottom: start time difference distribution.

For each model of the start time uncertainty [2, 16, 17], the difference in the residuals of the time fit is compared with the variance. The difference in the start time measurement has to take into account the shower front propagation which is model dependent whereas, as the two tanks in the doublet are close, the difference in the time fit residulas is practically independent of the shower front model assumed for the angular reconstruction and, if the uncertainties in the time measurement are correctly described, the distribution of δ defined by eq. 3.19 should have unit variance.

$$\delta = \frac{\Delta T}{\sqrt{V[T_1] + V[T_2]}} \tag{3.19}$$

where ΔT is the difference between the two residuals, and $V[T_1]$ and $V[T_2]$ are the variances for both start times predicted by the model.

Models [17] and [16] given by eqs. 3.16 and 3.13 need a first guess of the incoming direction of the shower to calculate the start time variances. These parameterizations are done on a number-of-particles basis and they use the mean track length, which is zenith angle dependent, to calculate the number of particles from the measured signals[1]. This first guess of the arrival direction has been obtained for this analysis making a time fit to a plane front with a constant start time variance of $V[T] = 625\ ns^2$.

Model [2] besides needing the incoming direction of the shower to compute the start time uncertainty also needs the core position. In this case, the shower core position is reconstructed with the algorithm used for the event reconstruction, so an iterative angular-core reconstruction is implemented. The uncertainty introduced in the measurement by the detection device has been introduced as a constant term of $20\ ns$ that has been added in quadrature to the uncertainty associated to the width of the shower front which is directly predicted by the model. This term takes into account the uncertainty introduced in the start time measurement by the light collection in the tank, by the GPS time determination and by the procedure of signal digitalization.

To check the validity of the proposed models [2, 16, 17] for the angular range of interest to the analysis of inclined events, the distribution of δ is used. This distribution is shown in fig. 3.9 for all the three models.

[1] $n = \frac{S}{RTL(\theta)}$. $RTL(\theta) = \frac{TL(\theta)}{TL(0)}$

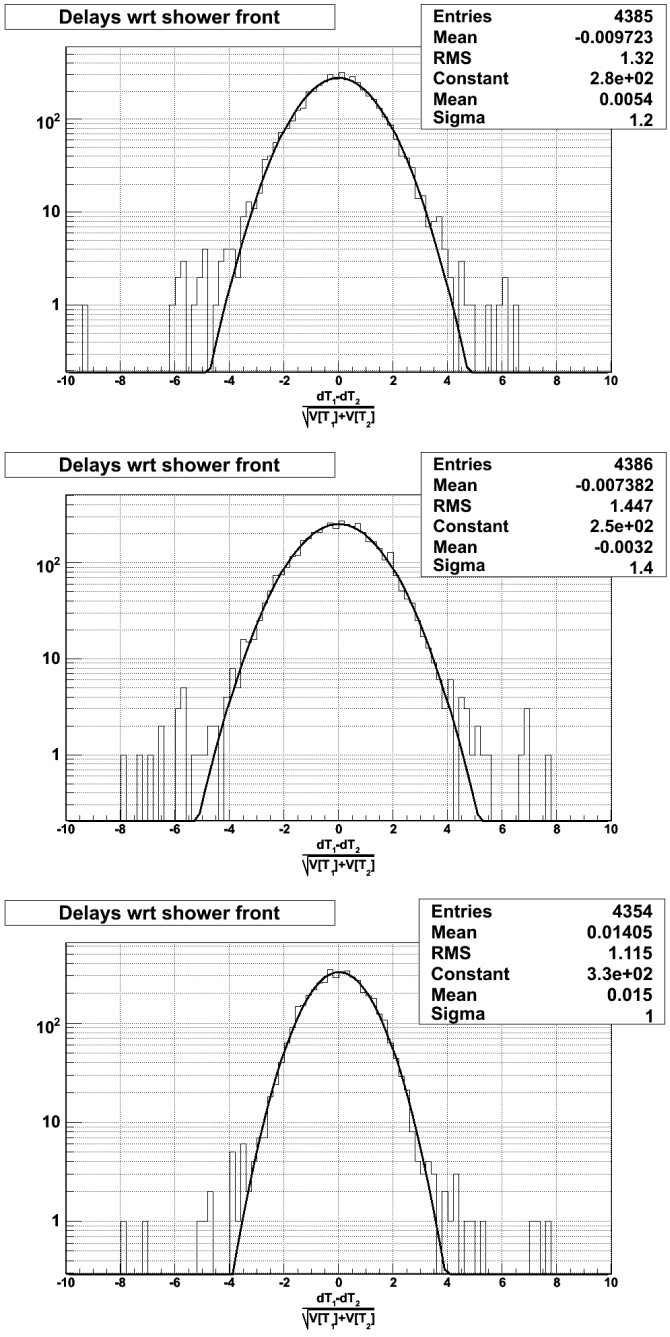

Figure 3.9: $\frac{\Delta T}{\sqrt{V[T]}}$ distribution for the three evaluated models. Top: [17], center: [16] and bottom: [2].

From plots in fig. 3.9 we see that both parameterizations from twin tanks measure-

ments (models [17] and [16]) are underestimating the start time variance for inclined events, producing a width of the δ distribution greater than one. The model based in [2] shows RMS distribution close to unity.

To validate the proposed model for different variables, we plot the width of the δ distribution as a function of the mean signal and of the distance to the core on the shower plane. In fig. 3.10 we see the flat behavior around the unit value which confirms the validity of the model for inclined events for a great range of values.

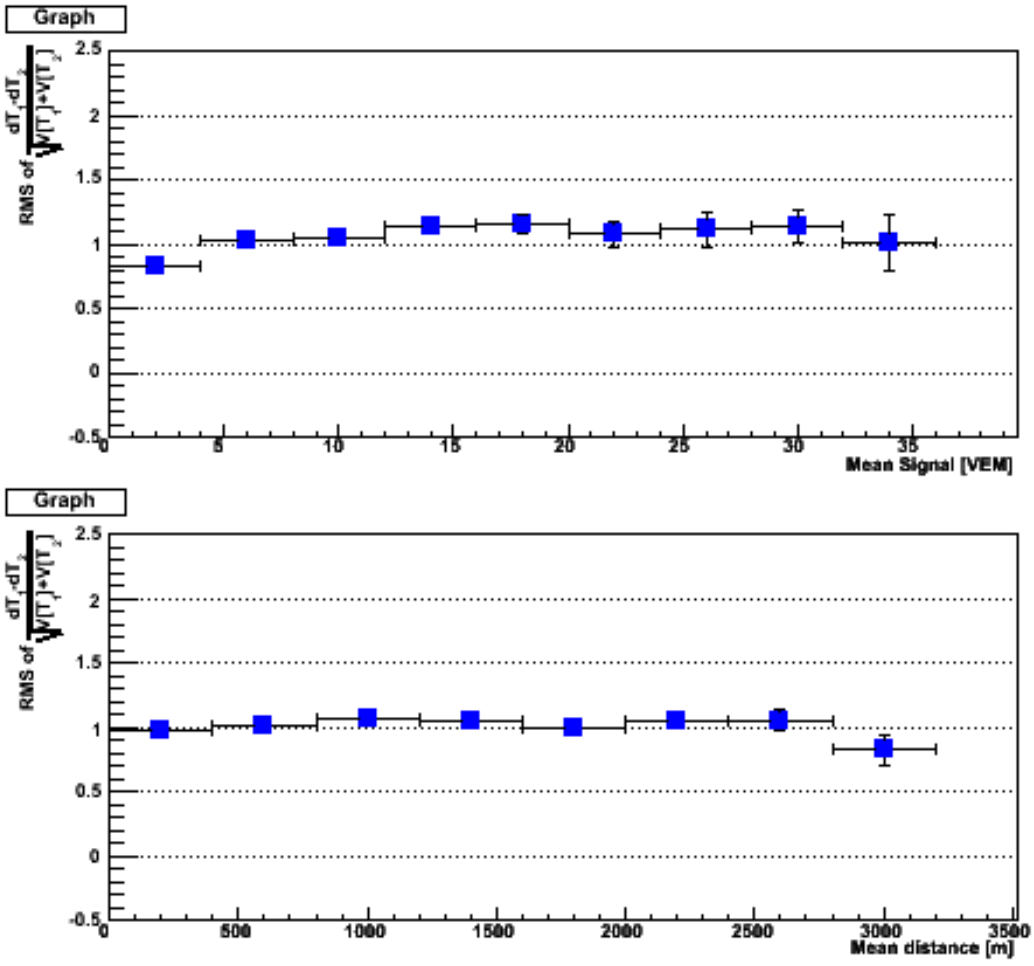

Figure 3.10: RMS of $\frac{\Delta T}{\sqrt{V[T]}}$ distribution for the [2] model. Top: signal dependence, bottom: distance to core dependence.

The RMS dependence on signal and distance to the core for models [17] and [16]

are shown in figs. 3.11 and 3.12. A worse behavior is seen for large signals and for tanks close to the shower axis.

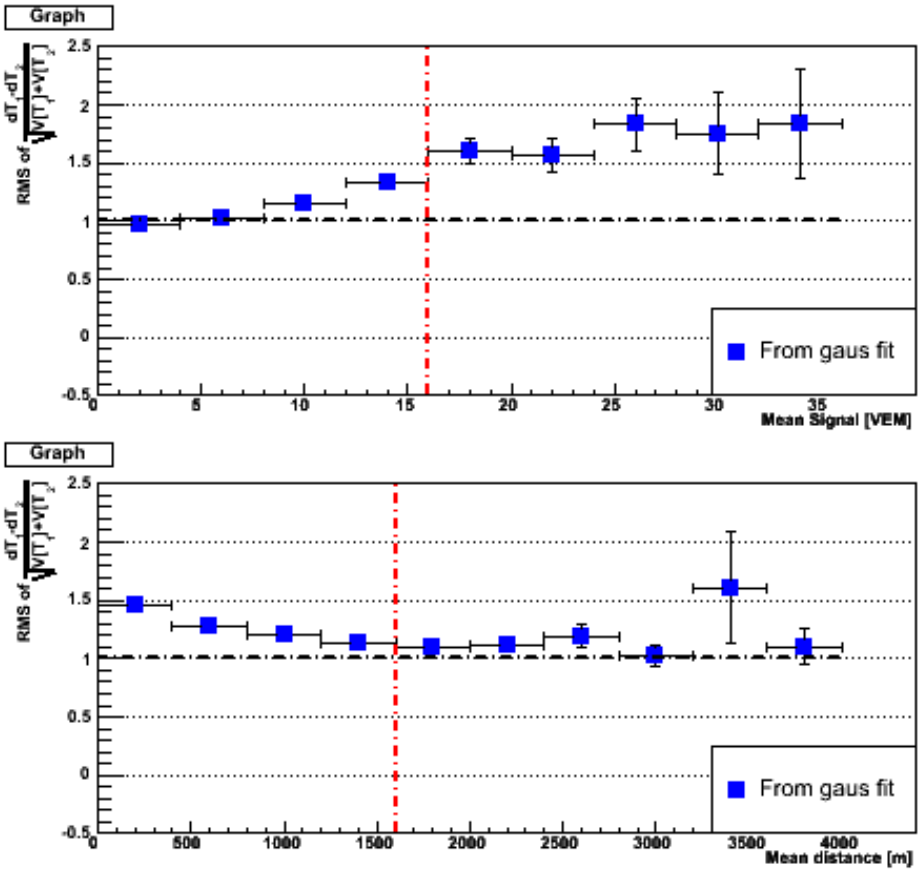

Figure 3.11: RMS of $\frac{\Delta T}{\sqrt{V[T]}}$ distribution for the [17] model. Top signal dependence, bottom distance to core dependence.

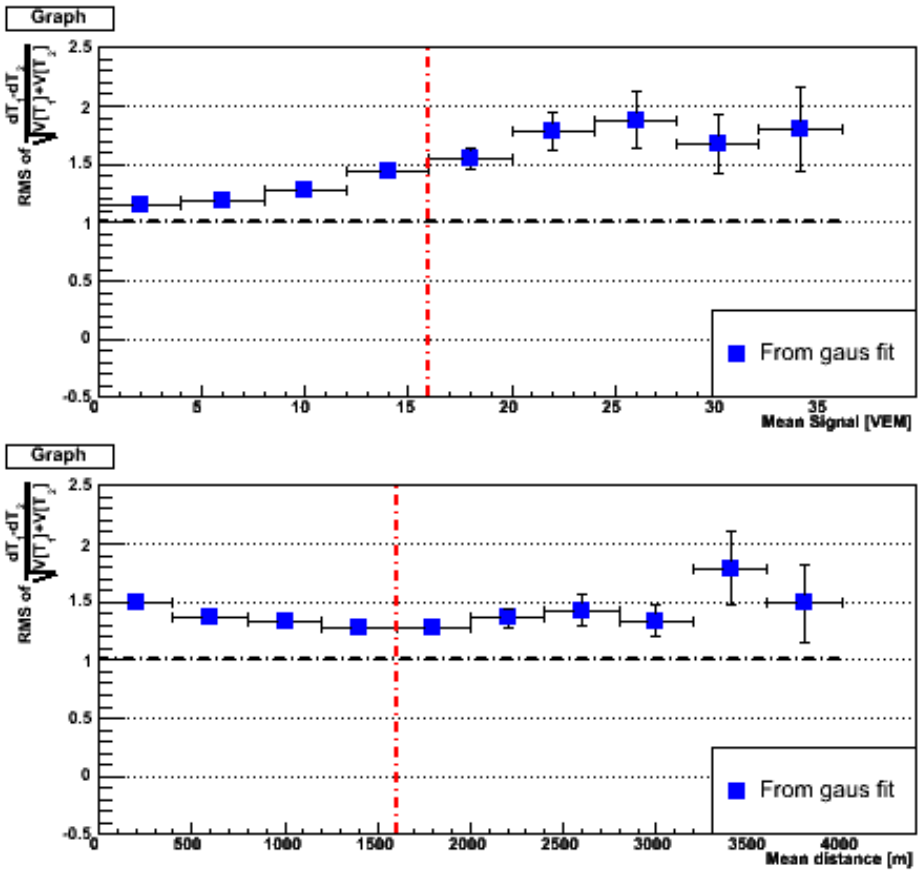

Figure 3.12: RMS of $\frac{\Delta T}{\sqrt{V[T]}}$ distribution for the [16] model. Top signal dependence, bottom distance to core dependence.

3.7 Angular resolution studies with hybrid events

A procedure to take advantage of the hybrid performance of the Pierre Auger observatory, has been set up to check the reconstruction chain. Besides, the use of high quality hybrid events, will allow us to improve the reconstruction algorithms.

To extract the angular resolution of the hybrid events, artificial showers were generated by laser shots. The Central Laser Facility, shown in fig. 3.13, is located in the middle of the array at about $30\ km$ from each fluorescence detector. It contains a remotely controlled laser which produces almost vertical showers (within $0.01°$) sending at the same time a pulse of light to a surface station to generate an artificial hybrid

event [18]. The reconstruction of laser shots is done with the same algorithm used to reconstruct real hybrid events with only one surface station. The obtained angular resolution for laser shots is $\sim 0.3^{\circ}$ [19].

Figure 3.13: The CLF with the Celeste SD station.

The laser events have geometrical characteristics that are favorable for a better hybrid reconstruction of the geometry compared to real hybrid events. The angular resolution of actual hybrid events has to be modified to account for other uncertainties arising from the particular geometry of the shower development with respect to the fluorescence detector that are ignored for laser shot events. One of them is the uncertainty of the hybrid shower axis which can be estimated as the ratio between the core uncertainty and the shower axis "lever arm"[2]. The mean accuracy for real hybrid events can be quoted as $\sim 0.6^{\circ}$ from a mean shower lever arm of $7.5\ km$ [20], so we can use the incoming direction from the hybrid reconstruction as a very good estimate of the true one and compare the SD-only incoming direction with it.

Quality cuts imposed to select high quality hybrid events are:

1. Golden events from 1st Jan 2004 to 31st May 2008.

2. FD arrival direction reconstruction from ADST v5r1.

3. Reduced χ^2 of the time fit lower than 5.

4. Zenith and azimuth uncertainties below 5°.

[2]the distance along the shower axis from ground to the point seen in the camera by the pixel with the highest elevation.

With those cuts, more than 2000 golden hybrid events are selected to test the performance of the angular reconstruction algorithms.

The comparison between zenith angles of the SD only reconstruction and the hybrid reconstruction is shown in fig. 3.14. A better resolution of the zenith angle is shown by the analysis with the curved shower front than that observed for reconstruction with a simple plane shower front.

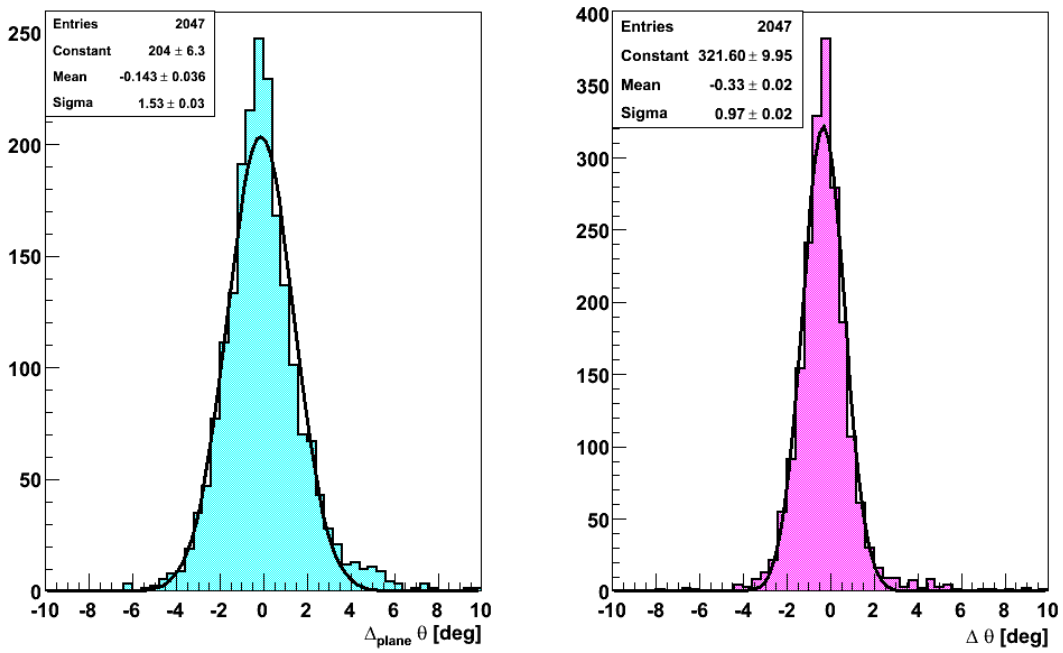

Figure 3.14: Zenith angle comparison between hybrid and surface only reconstructions. Left: plane shower front. Right: shower front with curvature and time variance from [2].

The space angle between both reconstruction is shown in fig. 3.15. The distribution has been fitted to a Gaussian resolution function $dp \propto e^{-\psi^2/2\sigma^2} d\left(cos(\psi)\right) d\phi$ where ψ is the space angle between both reconstructions. The angular resolution (AR) is related to the σ parameter as $AR = 1.5\sigma$.

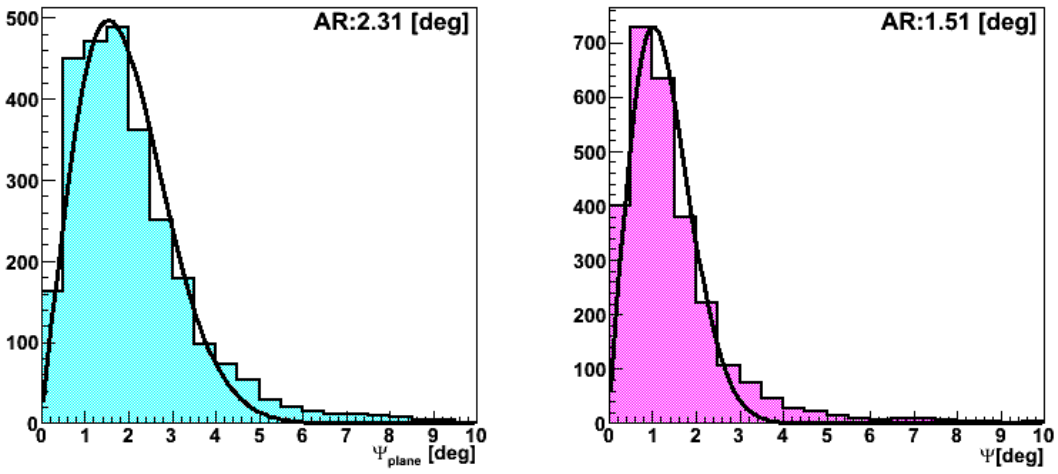

Figure 3.15: Space angle between hybrid and surface only reconstructions. Left: plane shower front. Right: shower front with curvature from [2].

Considering a resolution of $\sim 0.6^{\circ}$ for the hybrid events, the angular resolution for the surface detector can be quoted for this study as $\sim 1.1^{\circ}$.

As it is shown in fig. 3.16 no systematic is present in the space angle due to the zenith angle, the distance to the axis of the surface detector tank included in the hybrid fit, to the fluorescence eye or to the acquisition date.

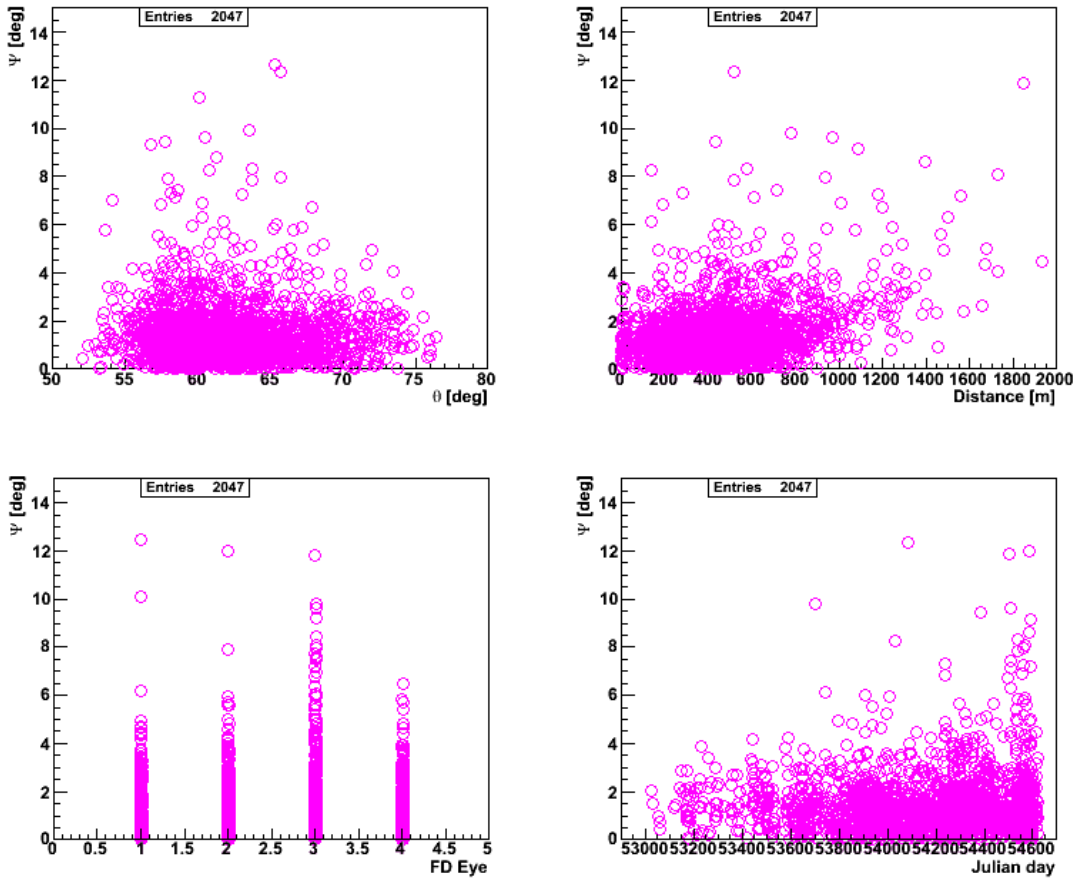

Figure 3.16: Dependence of the space angle between hybrid and surface only reconstructions. Top left zenith angle dependence . Top right: dependence on the distance to the core of the station used in the hybrid fit. Bottom left: dependence on the fluorescence eye. Bottom right: dependence on the acquisition date.

Bibliography

[1] M. Ave, R. A. Vazquez & E. Zas, Astropart. Phys. **14** (2000) 91.

[2] L. Cazon, R. A. Vazquez, A. A. Watson & E. Zas, Astropart. Phys. **21** (2004) 71.

[3] P. Bassi, G. Clark & B. Rossi, Phys. Rev. **92** (1953) 441.

[4] P. Billoir, "Reconstruction of showers with the ground array: status of the prototype program", Pierre Auger Collaboration Internal Document, GAP Note 2000-025.

[5] P. da Silva & A. Letessier-Selvon, "Status and proposal for the shower direction reconstruction", Pierre Auger Collaboration Internal Document, GAP Note 2003-012.

[6] E. Armengaud *et al.*, "Fitting a variable radius of curvature", Pierre Auger Collaboration Internal Document, GAP Note 2003-108.

[7] P. Billoir *et al.*, "A complete procedure for the reconstruction of inclined air showers", Pierre Auger Collaboration Internal Document, GAP Note 2003-003.

[8] D. Allard *et al.*, "A guide-line to the Auger surface detector analysis", Pierre Auger Collaboration Internal Document, GAP Note 2006-024.

[9] P. Billoir, "FADC trace cleaning in surface detector through a segmentation procedure", Pierre Auger Collaboration Internal Document, GAP Note 2005-074.

[10] CDAS v4r6.

[11] J. Linsley & L. Scarsi, Phys. Rev. **128** (1962) 2384.

[12] J. Linsley, L. Scarsi & B. Rossi, Phys. Rev. Lett. **6** (1961) 485.

[13] J. Linsley, J. Phys. G **12** (1986) 51 .

[14] A. M. Anokhina *et al.*, Phys. Rev. D **60** (1999) 033004.

[15] J. Abraham *et al.*, Nucl. Instr. and Meth. **A523** (2004) 50.

[16] M. Horvaj & D. Veberič, "On shower front start time variance ", Pierre Auger Collaboration Internal Document, GAP Note 2007-057.

[17] C. Bonifazi *et al.*, "A model for the time uncertainty measurements in the Auger surface detector array", astro-ph 0751856 (2007).

[18] B. Fick *et al.*, "The first Central Laser Facility", Pierre Auger Collaboration Internal Document, GAP Note 2004-003.

F. Arqueros *et al.*. "The central laser facility at the Pierre Auger Observatory", Proc. 29th International Cosmic Ray Conference, Pune-India, **8** (2005) 335.

[19] M. Monasor PhD Thesis, "Energy calibration of the Pierre Auger observatory. Measurement of the spectrum of ultra high energy cosmic rays", Pierre Auger Collaboration Internal Document, GAP Note 2008-167.

[20] C. Bonifazi *et al.*, "Angular resolution of the Pierre Auger Observatory", Proc. 29th International Cosmic Ray Conference, Pune-India, **7** (2005) 17.

[21] I. Valiño PhD. Thesis, "Detection of horizontal air showers and neutrino induced showers with the Pierre Auger Observatory", Pierre Auger Collaboration Internal Document, GAP Note 2008-024.

Chapter 4

Impact point and shower size reconstruction

Once the arrival direction of the detected shower has been determined from the time measurements as it has been described in the previous chapter, the impact point of the shower and the energy of the originating cosmic ray have to be inferred from the data. Both of them are calculated by a comparison of the measured signals with the expected ones for a certain set of tanks. This set includes at least all the triggered tanks excluding those which are rejected and several zero signal stations to better confine the core position and to avoid an artificial rise in the shower energy due to a misplacement of the shower core.

The expected signals needed for comparison are computed from simulations of air showers to obtain particle distributions at ground level and from simulations of the surface detector tank response to the passage of the particles through them. These expected signals depend on the position of the considered tank with respect to the shower core and on the energy of the cosmic ray. These dependences are used to compute the energy and the impact point of the shower by minimizing the difference between expected and measured signals or by maximizing their likelihood. The calculated magnitude is not the cosmic ray energy but the shower size related to a reference value which is obtained using $10^{19}\ eV$ proton showers. This parameter, known as $N19$, represents the relative number of muons of the detected shower with respect to the reference for the same arrival direction. $N19$ can be correlated, as it will be shown, with the fluorescence energy measurement of the originating cosmic ray using a subsample of events measured

with the two techniques.

The first model to describe the muon patterns at ground was developed within the Haverah Park experiment. It was applied to air shower data demonstrating that it was possible to measure the energy of these inclined events with a resolution comparable to that achieve for more vertical events [1, 2]. The work presented in the thesis is mainly based on this analytical model.

For inclined showers the bulk of the signal is produced by the muonic component of the shower. Shower simulations of this component are used to derive the expected muon signals. It has been shown that to a good degree of accuracy the shape of these muon distributions is fairly independent of composition and assumptions about hadronic models. In addition, the signal produced by the electromagnetic component is small, typically of order of 20% [3, 4]. This electromagnetic signal has been calculated using shower simulations, and will be introduced as a correction to the signal in relation to the expected number of muons.

The comparisons between measured and expected signals are performed in a two step process. Firstly a brute force χ^2 minimization method is used to obtain the first estimates of core position and N19. The process is later refined with a Maximum Likelihood method. These two methods are implemented one after the other taking advantage of the strengths of each one.

This chapter is organized as follows. The first two sections briefly describe both methods used to obtain the impact point of the shower and its size. Section 4.3 deals with the calculation of the expected signals through the simulations of showers, the analysis of the tank response to crossing muons and the evaluation of the electromagnetic correction. Subsection 4.3.1 is devoted to the obtaining of the expected number of muons given by a simulated proton shower; the tank response to crossing muons is described in subsection 4.3.2 and the signal correction due to the electromagnetic component in subsection 4.3.3. Section 4.4 deals with the correction in shower size due to the fact that muon maps are discretized in zenith angle and showers are reconstructed using the closest map in zenith. The check that the zenith angle dependence of the number of muons is correctly taken into account by the dependence implicit in the maps is done in section 4.5. Finally the energy calibration procedure to obtain the energy of the cosmic ray from the shower size parameter is fully described in section 4.6.

4.1 Core position reconstruction with a minimum χ^2 method

A χ^2 function between measured, S_i^{meas}, and expected signals, S_i^{exp}, is conventionally defined as:

$$\chi^2 = \sum_{i=0}^{i=n} \frac{(S_i^{meas} - S_i^{exp})^2}{\sigma_i^2} \tag{4.1}$$

where i runs through the selected stations (triggered and zero signal stations) and σ_i is the uncertainty in the signal measurement.

The expected signal depends on the shower size ($N19$) and on the relative position of the detector with respect to the shower axis as measured in a plane perpendicular to the shower front ($\hat{x}_i, \hat{y}_i$). Neglecting the dependence of the expected signal on the arrival direction, because it can be considered as an input from the angular reconstruction step, and assuming that the dependences on the primary composition and on the hadronic interaction models do not affect the shape of the particle densities, the χ^2 function can be rewritten as:

$$\chi^2 = \sum_{i=0}^{i=n} \frac{(S_i^{meas} - S_i^{exp}(N19, x_i - X, y_i - Y))^2}{\sigma_i^2} \tag{4.2}$$

$$\equiv \sum_{i=0}^{i=n} \frac{(S_i^{meas} - S_i^{exp}(N19, \hat{x}_i, \hat{y}_i))^2}{\sigma_i^2} \tag{4.3}$$

The minimization of the χ^2 function given by eq. 4.2 with respect to the three parameters we want to obtain: the position of the shower core (X,Y) and the shower size (N19), will lead to a first estimate of the values of these parameters.

The expected signal can be approximately assumed to be proportional to the expected number of muons and given that, by definition, the number of muons scales with $N19$, the shower size, we can assume that the expected signal also scales with $N19$. Searching a minimum of eq. 4.2 with respect to $N19$ we get:

$$\begin{aligned}
\frac{\partial}{\partial N19}\left(\sum_{i=0}^{i=n}\frac{(S_i^{meas}-N19S_i^{exp}(1,\hat{x}_i,\hat{y}_i))^2}{\sigma_i^2}\right) &= 0\\
\sum_{i=0}^{i=n}\frac{-2(S_i^{meas}-N19S_i^{exp}(1,\hat{x}_i,\hat{y}_i))S_i^{exp}(1,\hat{x}_i,\hat{y}_i)}{\sigma_i^2} &= 0\\
\sum_{i=0}^{i=n}\frac{S_i^{meas}\ S_i^{exp}(1,\hat{x}_i,\hat{y}_i)}{\sigma_i^2}-N19\sum_{i=0}^{i=n}\frac{S_i^{exp}(1,\hat{x}_i,\hat{y}_i)S_i^{exp}(1,\hat{x}_i,\hat{y}_i)}{\sigma_i^2} &= 0
\end{aligned}$$

$$N19=\sum_{i=0}^{i=n}\frac{S_i^{meas}\ S_i^{exp}(1,\hat{x}_i,\hat{y}_i)}{\sigma_i^2}\left(\sum_{i=0}^{i=n}\frac{(S_i^{exp}(1,\hat{x}_i,\hat{y}_i))^2}{\sigma_i^2}\right)^{-1} \tag{4.4}$$

The $N19$ value that minimizes the χ^2 as computed in eq. 4.2 can be associated to the core position using the precedent equation. Using the barycentre of the triggered tanks weighted by their signals as a first estimate of the shower core position, a search of the reconstructed core is performed around it. Sampling X and Y values across a grid around the barycentre, the $N19$ value that minimizes χ^2 according to eq. 4.4 and its associated χ^2 value according to eq. 4.2, can be calculated for each point of the grid. Two grids are set up for the search of the core position: the first one has a spacing of $50\ m$ and the second one of $20\ m$. This last choice matches the spacing used for the muon maps generation. This second minimization is not built around the barycentre but around the position in the first grid that minimizes χ^2 according to eq. 4.2. The core position (X,Y) and the associated $N19$ of this second minimal χ^2 search are used as input for the final reconstruction using the maximum likelihood method. Just as an example, a χ^2 map for a real event obtained using the grid search procedure is shown in fig. 4.1. For this high multiplicity event the minimum of the χ^2 associated with the position of the shower core is clearly visible.

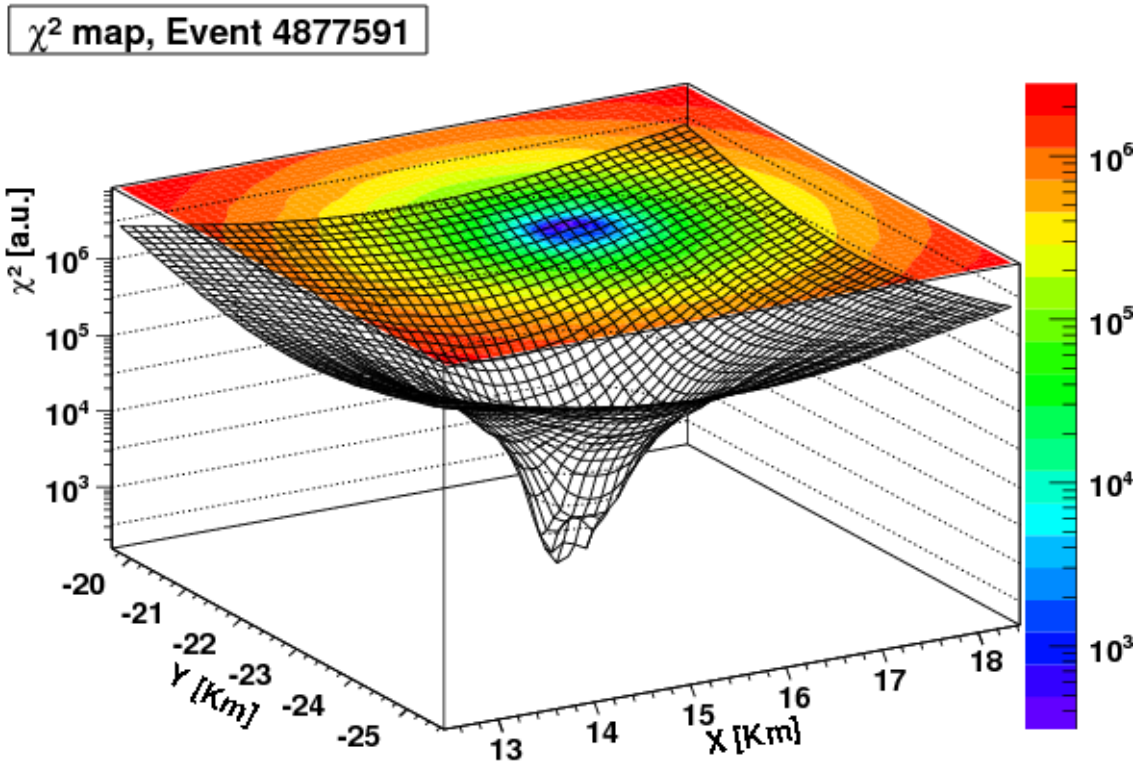

Figure 4.1: χ^2 map for a high multiplicity event resulting from the first grid search (see text) of minimal chi^2.

4.1.1 Signal uncertainty

The uncertainty in the signal measurement to be used in eq. 4.2, σ_i, can be evaluated from signal measurements of doublets as stated in [5] and parameterized for vertical showers as:

$$\sigma_i = (0.32 + 0.42 sec\theta)\sqrt{S_i^{meas}} \tag{4.5}$$

In our case, the uncertainty in the detected signal for this χ^2 method is based on the Poisson statistics on the number of muons neglecting the electromagnetic correction to the signal and it is given by:

$$\sigma_i = \sqrt{N\mu_i}\frac{S_i^{exp}}{N\mu_i} = \sqrt{TL(\theta)}\sqrt{S_i^{exp}} \tag{4.6}$$

where $N\mu_i$ is the expected number of muons, $TL(\theta)$ is the mean track length for a given zenith angle and $S_i^{exp} = N\mu_i\ TL(\theta)$ is the expected signal. The use of the expected signals instead of the measured ones is done to allow a similar treatment of triggered and zero signal stations. Predicted signals for stations far away from shower axis are not very reliable because muon density maps are restricted in size to a $8\ km \times 8\ km$ square. Outside this area the expected signal is hard to handle and it is set to zero. Typically the stations that are outside this area do not have signal and zero signal stations with a null expected signal are not included in the χ^2 calculation.

4.1.2 The barycentre as first guess of the core position

The choice of the barycentre as a first estimate of the shower core compared to the final reconstructed core is shown in fig. 4.2 where the average distance from the reconstructed core to the barycentre measured in the ground plane is plotted versus the reconstructed zenith angle for a large set of T5 events. The mean distance for all the considered events is below $500\ m$ spanning from $200\ m$ for events with a zenith angle of $60°$ to over $1500\ m$ for events with a zenith angle greater than $80°$, although the statistics rather poor above $84°$.

From fig. 4.2 we see that as the reconstructed zenith angle increases, the relation of the impact point with the barycentre of the signals is fainter. This is one of the reasons to not use the vertical definition of the highest trigger level ($T5$ or quality trigger) for inclined events.

4.1.3 Importance of zero signal stations

In the calculation of $N19$ and of the core position using the χ^2 method, zero signal stations play a very important role to confine the impact point of the showers, above all for low multiplicity events (events with a small number of tanks with signal). In fig. 4.3 χ^2 maps for the same event using and not using zero signal stations are shown. As it is clearly seen in the left panel, when no zero signal stations are used, there is a two minima structure which can lead to a bad reconstruction of the core position. The instability is

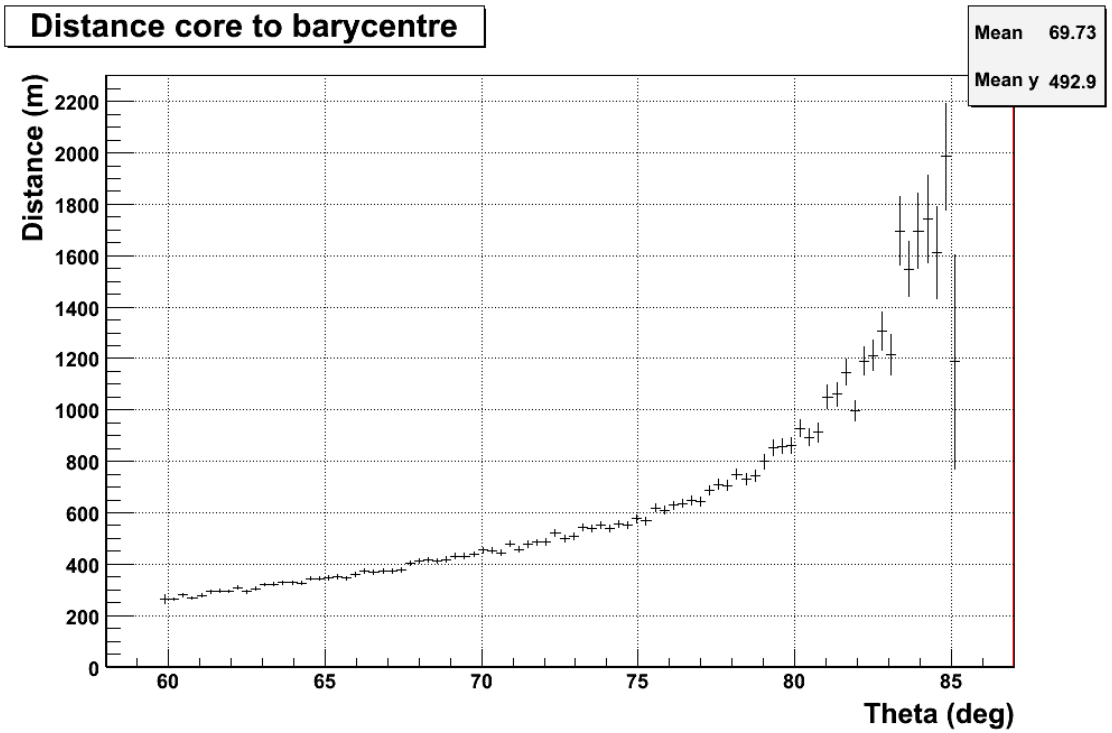

Figure 4.2: Average distance on ground of the reconstructed core to the barycentre. Barycentre of signals seems to be a good choice as a first estimation of the shower impact point at ground.

eliminated just using all zero signal stations within $1600\ m$ from all the triggered tanks. This is shown in the χ^2 map on the right panel that only displays one minimum very close to the true core position which is surrounded by the four triggered stations. This situation is rather common particularly for low multiplicity events.

Fig. 4.3 also gives a hint about the importance of the high level trigger which demands that all the stations around that closest to the shower core the core are active to ensure an accurate reconstruction. If the shower core is not surrounded by a complete hexagon of active stations, as can happen when the shower strikes the ground near the edges of the surface detector or close to a position without a working tank, the core position and hence the shower size can be misreconstructed. This situation is somehow reproduced when zero signal stations are not accounted for in the reconstruction and the undesirable result is clearly seen in the left panel of fig. 4.3.

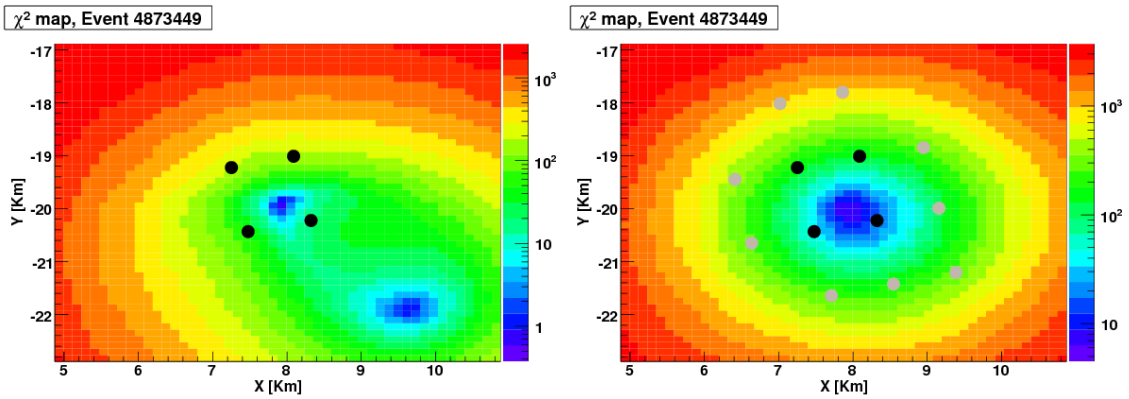

Figure 4.3: χ^2 map for $N19$ and core reconstruction without (left) and with (right) zero signal stations. Black dots are the triggered stations while the grey dots on the right panel are the zero signal stations considered in the χ^2 minimization.

4.2 Shower size estimate using maximum likelihood

The method of maximum likelihood estimation (MLE) is a statistical tool first introduced in [6] and used to calculate the best way of fitting a mathematical model to some experimental data. With this method we try to maximize a probability density which must depend on the parameters we want to obtain. In our case, where the parameters we want to obtain are the shower size ($N19$) and the position of the shower core (X,Y), this probability function is built from the product, for all the considered tanks, of the probability of having a measured muonic signal $S\mu_i^{meas}$ [1] when a number of muons $N\mu_i$ is expected.

$$\mathbb{P}(N19, X, Y) = \prod_{i=1}^{n} \mathcal{P}(S\mu_i^{meas}, N\mu_i) \tag{4.7}$$

This probability, $\mathbb{P}$, depends on the searched parameters, $N19$ and (X, Y) because the expected number of muons, $N\mu_i$, depends on them. $N\mu_i$ depends, for a given tank, on its position with respect to the shower axis measured on the transverse plane, $(\hat{x}, \hat{y})$, and on the shower size characterized by the parameter $N19$. The maximum likelihood

[1] We use the term *measured muonic signal* to refer to the muon signal extracted from measurement obtained after the electromagnetic correction has been subtracted.

procedure will search a shower size value and a shower core position that produce an expected number of muons at each station which maximizes the total probability stated in eq. 4.7.

The two dimensional distributions of the muons projected onto the transverse plane, also called muon maps, are obtained from simulations. The same assumptions made for the minimum χ^2 procedure are used here and, for a fixed arrival direction, the shape of the muon maps is assumed to be independent of energy which only affects the global normalization $N19$. Also, the shape of the maps is assumed not to depend on composition nor on hadronic models [3, 4]. We can factor out the normalization $N19$ relative to a reference distribution (see section 4.3.1).

The signal due to the muonic component, $S\mu_i^{meas}$, is obtained subtracting the average electromagnetic component in the measured signal. In this work, this is parameterized as a factor to apply to the signal, which depends on zenith angle and on the distance to the shower core, $EMCorrection(\hat{x}, \hat{y})$. It will be discussed in section 4.3.3.

$$\begin{aligned} N\mu_i \equiv N\mu_i(N19, \hat{x}_i, \hat{y}_i) &= N19\ N\mu_i(1, \hat{x}_i, \hat{y}_i) \\ S\mu_i^{meas} \equiv S\mu_i^{meas}(\hat{x}_i, \hat{y}_i) &= \frac{S_i^{meas}}{1 + EMCorrection(\hat{x}_i, \hat{y}_i)} \end{aligned}$$

The measured signal $S\mu_i^{meas}$ when $N\mu_i$ muons are expected, can be produced by different numbers of muons, each with different probability. We define $P_k(S\mu)$ as the probability distribution of k muons to produce a muonic signal $S\mu$ when traversing a surface detector tank. To compute each local probability, $\mathcal{P}(S\mu_i^{meas}, N\mu_i)$, the sum over the probabilities for all possible numbers of muons k to produce the measured signal, $P_k(S\mu)$, has to be computed. Each probability must be multiplied by the Poissonian probability of having k muons when $N\mu_i$ are expected. The overall probability becomes then:

$$\mathbb{P}(N19, X, Y) = \prod_{i=1}^{n} \mathcal{P}(S\mu_i^{meas}, N\mu_i) \tag{4.8}$$

$$= \prod_{i=1}^{n} \sum_{k=1}^{k=\infty} Poisson(k, N\mu_i)\ P_k(S\mu_i^{meas}) \tag{4.9}$$

The probability functions $P_k(S\mu^{meas})$ are discussed in section 4.3.2.

A special comment needs to be made about the treatment of zero signal stations and stations with a saturated signal. To a first approximation, only an upper o lower limit to the signal is available by the measured value of these stations.

For no signal stations, the only information we have is that the measured signal is below a trigger threshold (S_{th}) given, in principle, by the first level trigger. The contribution of a zero signal station to the total likelihood probability can be evaluated as the probability of having k muons when $N\mu$ are expected multiplied by the probability that these k muons produce a signal below S_{th}. The probability demands an integral of the probability distribution over all the possible signals below the threshold (i.e. in S):

$$\begin{aligned}
\mathcal{P}_{zero}(N\mu_i) &\equiv \mathcal{P}(S < S_{th}, N\mu_i) && (4.10)\\
&= \int_0^{S^{th}} \mathcal{P}(S, N\mu_i) dS && (4.11)\\
&= \int_0^{S^{th}} \sum_{k=0}^{k=\infty} Poisson(k, N\mu_i) P_k(S) dS && (4.12)\\
&= \sum_{k=0}^{k=\infty} Poisson(k, N\mu_i) \int_0^{S^{th}} P_k(S) dS && (4.13)
\end{aligned}$$

The $T1$ threshold is of about $1.75\ VEM$ while the ToT is $1.6\ VEM$ so the number of muons that can produce such a faint signal has to be quite low. The sum over the possible number of muons, k, in practice can be reduced to below 3. The number of stations which have no signal and are included in the fit is selected ensuring that all stations within a distance of $6700\ m$ to a triggered tank are included in the maximum likelihood fit.

When a signal is saturated, effectively only a lower limit of the actual signal is available. The probability is similarly evaluated as the probability that k muons produce a signal above $S\mu_i^{meas}$:

$$\mathcal{P}_{sat}(S\mu_i^{meas}, N\mu_i) = \mathcal{P}(S > S\mu_i^{meas}, N\mu_i) \quad (4.14)$$

$$= \int_{S\mu_i^{meas}}^{\infty} \mathcal{P}(S, N\mu_i) dS \quad (4.15)$$

$$= \int_{S\mu_i^{meas}}^{\infty} \sum_{k=0}^{k=\infty} Poisson(k, N\mu_i) P_k(S) dS \quad (4.16)$$

$$= \sum_{k=0}^{k=\infty} Poisson(k, N\mu_i) \int_{S\mu_i^{meas}}^{\infty} P_k(S) dS \quad (4.17)$$

Saturated signals are likely to be produced by large numbers of muons. As will be shown, $P_k(S\mu)$ can be accurately approximated by a Gaussian function for $k > 8$. Besides, the Poissonian distribution can be also approximated by Gaussian distribution for k high enough and hence this integral can be parameterized as:

$$\mathcal{P}_{sat}(S\mu_i^{meas}, N\mu_i) = \frac{1}{2}\left\{1 - tgh\left[\frac{S\mu_i^{meas} - S\ N\mu_i}{2\ S^2\ \sqrt{N\mu_i}}\right]\right\} \quad (4.18)$$

Saturation effects could arise from saturation of the sampling ADC and/or of the PMT. The first one occurs at typically $\rho \approx 100\ VEM/m^2$ and the second one at $\rho \approx 500\ VEM/m^2$. A procedure to take into account these two kinds of saturation effects and to deduce the actual signal from the FADC trace obtained has been developed in [7] but it has not been used in this work. Saturated signals have been treated as lower limits of the measured signals.

In the implementation of this method we minimize the opposite of the natural logarithm of the total probability. The upper limits of the involved summations are truncated to reduce computation time.

$$-log(\mathbb{P}) = -\sum_{i}^{n} log(\mathcal{P}(S\mu_i^{meas})) \quad (4.19)$$

$$= -\sum_{i}^{n} log(\sum_{k=l-lim}^{k=u-lim} Poisson(k, N\mu_i)\ P_k(S\mu_i^{meas})) \quad (4.20)$$

Fig. 4.4 shows the likelihood function behavior around the minimum for two real

events.

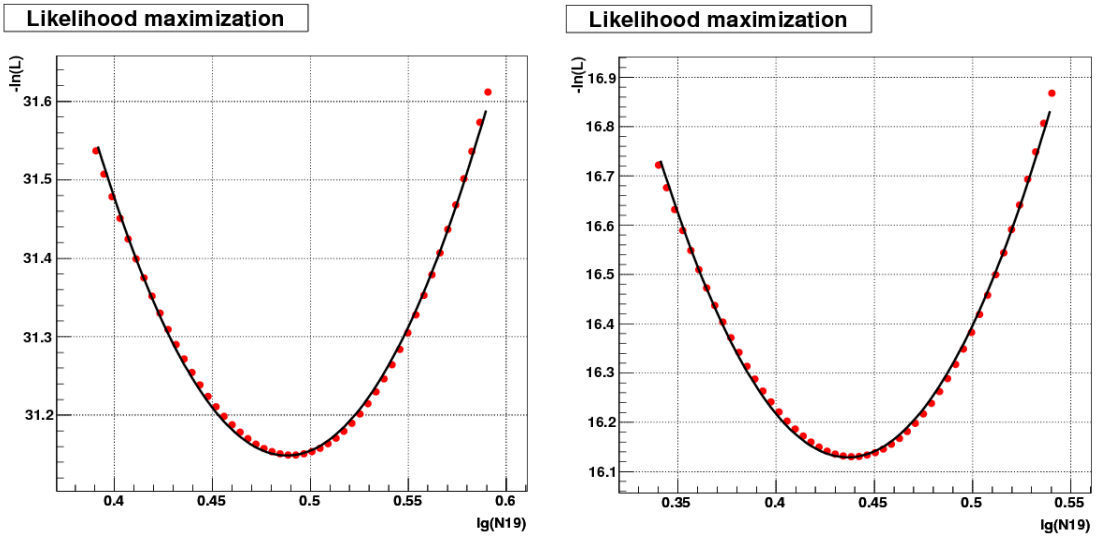

Figure 4.4: Likelihood function maximization for two events detected by the Auger surface detector. The negative of the natural logarithm of the likelihood function is minimized with respect to the logarithm of the size parameter $N19$.

The impact of zero signal stations in the likelihood maximization is shown in fig. 4.5. Besides an overall decrease in absolute P for the event which is irrelevant, we note that adding zero signal stations has a significant effect on the extracted shower size. For the event shown, zero signal stations represent a reduction of over $\sim 20\%$ in the $N19$ estimate. This is characteristic of the lower energy events[2].

[2] GAP note in progress

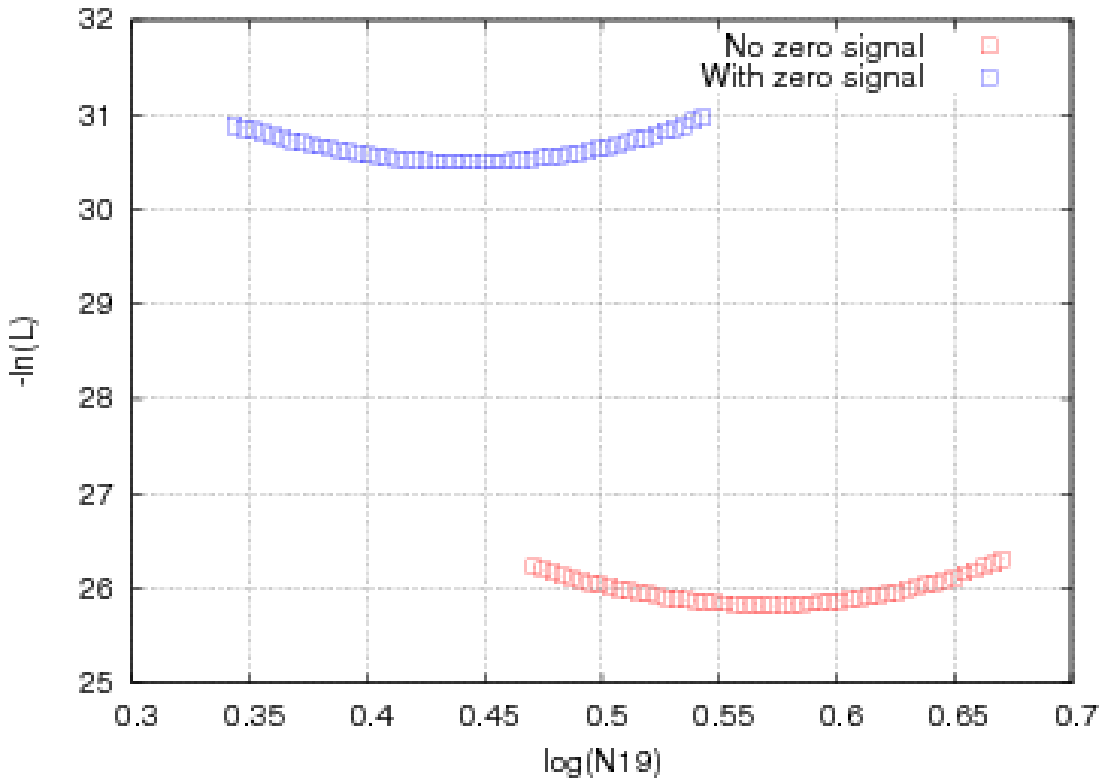

Figure 4.5: Comparison between likelihood maximization with (blue) and without (red) zero signal stations is shown. A reduction of $\sim 20\%$ in the $N19$ estimate can be observed for this event.

4.3 Calculation of the expected signal

The expected signals are needed for the comparison with measured ones in the χ^2 minimization or to evaluate the probabilities of having a given measured signal needed in the maximum likelihood method. They are obtained from the expected number of muons and from the signal that they produce traversing an surface detector tank. The minimization of the χ^2 given by eq. 4.2 only needs the mean signal produced by an expected number of muons and its uncertainty while for the maximum likelihood method the complete signal probability distribution for this number of muons has to be given to construct the complete probability function as stated in eq. 4.7.

4.3.1 Muon maps

A two dimensional distribution is needed to predict the expected signals in each tank. Muon density maps allow to compute the expected number of muons at any given point from the shower axis. This is because there is a loss of cylindrical symmetry mainly due to the magnetic field bending of particles as they travel through the atmosphere. This loss makes the algorithm used to measure the size of vertical showers [8] unsuitable for the analysis of inclined air showers.

Several methods are available to produce these maps from air shower simulations through different procedures as described in [1], [9] and [10]. In this work, a set of muon density maps based on pioneering work of ref. [1] has been generated in [11]. This can be converted to the expected number of muons in a tank multiplying the muon number density given by the maps by the projected area of the tank in the plane perpendicular to the arrival direction. The number density depends on zenith, azimuth and distance to the shower core.

In absence of the magnetic field of the Earth, they have, to an excellent approximation, cylindrical symmetry on the plane perpendicular to the shower axis called (transverse plane) as it is shown in the left panel of fig. 4.6. The two dimensional distributions are generated applying the deviations due to the Earth's magnetic field to muon distributions generated without the magnetic field using the anticorrelation between the average muon energy and the distance to the shower axis, shown in the right panel of fig. 4.6, and assuming that muons are produced in a fixed region of the atmosphere. The magnetic bendings are introduced considering the projection of the Earth's magnetic field onto the transverse plane and analytically calculating the deviations to obtain the muon densities.

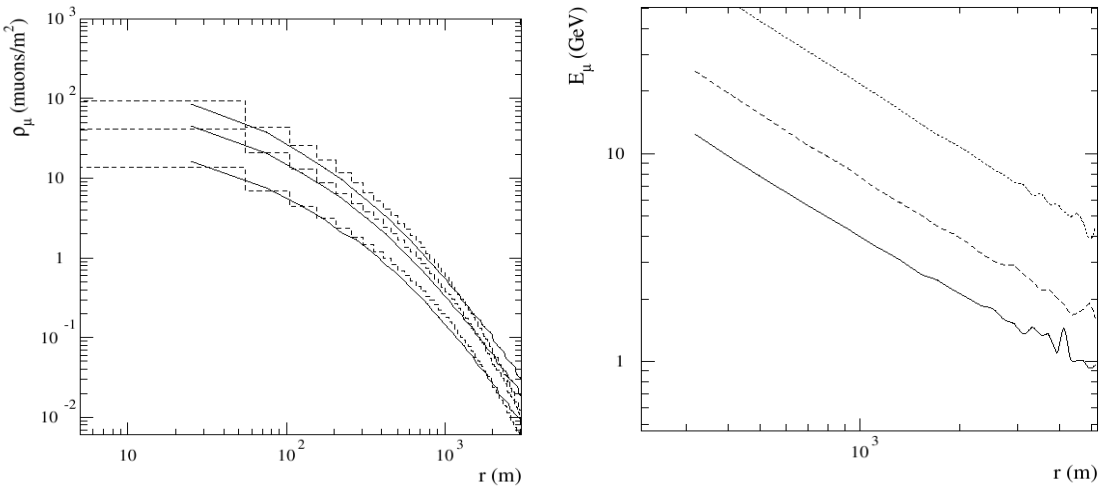

Figure 4.6: Inputs for muon maps generation taken from [1]. Left panel: Lateral distribution of muons from simulations (histograms) and from the model (continuous lines). Different sets of lines correspond from top to bottom to zenith angles of $60°$, $70°$ and $80°$. Right panel: Average muon energy as a function of the distance to the shower axis. Different figures correspond from bottom to top to zenith angles of $60°$, $70°$ and $80°$.

For practical purposes the implementation of the analytic densities provided by the model requires lengthy integrations and muon maps have been generated binning the results for different zenith and azimuth angles in a $20\ m \times 20\ m$ grid. Each histogram spans an area of $4\ km \times 4\ km$ on the shower plane. Stations further away from the shower core are assumed to expect no muons. Maps are generated in steps of $2°$ in zenith (from $60°$ to $88°$) and in steps of $5°$ in azimuth given a total of 1080 maps.

In fig. 4.7 four muon density maps out of the set used for reconstruction are shown for four different zenith angles but for the same azimuth configuration. The bending of the muons caused by the Earth magnetic field can be easily noticed particularly at high zenith angles where a two lobed pattern is clearly visible. This pattern corresponds to the total separation of positive and negative muons produced by the magnetic field.

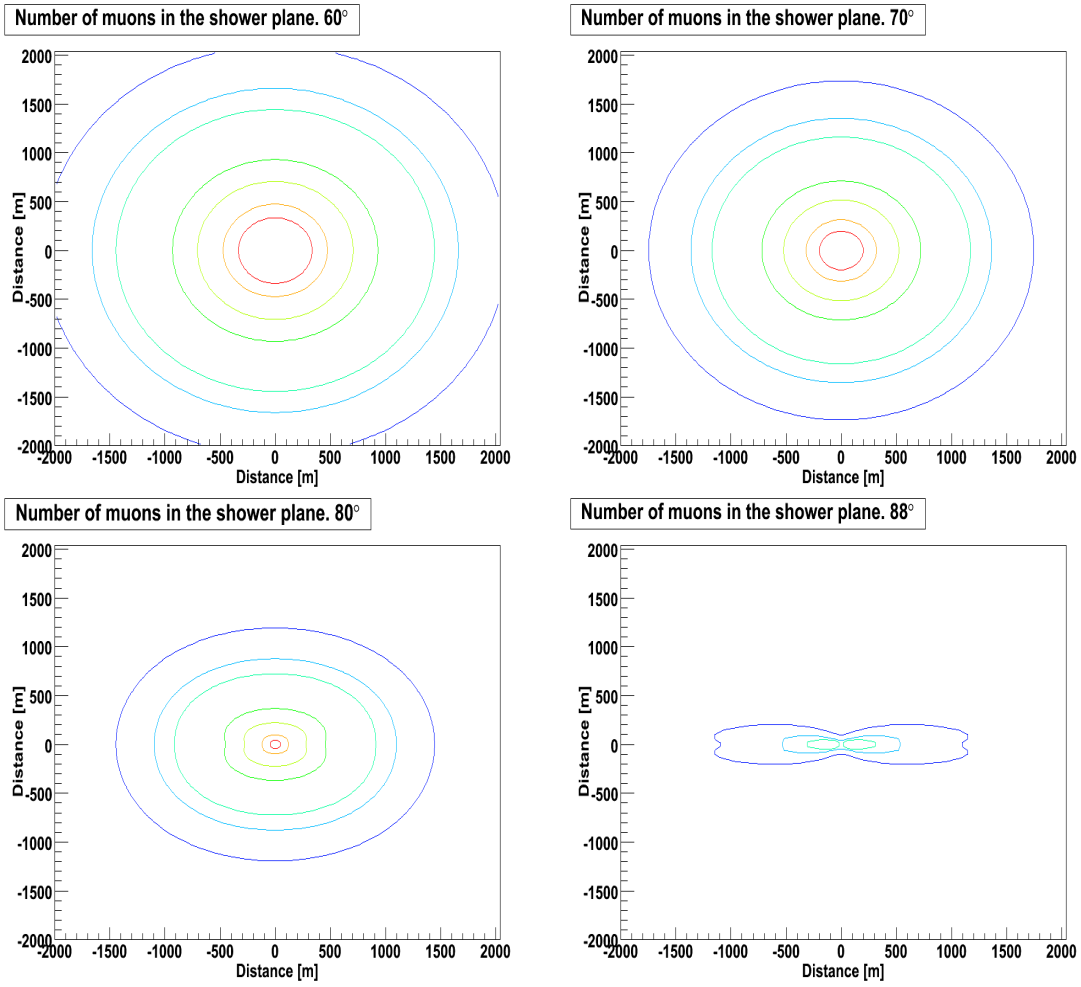

Figure 4.7: Muon maps for 60, 70, 80 and 88 degrees. Several equal-density contours are also plotted. Dark blue: 1 $muon\ m^{-2}$, green: 10 $muon\ m^{-2}$, red: 100 $muon\ m^{-2}$, etc.

The shape is pretty independent of the primary mass and of hadronic model [3, 4]. The only asymmetry in the maps obtained with the mentioned procedure is due to the magnetic field. Due to the differences in the path lengths traveled by the muons in the early and in the late region, there is an additional asymmetry caused by the muon decay [11]. This asymmetry increases with zenith angle as the path length difference also rises. As a first approximation a multiplicative factor that depends on the azimuth angle on the transverse plane, ζ, and on the zenith angle, θ, and it can be introduced

in the muon maps taken from [12] as:

$$\rho_A(x,y) = \rho(x,y) \int d\epsilon P(\epsilon, <\epsilon>, \sigma) \left(\frac{E}{E + \rho\ a\ \Delta} \right)^{\kappa} \tag{4.21}$$

where $\rho_A(x,y)$ ($\rho(x,y)$) is the muon density with (without) the early-late asymmetry accounted, $P(\epsilon, <\epsilon>, \sigma)$ is the probability distribution that muons of average energy $<E>$ have an energy ϵ, $\rho\ a = 2 \cdot 10^{-3}\ GeV\ m^{-1}$, $\Delta = r\ cos(\zeta)\ tan(\theta)$, and $\kappa = 0.8$. This correction has not been used in this work.

Other muon maps are available for the reconstruction of inclined events, those generated by the IPN Paris group [9] and those obtained by the Aachen group [10]. They differ in the way of treating the muons in the simulation and how the final maps are produced. Maps from [9] have been also generated using the shower Monte Carlo code AIRES [13] whereas maps from [10] have been generate with the CORSIKA Monte Carlo [14] and using QGSJet-II as high energy interaction model. These two sets of maps have the early-late asymmetry in the signal included by construction. A summary of several features of the three sets is given in table 4.3.1.

	USC	Paris	Aachen
Shower Monte Carlo	AIRES	AIRES	CORSIKA
High energy interaction model	QGSJet01	QGSJet01	QGSJet-II
Early-late asymmetry	NO	YES	YES
Maps generation	Simulation without magnetic field adding deformations by analytical model	Monte Carlo for muon propagation	Full shower simulation

Table 4.1: Comparison of the available muon maps.

4.3.2 Tank response to crossing muons

Once the number of muons expected at a given position is known from the muon density maps, the response of the detector to these muons has to be calculated. The mean and the uncertainty of the signal produced when k muons enter the tank are needed for χ^2 minimization and the probability distribution of signals produced by k muons must be obtained for the maximum likelihood method. The simulation of the response of the

surface detector tanks to crossing muons was made in 2005 and is described in [11] where details about the computation of these three inputs for the reconstruction are given. We summarize the result used here. An update of the simulation of the tank response is currently underway (GAP note in progress). The histograms that have been computed so far using the latest version of the Offline[3] indicate results completely consistent with the older ones used throughout this thesis.

1. Signal probability distribution for single muons

   To obtain these distributions the fundamental function is $P_1(S\mu)$, the probability distribution to have a muonic signal $S\mu$ when 1 muon enters the tank. This distribution depends on the zenith angle of the incoming muon and on its energy. The more inclined the incoming direction of the muon to the tank, the larger is the average track length and the more Cherenkov light will be produced giving rise to a higher signal in the tank. In addition, as the zenith angle rises, the muon energy increases. This leads to a higher number of hard processes such as bremsstrahlung or pair production what contributes to increasing also the produced signal by adding long tails to the distribution [11].

   This probability function has been obtained using GEANT4 package [15] as described in Appendix B of [11]. The distributions are avaliable for 16 zenith angles (60° to 90° in steps of 2°) and 10 muon energies (1 GeV, 3 GeV, 5 GeV, 10 GeV, 20 GeV, 50 GeV, 75 GeV, 100 GeV, 500 GeV and 1000 GeV).

[3] The official simulation code of the experiment.

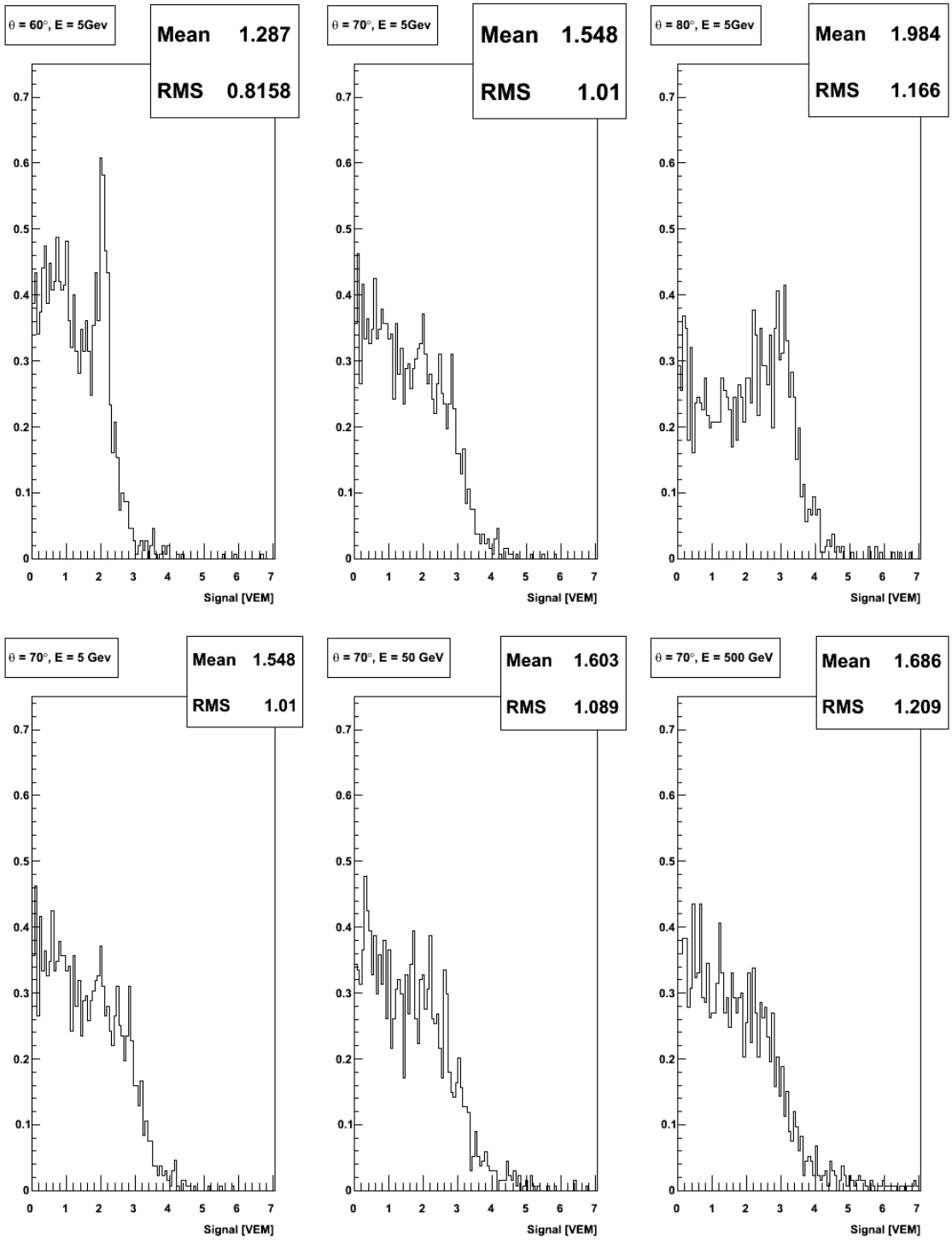

Figure 4.8: Top: signal probability distributions for a single $5\ GeV$ muon entering the tank with a zenith angle of $60°$ (right), $70°$ (center) or $80°$ (left). Bottom: signal probability distributions for a single $70°$ muon entering the tank with an energy of $5\ GeV$ (right), $50\ GeV$ (center) or $500\ GeV$ (left).

2. Signal distribution probability for k muons.

   To calculate the signal probability when k muons enter the tank, $P_k(S\mu)$,we have to perform the autoconvolution of the probability distribution function of a single muon.

$$\begin{aligned} P_2(S\mu) &= \int_0^\infty dS' P_1(S'\mu) P_1(S\mu - S'\mu) \\ \cdots &\quad \cdots \\ P_k(S\mu) &= \int_0^\infty dS' P_1(S'\mu) P_{k-1}(S\mu - S'\mu) \end{aligned}$$

   Although the shape of the signal probability for a single muon is complicated, the function rapidly becomes Gaussian allowing a simple parameterization of its mean value and its width as functions of the number of muons. We have chosen to use the gaussian approximation when the expected number of muons is greater than 8.

$$P_k(S\mu) = Gauss(\zeta_k(E,\theta), \sigma_k(E,\theta)),\ if\ k > 8 \tag{4.22}$$

   As it is shown in [11], on the one hand, the mean signal of k muons, $\zeta_k(E,\theta)$, grows linearly with the number of muons, k,for fixed zenith angle and energy. On the other hand, its uncertainty, $\sigma_k(E,\theta)$, grows with its square root. The normalization of these dependences are functions of the zenith angle and of the muon energy that can be factorized. The mean and width of the gaussian can be parameterized as follows:

$$\zeta_k(E,\theta) = f_1(E)\ TL(\theta)\ k \tag{4.23}$$

$$\theta_k(E,\theta) = f_2(E)\ \sigma^2_{TL}(\theta)\ \sqrt{k} \tag{4.24}$$

   where k is the number of muons, E is their energy, θ is the entering zenith angle, $< TL >$ is the mean track length at that zenith, σ^2_{TL} is the track length variance

and f_1 and f_2 are two energy dependent expressions given by:

$$f_1(E) = 0.92 + 0.085\ log_{10}(E) \quad (4.25)$$

$$f_2(E) = 0.23 + 0.052\ log_{10}(E) \quad (4.26)$$

4.3.3 Electromagnetic part of the signal

Signals produced at the surface detector tanks are dominated by muons in horizontal showers. The electromagnetic component due to the π^0 decays is almost completely absorbed before reaching the ground particularly for angles above 65°. In any case, this component remains typically at low distances to the shower axis. In addition, there is a small electromagnetic component in inclined showers due to muon decay and to hard muon interactions. This component, that contributes typically about 20% of the muonic signal [1] has been studied in [16]. Both the size and its two dimensional behavior have to be taken into account. The measured signal is corrected subtracting the electromagnetic correction to obtain the muonic signal in order to compare the muonic signal measured to that expected according to the prediction for the number of muons.

The electromagnetic component due to muon decay has been shown to follow the two dimensional distribution of the muons [1]. The signal induced by the electromagnetic component was parameterized taking the ratio of the electromagnetic signal, S_{EM}, to the muonic signal, S_μ as a function of the zenith angle and on the distance to the shower axis. The parameterization of this ratio [16], is obtained using shower simulations with $AIRES$ and a tank simulation code called $S1000\ USC$ also described in that work.

In fig. 4.9 the ratio of electromagnetic to muonic signal is shown as a function of the distance to the shower axis for several zenith angles. On the one hand, close to the shower core, this ratio decreases with zenith angle up to 72° increasing again from there. This behavior is due to the π^0 shower component which rapidly attenuates as the zenith angle increases from 60° to 72° to be taken over by the hard muon processes that dominate the electromagnetic signal close to the shower core for very inclined showers. On the other hand, far from the shower core, the contribution of the electromagnetic component is only due to muon decay and becomes practically constant.

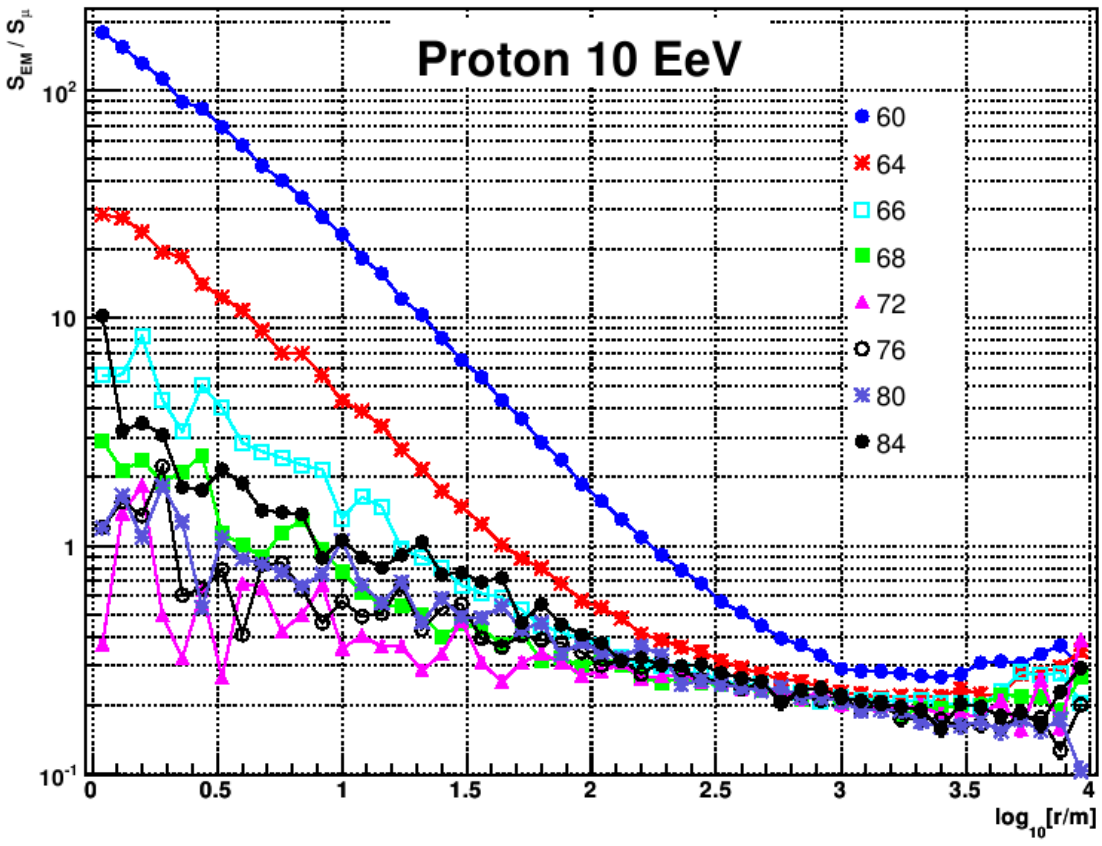

Figure 4.9: EM ratio.

A simple parameterization of this ratio has been made in [16]:

$$\frac{S_{EM}}{S_\mu}(r,\theta) = A(\theta)\ r^{C(\theta)} - B(\theta)\log_{10}(r) \tag{4.27}$$

The assumption that the ratio $\frac{S_{EM}}{S_\mu}$ is equal at the same distance from the shower axis in the shower plane regardless of the azimuthal angle is only an approximation. There is an azimuthal asymmetry in the signal due to the several effects, the most important are the so-called geometrical effect, the longitudinal development effect and ground screening [17]. At $\theta > 60°$ there is a small early-late asymmetry in the muonic signal that increases slowly with distance to the core. This is due to the long attenuation length of the muons in the atmosphere. At $\theta < 70°$ there is an important early-late asymmetry in the EM signal that increases rapidly with the distance to the shower axis. However,

at $\theta > 70^{\circ}$, the asymmetry increases slowly with the distance to the core in the same way as the asymmetry in the muonic signal since the EM component comes mainly from muon decay. The ratio $\frac{S_{EM}}{S_{\mu}}$ has a clear azimuthal asymmetry at $\theta < 70^{\circ}$ in agreement with the asymmetries obtained for the muon and electromagnetic components. The ratio with these effects taken into account has been also parameterized in [16] as:

$$\frac{S_{EM}}{S_{\mu}}(r,\theta,\zeta) = \frac{S_{EM}}{S_{\mu}}(r,\theta)\,(1 + A_{asym}(r,\theta,\zeta)) \tag{4.28}$$

where θ is the zenith angle of the shower, ζ is the azimuth angle in the shower plane, r is the distance to the shower axis, $\frac{S_{EM}}{S_{\mu}}(r,\theta)$ is given by eq. 4.27 and the parameter A_{asym} characterizes the azimuthal asymmetry. This correction is has not been used in this work. The effect of the magnetic field in this parameterization has also been studied in [16] can be introduced a posteriori. It is negligible below 80° although its effect can be greater than 20% for showers with a zenith angle over 86°. It is neglected in this work. In addition, the electromagnetic correction changes with model, compositions and with energy. A systematic study of these effects is in progress but will not be reported in this thesis.

4.4 Size correction due to the binning in the muon maps

Muon maps are binned for practical reasons, so detected showers are reconstructed using the available map closest to the zenith angle of the shower. As the shower size drops with zenith angle in an implicit way for each set of maps, a correction factor, κ, must be included in the analysis to account for this effect due to the difference between the reconstructed zenith angle and the zenith angle of the used map. As a result, the $N19$ value for a shower arriving with a zenith angle θ and with a reconstructed shower size of $N19_{rec}$ computed with a map generated with a zenith angle of θ_{map} can be obtained from the expression:

$$N19 = \frac{N19_{rec}}{\kappa(\theta,\theta_{map})} \tag{4.29}$$

The parameterization of the κ factor has been obtained for the set of muon maps used

in this work directly from full Monte Carlo air shower simulations by comparing the total number of muons as a function of the zenith angle for simulated showers of the same energy. In fig. 4.10, a parameterization of the total number of muons with respect to a $60°$ shower is plotted versus the zenith angle. As an example, all the detected showers with a zenith angle between $63°$ and $65°$ (dashed red lines) will be reconstructed with the $64°$ map. As the total number of muons of a $63°$ ($65°$) shower is greater (smaller) than that of the used map, the size parameter obtained will be then smaller (greater) than the true one and hence the correction factor κ will be greater (smaller) than one for reconstructed zenith angles below (above) the nominal value of the used map.

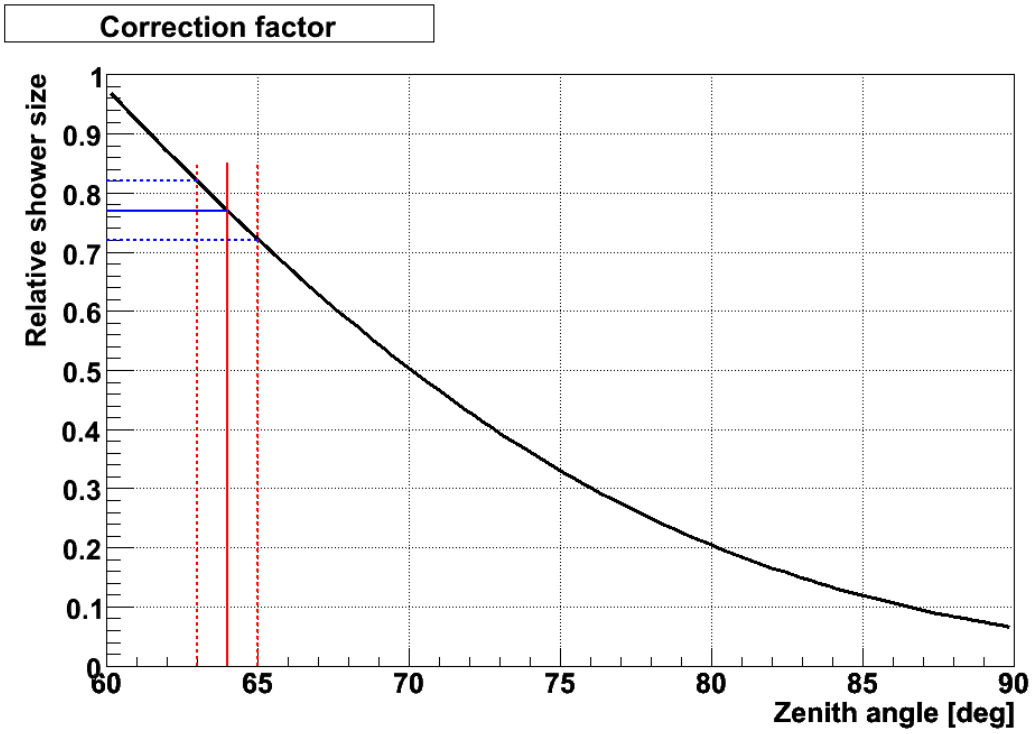

Figure 4.10: Attenuation of the total number of muons from maps.

The correction factor to be applied in each case shown in fig. 4.11 can be parameterized as follows:

$$\kappa(\theta, \theta_{map}) = 10^{d(\theta)-d(\theta_{map})} \tag{4.30}$$

where

$$d(\theta) = a + b\,[1 - \cos(\theta)] + c\,[1 - \cos(\theta)]^2 \tag{4.31}$$

and $a = 0.395$, $b = -0.04$ and $c = -1.54$. The correction factor increases for larger zeniths and reaches over 12% for very inclined events as it is shown in fig. 4.11.

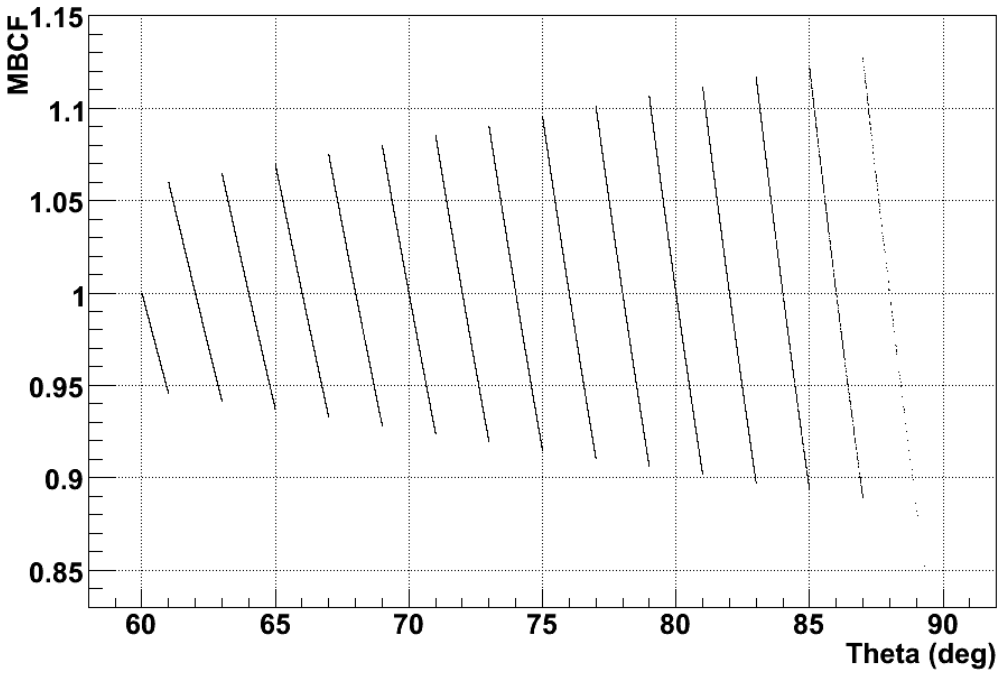

Figure 4.11: Correction factor.

As a corollary, the uncertainty in the determination of the zenith angle propagates to the estimated $N19$. The attenuation shown in fig. 4.10 can be used in a similar fashion to calculate the effect of this propagation of the angular uncertainty to the $N19$ and hence to the estimated energy.

4.5 Zenith angle dependence evaluation

As the development stage of an extensive air shower is a function of the atmospheric slant depth traveled before reaching ground, showers with the same energy but with

different zenith angle of incidence, will have different number of muons at ground and will show different shower sizes. Following analyses of more vertical showers we can refer to the reduction of the signals with zenith angle as attenuation. The attenuation curve is just a function that describes the dependence of this reduction on the zenith angle.

In our case the size parameter $N19$ is relative to a given map corresponding to the arrival direction of the reconstructed event. As the maps include an implicit attenuation, $N19$ only depends on energy assuming that maps have the correct attenuation. This assumption can be tested using the $\sin^2(\theta)$ distributions. Assuming an isotropical arrival of cosmic rays and 100% efficiency of the detector above a given energy threshold, the zenith angle distribution of events should proportional to $sin^2(\theta)$. Above a certain energy threshold, which is related to the saturation of the detector efficiency, this distribution should become flat. Equivalently a "Constant Intensity Cut" method [18–20] can be made by chosing the $N19$ value above which the event rate (or intensity) obtained in equal bins of $\sin^2(\theta)$ is constant. The resulting graph for $N19$ should be flat if the array is 100% efficient.

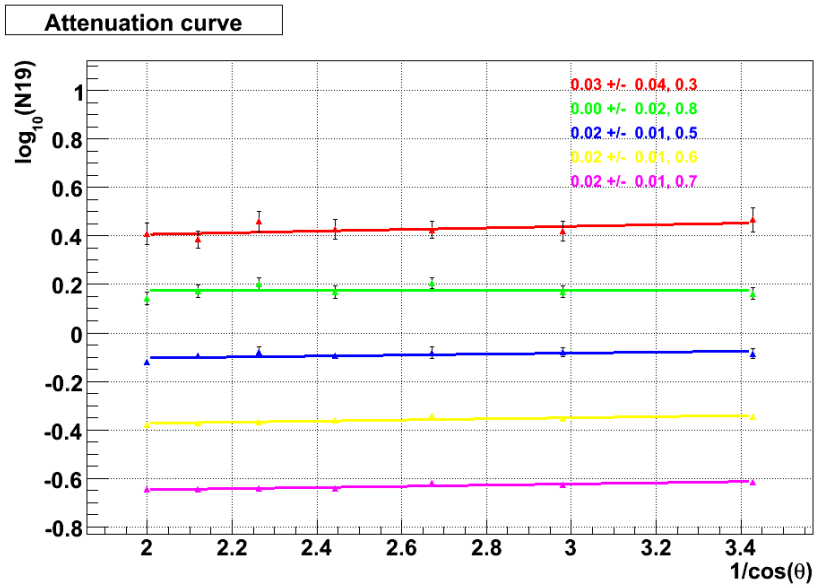

Figure 4.12: Solid lines are fits to a first order polynomial function. Legend shows the slopes of this fits, all of them compatible with a constant attenuation curve. Reduced χ^2 values for each fit are also shown.

The corresponding plot obtained for the five different intensities shown in the previous figure are practically flat what confirms that attenuation is adequately taken into account by the maps within the statistical accuravy of the method.

4.6 Energy calibration

As the shape of the muon maps is practically independent of energy, the size of the detected showers is measured with respect to a reference simulation corresponding to 10^{19} eV proton air showers. This size parameter, denoted as $N19$, gives the relative number of muons of the detected shower with respect to the reference for the same arrival direction. $N19$ will be shown to have a good correlation with the fluorescence energy measurement for a subset of hybrid events. This correlation allows us to use N19 as an estimator of the true energy of the cosmic ray.

4.6.1 Hybrid events selection for calibration curve

In order to assign an energy value to each N19 reconstructed value, we make use of the golden hybrid events reconstructed with both the FD and the SD to correlate the energy measured by the FD detector to the reconstructed $N19$ obtained with the SD in a similar way to what is done in vertical events [21]. From January 2004 to June 2008, 2665 $T4$ golden hybrid events have been detected with a zenith angle above 60°. A set of high quality golden hybrid events is chosen by imposing a collection of selection criteria. Quality criteria are applied to both the FD and the SD reconstructions.

1. FD cuts.

   (a) The events must have a Cherenkov fraction below 50% to avoid the uncertainties from the model of Cherenkov light.

   (b) The tank with largest signal must be closer than $750\ m$ to the shower axis.

   (c) The reduced χ^2 of the Gaisser-Hillas fit must be below 4 to get rid of events with profiles distorted due to clouds or fog. Profiles without a clear maximum are rejected by the requirement that the χ^2 of a linear fit to the profile exceeds the χ^2 of the Gaisser-Hillas fit by at least 4.

(d) A precise reconstruction of the shower profile, and hence a reliable estimate of its energy, requires the observation of a significant fraction of the profile and not only of its rising or falling section. For this reason, the shower maximum is required to be within the field of view and determined with an uncertainty below $50\ g/cm^2$.

(e) The uncertainty in the reconstructed energy must be below 40%. This is a useful parameter to reject badly reconstructed events because the reconstruction algorithm propagates uncertainties on the light flux and the geometrical uncertainties.

The magnitudes of these cuts are similar to those applied in the calibration with vertical showers [21]. Table 1 shows the number of events rejected by each cut and the number of remaining events after applying the cuts consecutively.

Cut label	a	b	c	d	e
Only	801	520	1189	1822	367
Remaining	1864	1440	759	439	439

Table 4.2: First line: FD cut label. Second line: number of events rejected by the each of the cuts applied on their own to the initial 2665. Third line: number of remaining events after applying cuts consecutively.

2. efit cuts.

(a) The relative uncertainty in $N19$ must be below 40%.

(b) The inclined T5 quality trigger condition must be satisfied to get rid of badly reconstructed events due to a misplacement of the shower core.

From the 439 events selected by the fluorescence cuts, 421 have a statistical uncertainty on $N19$ below 40% and 286 out of them fulfill the T5 trigger condition.

A good linear correlation between the size parameter $N19$ and the fluorescence energy E_{FD} is shown in fig. 4.13 for the 286 selected events. The energy of the event can be determined with the surface detector with this procedure that eliminates many of the

dependences on simulation or primary composition uncertainties from the shower size parameter by the linear relation:

$$\log(N19) = A + B\ \log(E) \tag{4.32}$$

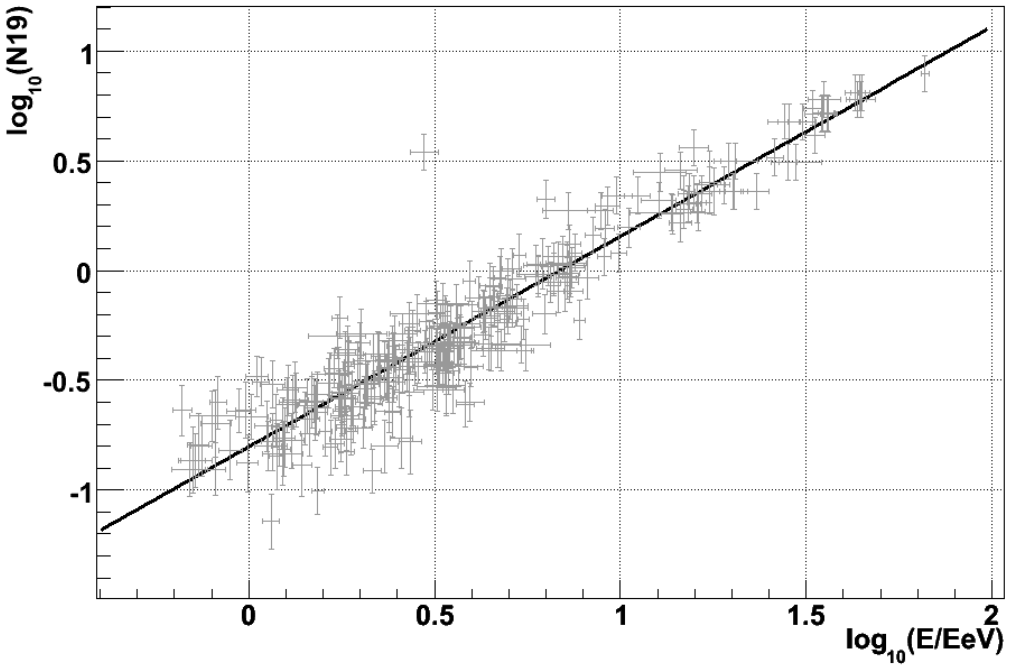

Figure 4.13: Linear correlation between $log_{10}(E)$ and $log_{10}(N19)$ for the 286 selected events.

Statistical uncertainties on $N19$ and on E_{FD} have been assigned to each event. On the one hand, for the statistical uncertainty of the SD reconstruction, σ_{N19}, three contributions have been taken into account:

$$\sigma^2_{N19} = (\sigma^{mle}_{N19})^2 + (\sigma^{\theta}_{N19})^2 + (\sigma^{sh}_{N19})^2 \tag{4.33}$$

where σ^{mle}_{N19}, is the statistical uncertainty obtained with the maximum likelihood method employed for the $N19$ reconstruction. σ^{θ}_{N19} accounts for the uncertainty on the zenith angle reconstruction which can be estimated using the correction factor described in

section 4.4 combined with the zenith angle uncertainty. Finally, σ^{sh}_{N19}, is due to the shower to shower fluctuations and it has been obtained using Monte Carlo simulations using proton primaries and QGSJETI to be 18%[4]. The average uncertainty for the complete set of selected events used in the calibration is 23%.

Fig. 4.14 shows the uncertainty in $N19$ extracted from the likelihood maximization procedure. This uncertainty increases with the zenith angle and decreases with energy. In the energy range where the energy spectrum of cosmic rays will be obtained is below 10%.

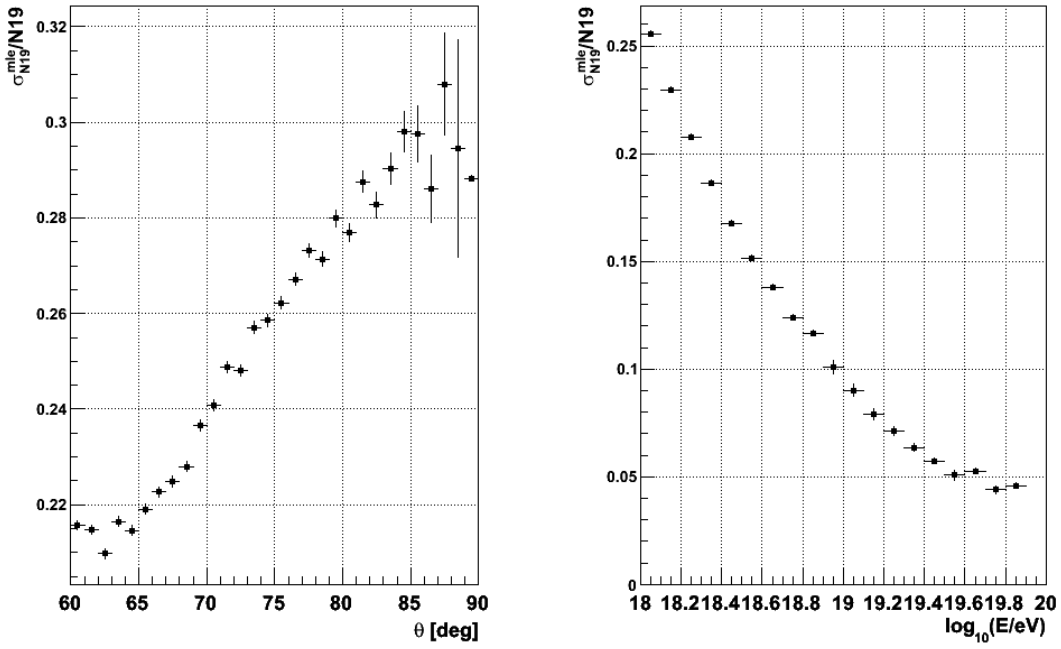

Figure 4.14: Uncertainty in $N19$ from the maximum likelihood procedure as a function of the zenith angle (left panel) and as a function of energy (right panel).

The statistical uncertainty due to the zenith angle uncertainty is estimated by the propagation of the uncertainty in θ into $N19$ that can be done directly from expressions 4.29, 4.30 and 4.31.

[4] R. Vázquez private communication.

$$\sigma^{\theta}_{N19} = \left|\frac{\partial N19}{\partial \theta}\right| \sigma_\theta \tag{4.34}$$

$$= \left|\frac{\partial N19}{\partial \kappa}\frac{\partial \kappa}{\partial \cos(\theta)}\frac{\partial \cos(\theta)}{\partial \theta}\right| \sigma_\theta \tag{4.35}$$

$$= N19\ \ln(10)\ |\sin(\theta)\ (b + 2c(1-\cos(\theta)))|\sigma_\theta \tag{4.36}$$

$$\frac{\sigma^{\theta}_{N19}}{N19} = \ln(10)\ |\sin(\theta)\ (b + 2c(1-\cos(\theta)))|\ \sigma_\theta \tag{4.37}$$

where σ_θ is the uncertainty in the zenith angle determination arising from the arrival direction reconstruction.

Fig. 4.15 shows the propagation of the zenith angle uncertainty into the shower size uncertainty following the previous expression.

The relative uncertainty in $N19$ due to the zenith angle uncertainty is in any case below 20%. In the angular range where the energy spectrum will be built (between 60° and 80°) the relative uncertainty is below 6%. Besides, as it is shown in the right panel of fig. 4.15, above $10^{18.7}\ eV$, the energy range in which the spectrum will be obtained, this uncertainty is below 3%.

On the other hand, the uncertainty assigned to E_{FD} is directly taken from the fluorescence analysis[5] and comes from several contributions such as the statistical uncertainty in the fit performed in the reconstruction procedure, the uncertainty of the hybrid geometry, the uncertainty of the correction for invisible energy, and the uncertainty in the aerosol content measurement. The mean value of this uncertainty is around 7% and it is practically constant in the whole hybrid sample for calibration.

In addition to the cuts performed on both the fluorescence and on the surface reconstruction to ensure the high quality of the reconstructed parameters, we have to get rid of the possible biases in the selected set of events. Inclined air showers trigger SD detector for energies above $10^{18.7}\ eV$ with close to 100% efficiency (see section 5.1). Below this energy, the surface detector is more sensitive to events with upward fluctuations on the number of muons, and these events should be rejected to avoid a bias in the calibration. Previous analyses for events with $\theta < 60^\circ$ have shown that discarding events below a line perpendicular to the calibration line may introduce a bias that can influence

[5] ADST

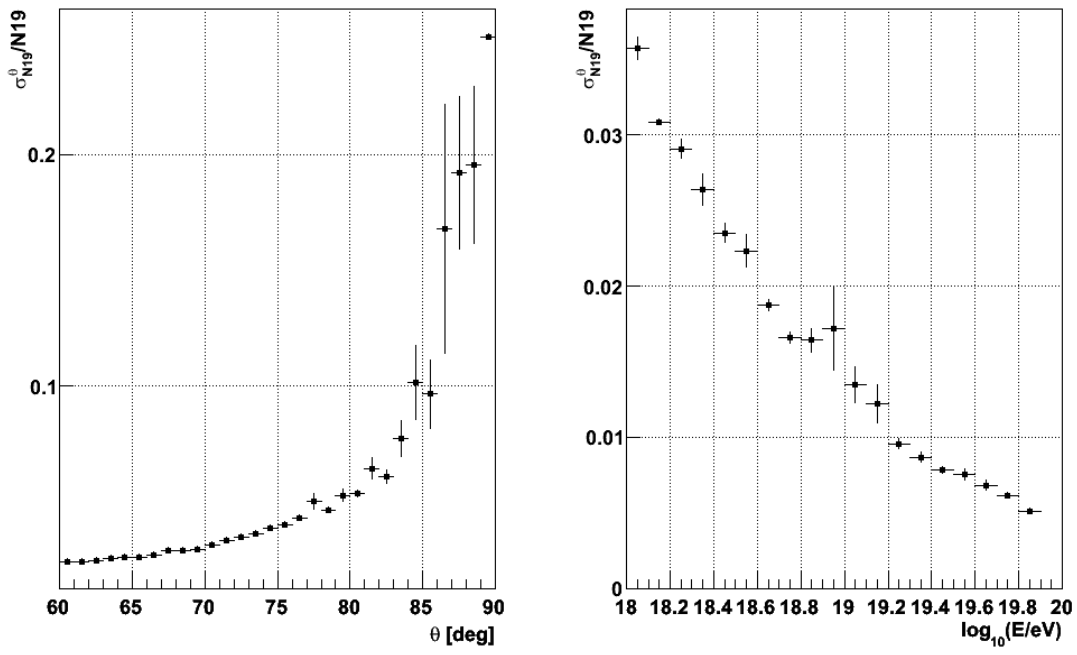

Figure 4.15: Propagation to the uncertainty in $N19$ of the uncertainty on the zenith angle. The uncertainty is shown as a function of the zenith angle (left panel) and as a function of energy (right panel).

the cosmic ray spectrum up to 20% especially in the low energy range [22]. This bias is due to the difference in the relative uncertainties on the fluorescence measurement of the energy and on the energy estimator from the surface detector measurement. Events are expected to be distributed within an "ellipse" error around the calibration line. This ellipse has two major axis according to the $\sigma_{E_{FD}}$ and σ_{N19}. If this ellipse error were just a circumference as in the left panel of fig. 4.16 a cut perpendicular to the calibration line would not introduce a bias as the two dashed areas in the figure would be equally populated. But if uncertainties are different, as it is actually true case (see right panel of fig. 4.16), one of the areas will be more populated and that population will bias the fit to obtain the calibration curve. A cut must be made depending on the relative uncertainties of both magnitudes that we try to correlate.

For a given pair $(E^{cut}_{FD}, N19^{cut})$ in the calibration line and assuming a Gaussian distribution of the measurements, data points are expected to be distributed according to

the ellipse error centered in $(E_{FD}^{cut}, N19^{cut})$ with $\sigma_{E_{FD}}$ and σ_{N19} for the x and y axis respectively. Rejecting low energy events under any line through $(E_{FD}^{cut}, N19^{cut})$ without taking into account the relative uncertainties on both magnitudes will introduce a bias in the determination of the calibration line. In this work, this low energy rejection is performed using an elliptical cut that takes into account the uncertainties in the energy measurement and in the N19 reconstruction with a certain confidence level as described in [23].

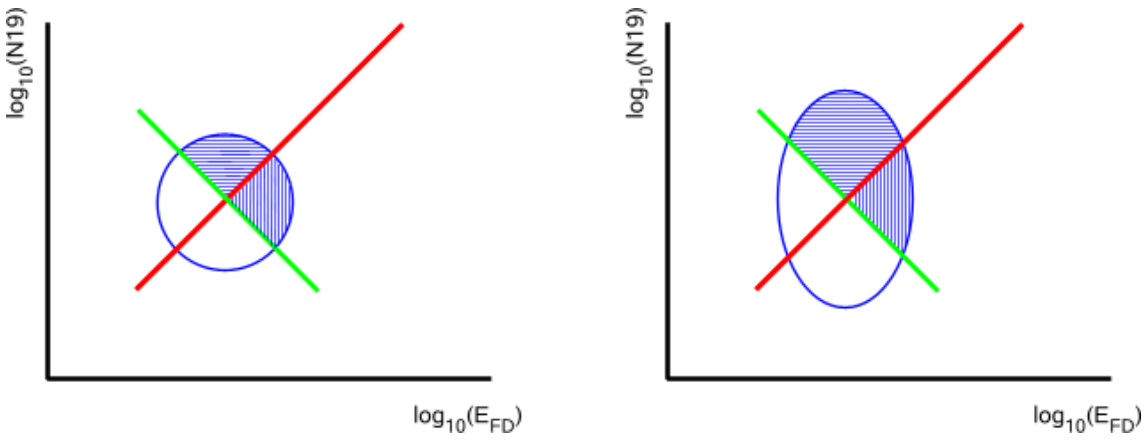

Figure 4.16: Elliptical cut.

This cut is implemented in two steps. Firstly, events below the energy at which the trigger efficiency saturates are all rejected. Secondly, events below this cut but within the ellipse error are retrieved to eliminate the bias introduced by that rejection. This recovery of events is very important for the establishment of the inclined events calibration line due to the low statistics of inclined golden hybrid events. The relative uncertainties on E_{FD} and $N19$ relative uncertainties are shown in fig. 4.17. The values used to fix the elliptical cut, based on a 95% confidence level for these uncertainties at the saturation energy are 0.07 for E_{FD} and 0.21 for $N19$.

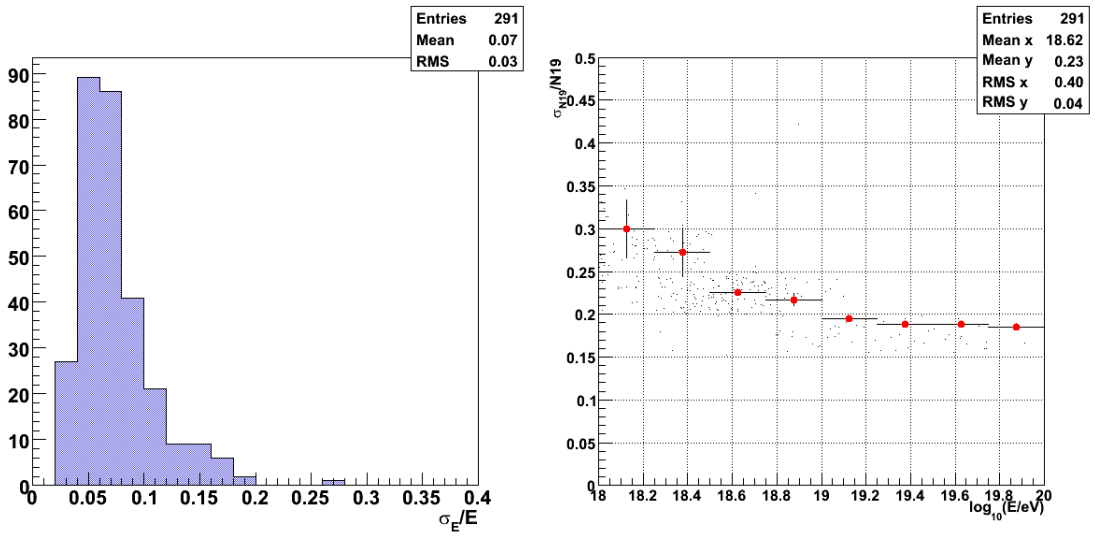

Figure 4.17: Relative uncertainties on E_{FD} and on $N19$ employed to fix the elliptical cut.

An alternative to this method is the so-called "optimal line cut" method described in [22] which uses a toy Monte Carlo to fix the slope of the line below which the events will be discarded. It does not introduce a bias on the measurement of the slope and the intercept of the calibration line, but the criterion employed in this work is, in principle, less sensitive to the true values of the uncertainties in E_{FD} and in $N19$ and does not depend on the real value of the slope as the optimal line cut does.

The 117 events that survive the elliptical cut are shown in light blue in fig. 4.18 with the linear best fit to them in dark blue. Parameters A and B from eq. 4.32 are $A = -0.82 \pm 0.03$ and $B = 0.99 \pm 0.03$ with a reduced χ^2 of 1.14.

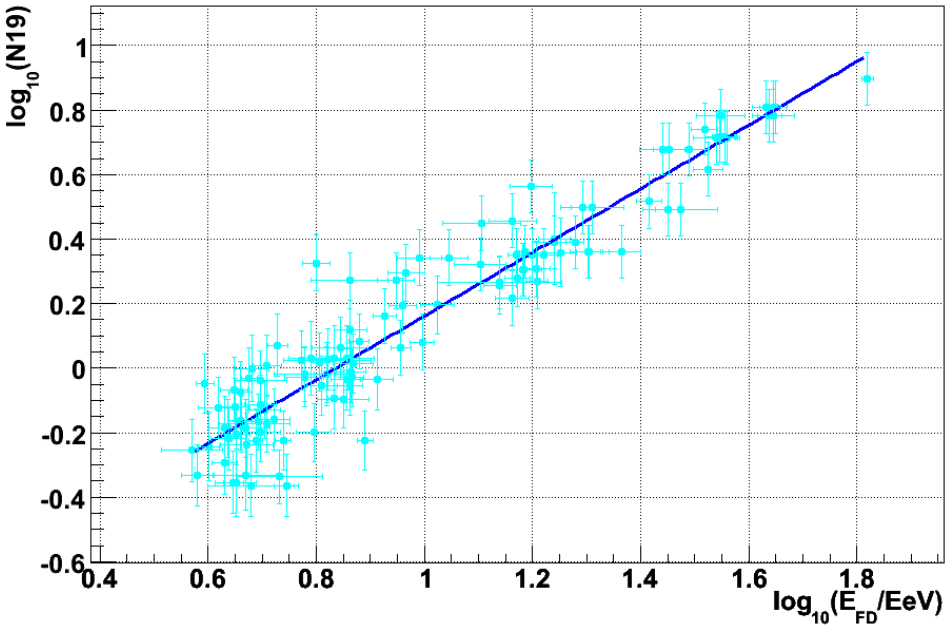

Figure 4.18: Correlation between $log_{10}(E)$ and $log_{10}(N19)$ for the selected 117 events used to get the calibration line.

The energy resolution can be estimated from the fractional difference between the fluorescence energy measurement and the energy derived from $N19$ with the calibration curve. This resolution is taken as 20% from the standard deviation shown in fig.4.19.

4.6.2 Additional cross checks

To confirm, in a simple way, that the uncertainties assigned to the fluorescence measured energy and to the N19 reconstructed parameter have been correctly estimated, an orthogonal pull distribution has been built as:

$$P = \frac{\log_{10} N19 - (A + B \log_{10} E_{FD})}{\sqrt{\sigma^2_{\log_{10} N19} + B^2 \ \sigma^2_{\log_{10} E_{FD}}}} \tag{4.38}$$

The pull distribution is shown in fig. 4.20. The mean is close to zero and the standard deviation of the Gaussian fit is close to unity as it is expected from a proper estimation of uncertainties.

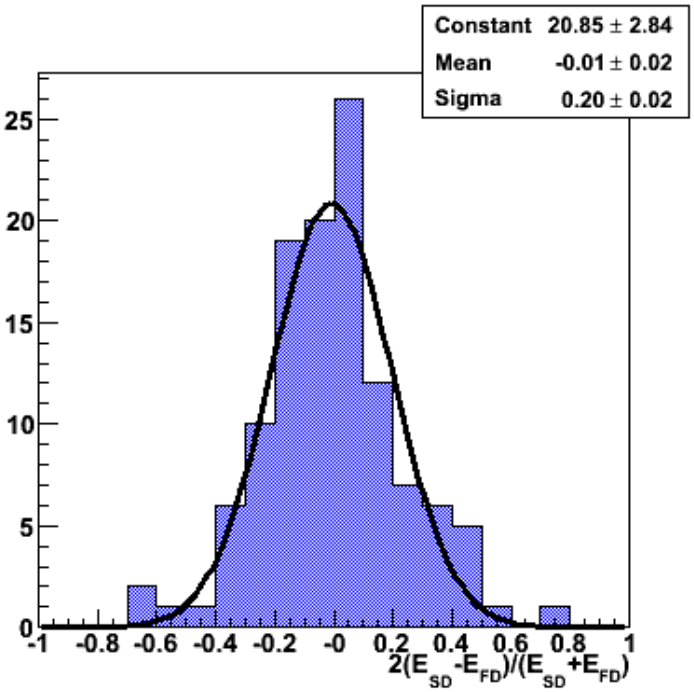

Figure 4.19: E_{SD} energy resolution.

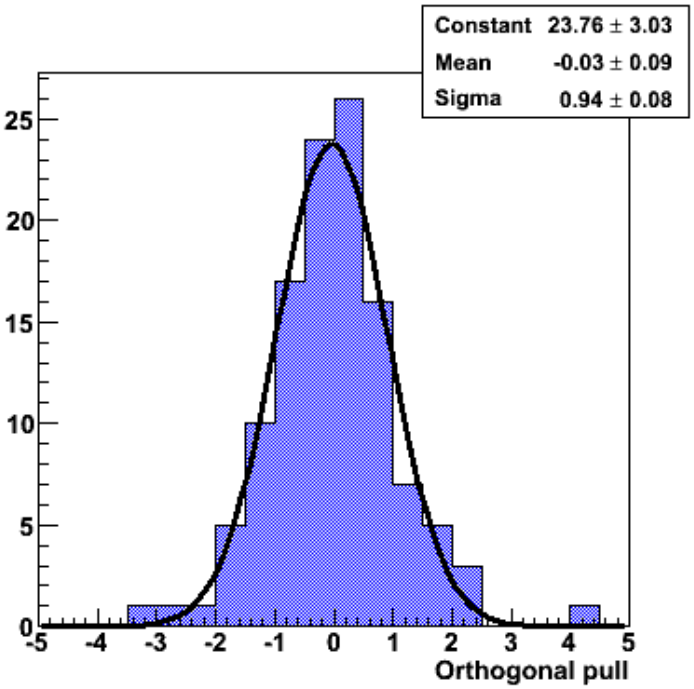

Figure 4.20: Orthogonal pull for the selected hybrid events.

As a further check, the calibration procedure has been performed for three eyes separately. "Loma Amarilla" has not been used because it has not enough statistics (only 9 events). Results are shown in fig. 4.21 and given in table 4.6.2 showing a good agreement within the statistical fluctuations. Thus, no systematic on the calibration curve is introduced when using events detected with different eyes of the fluorescence detector.

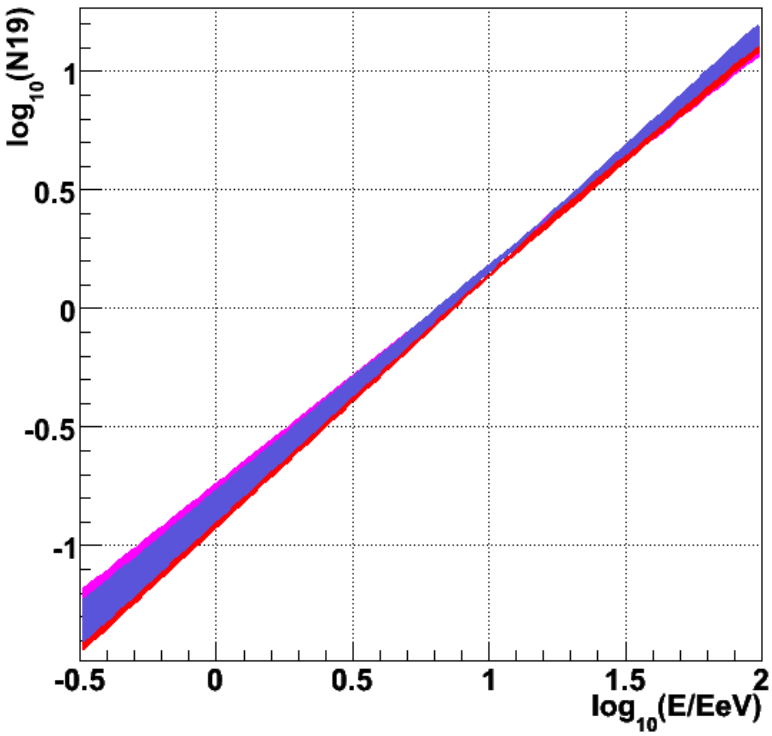

Figure 4.21: Calibration curves by FD eye. Leones (red), Coihueco (blue) and Morados (pink) calibration curves show a good agreement between them within the statistical uncertainties that are represented by shaded areas around the mean values of the calibration.

Eye	a	σ_a	b	σ_b	N
Leones	-0.87	0.05	1.01	0.05	39
Coihueco	-0.83	0.06	1.00	0.05	35
Los Morados	-0.79	0.05	0.96	0.05	34

Table 4.3: Calibration parameters by eye.

To study a possible bias introduced by the low energy event rejection, the calibration procedure has been performed for five different low energy thresholds for rejection: $10^{18.7}\ eV$, $10^{18.9}\ eV$, $10^{19.1}\ eV$, $10^{19.3}\ eV$ and $10^{19.5}\ eV$. As it is shown in fig. 4.22 all of them are compatible within the uncertainties. The resulting parameters as well as the number of events in the fits are shown in table 4.6.2.

$log_{10}(E_{FD}^{cut}/eV)$	a	σ_a	b	σ_b	N
18.7	-0.82	0.03	0.98	0.03	115
18.9	-0.78	0.04	0.95	0.04	80
19.1	-0.75	0.08	0.93	0.06	49
19.3	-0.87	0.11	1.01	0.08	39
19.5	-0.81	0.31	0.98	0.20	19

Table 4.4: Calibration parameters for different low energy cuts.

No systematic is seen due to the fluorescence eye or to the low energy cut selection. All the values of the parameters of the calibration curve are compatible between them within the uncertainties.

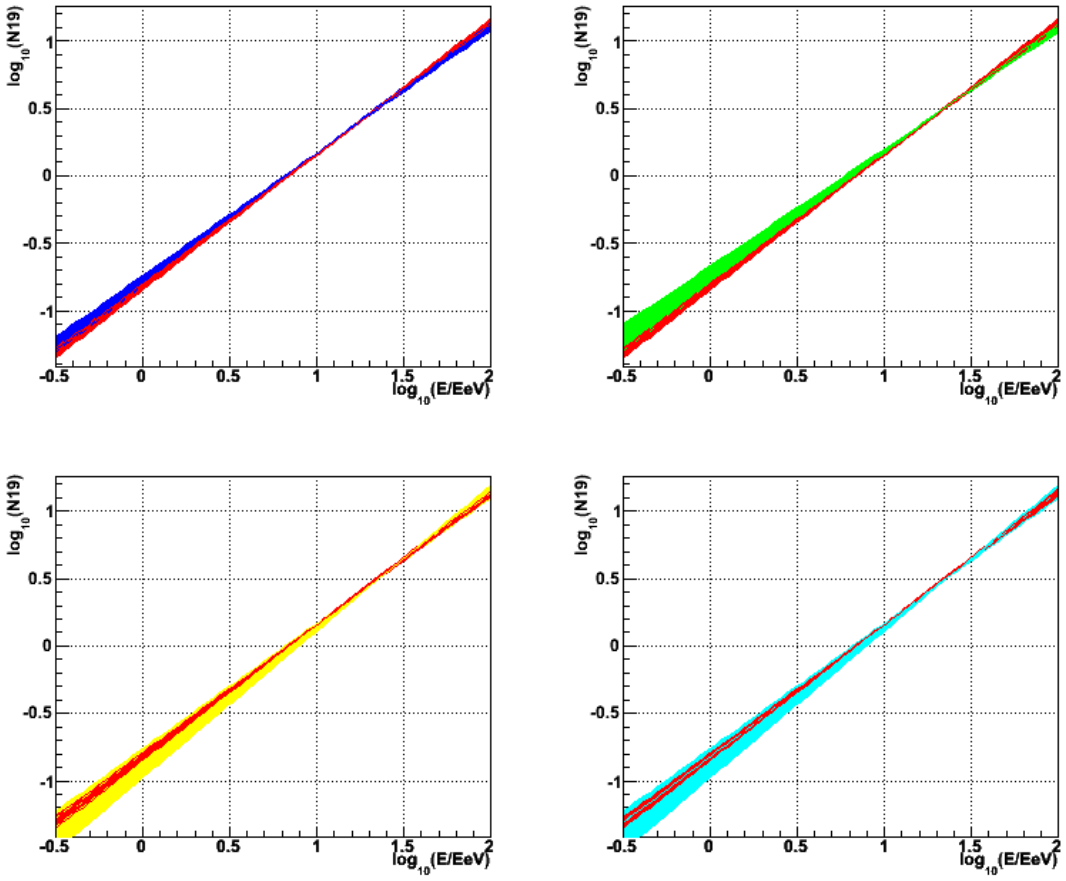

Figure 4.22: Calibration curves for different low energy cuts. The reference one with the cut at $10^{18.7}\ eV$ (red) is compared with the others. Top left $E_{cut} = 10^{18.9}\ eV$ (dark blue), top right $E_{cut} = 10^{19.1}\ eV$ (green), bottom left $E_{cut} = 10^{19.3}\ eV$ (yellow) and bottom right $E_{cut} = 10^{19.5}\ eV$ (light blue). The calibration curves show a good agreement between them within the statistical uncertainties which are represented by shaded areas around the mean values of the calibration.

Bibliography

[1] M. Ave, R. A. Vázquez & E. Zas, Astropart. Phys. **14** (2000) 91.

[2] M. Ave, R. A. Vázquez, E. Zas, J. A. Hinton & A. A. Watson, Astropart. Phys. **14** (2000) 109.

[3] M. Ave, J. A. Hinton, R. A. Vázquez & E. Zas, Phys. Rev. D **65** (2002) 063007.

[4] M. Ave, J. A. Hinton, R. A. Vázquez, A. A. Watson & E. Zas, Phys. Rev. D **67** (2003) 043005.

[5] M. Ave *et al.*, Nucl. Instrum. Meth. A **578** (2007) 180.

[6] R. A. Fisher, Philos. Trans. Roy. Soc. London Ser. A **222**, (1922) 309.

[7] M. Aglietta, I. De Mitri, S. Maglio, S. Maldera, I. C. Maris, D. Martello, G. Navarra & M. Roth, "Recovery of saturated signals of the surface detector", Pierre Auger Collaboration Internal Document, GAP Note 2008-030.

[8] D. Veberic & M. Roth, "SD Reconstruction Offline Reference Manual", Pierre Auger Collaboration Internal Document, GAP Note 2005-035.

[9] P. Billoir, O. Deligny & A. Letessier-Selvon, "A complete prcedure for the reconstruction of inclined air showers", Pierre Auger Collaboration Internal Document, GAP Note 2003-003.

[10] H. Dembinski, T. Hebbeker & M. Leuthold, "A comparison of Monte-Carlo generated Muon Maps with near horizontal SD showers", Pierre Auger Collaboration Internal Document, GAP Note 2007-124.

[11] G. Rodríguez-Fernández PhD Thesis. "Horizontal air showers at the Pierre Auger Observatory," (2007).

[12] L. Cazón, R. A. Vázquez, A. A. Watson & E. Zas, Astropart. Phys **21** (2004) 71.

[13] S. J. Sciutto Proc. 26th International Cosmic Ray Conference, Salt Lake City-USA, (1999).

S. J. Sciutto astro-ph 9911331.

[14] D. Heck *et al.*, "The CORSIKA Air Shower Simulation Program", Report FZKA 6019 (1998).

[15] http://geant4.web.cern.ch/geant4

[16] I. Valiño PhD Thesis. "Detection of horizontal air showers and neutrino induced showers with the Pierre Auger Observatory", Pierre Auger Collaboration Internal Document, GAP Note 2008-024.

[17] C. Pryke, "Asymmetry of Air Showers at Ground Level", Pierre Auger Collaboration Internal Document, GAP Note 1998-034.

X. Bertou & Pierre Billoir, "On the origin of the asymmetry of ground densities in inclined showers", Pierre Auger Collaboration Internal Document, GAP Note 2000-017.

M. T. Dova, "Asymmetries Observed in Giant Air Showers Using Water Cherenkov Detectors", Proc. 28th International Cosmic Ray Conference, Tsukuba-Japan, **8** (2003) 34.

[18] D. M. Edge *et al.*, J. Phys. A **6** (1973) 1612.

[19] J. Alvarez-Muñiz *et al.*, Phys. Rev. D, **66** (2002) 123004.

[20] M. Ave *et al.*, Astropart. Phys. **19** (2003) 47.

[21] Vertical calibration

[22] I. C. Maris PhD Thesis, "Measurement of the Ultra High Energy Cosmic Ray Flux using Data of the Pierre Auger Observatory", Pierre Auger Collaboration Internal Document, GAP Note 2008-026.

[23] C. di Giulio *et al.*, "Study of systematic uncertainties on the S_{38} energy calibration"

Chapter 5

Energy spectrum of UHECR

In this section, the energy spectrum of Ultra High Energy Cosmic Rays is derived using the surface detector data with a reconstructed zenith angle between 60° and 80°. The energy spectrum of the cosmic rays is the differential flux of cosmic rays at a certain energy E: $J(E)$. It can be obtained dividing the number of cosmic ray events detected, $N(E)$, in an energy interval ΔE by the exposure of the detector at that energy, $\eta(E)$.

$$J(E)\Delta E = \frac{N(E)}{\eta(E)} \tag{5.1}$$

As the $T5$ trigger condition discussed in section 2.3.2 is applied to the data to guarantee a high quality of the reconstruction parameters, the total detection area of the surface detector is constrained. This constraint allows us to calculate the active detection area as a multiple of the area of an elementary array cell, a_{cell}. Above a given energy threshold, that will be chosen to select events triggering the surface detector independently of their incoming direction or of their energy, the aperture of this elementary area, $\mathcal{A}_{cell}$, becomes purely geometrical. Thus, counting the number of active cells, N_{cell}, in a given period, Δt, we can obtain the exposure of the whole detector as $\eta = N_{cell}\ \mathcal{A}_{cell}\ \Delta t$.

5.1 Saturation energy of the trigger efficiency

The trigger efficiency, defined as the probability that an extensive air shower induces a given trigger level, depends on some parameters of the shower such as energy and

zenith angle. Over a given energy threshold called *saturation energy*, E_{sat},the efficiency is 100%, the calculation of the aperture will be purely geometrical and the exposure becomes independent of the energy. To deduce the cosmic ray flux from the measured data, the knowledge of this threshold is relevant because no points can be obtained below it unless some correction for the reduced efficiency is applied.

The trigger efficiency of the surface detector can be measured from a sample of hybrid events provided that the saturation energy of the trigger of the fluorescence detector is lower than that of the surface detector and that both trigger probabilities are uncorrelated. Binning all the hybrid events in energy intervals and counting in each bin the number of hybrid events that have also triggered the surface detector, n, the efficiency of the surface detector trigger is given by the ratio n/N [1] where N is the total amount of hybrid events in the sample.

In order that not to lose events because of other causes, besides the trigger efficiency, we have to ensure that the surface detector is active and ready to detect the event at the time the FD event takes place. We will only consider an FD event if the surface detector is not on a "bad period" of data acquisition. In addition, we ask the station with the largest signal, that it is supposed to be triggered by the FD detected shower, to be closer than $900\ m$ to the shower axis and to have active the first hexagon of neighbor stations.

The result of this method is shown in fig. 5.1 showing an energy saturation of the trigger efficiency between $10^{18.5}\ eV$ and $10^{18.8}\ eV$. We will use $10^{18.7}\ eV$ as a conservative estimate. The uncertainty in the trigger efficiency is expected to be well below 5% above this energy. This is an experimental approach to obtain the efficiency. A second possibility can be obtained with the infill array but it is presently being tested and the statistics available is still insufficient.

There are two caveats to this hybrid approach. There are very few hybrid events of zenith angle above 74° because of geometrical reasons. If shower maximum is to be observed with the FD, very inclined events will impact the ground outside the array area. In addition, for the same reason, at lower angles, the FD detector can have a selection effect by demanding the shower maximum to be in the field of view. Deeper showers are more likely to trigger both the FD and SD detectors. These deep showers are likely to have higher muon densities at ground level thus they can induce an overestimate of the efficiency. For this reason, this work will be updated by full Monte Carlo simulations. First

simulations using muon density maps and neglecting the electromagnetic component to give conservative results have given results which are slightly below those given by this hybrid approach.

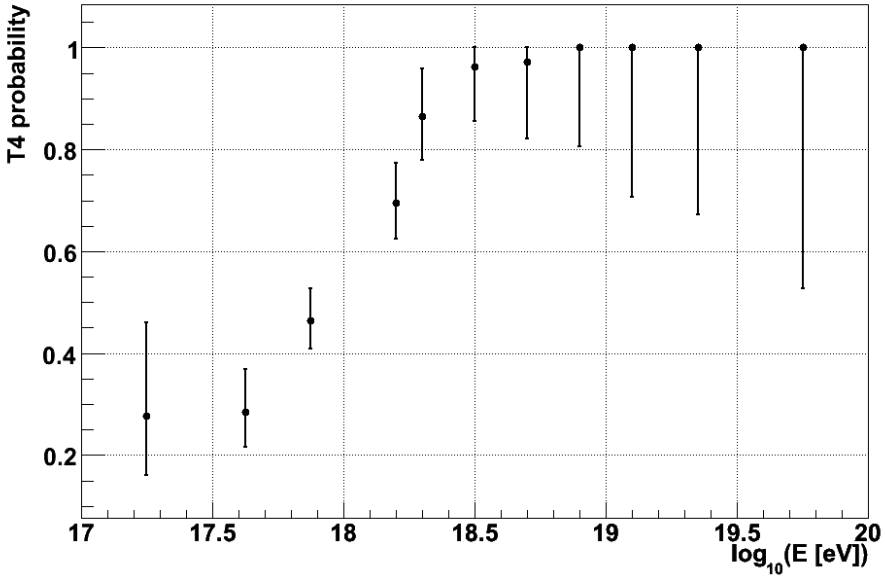

Figure 5.1: Efficiency curve for T4 triggers using hybrid events. Saturation is achieved at an energy of $10^{18.5}\ eV < E < 10^{18.8}\ eV$. Error bars correspond to the 68% confidence level.

5.2 Aperture and exposure

The exposure of the surface detector is given by the time integration of the aperture $\mathcal{A}$:

$$\eta(E) \ = \ \int_{t_i}^{t_f} dt\mathcal{A} = \ \int_{t_i}^{t_f} dt \int d\Omega \ A(t) \ cos(\theta) \ \epsilon_{SD}(E,\theta) \tag{5.2}$$

where t_i and t_f are the limits of the time interval of the observation, Ω is the solid angle, $A(t)$ is the effective area of the detector which varies with time[1], $\epsilon_{SD}(E,\theta)$ is the trigger efficiency of the surface detector, E is the energy and θ is the zenith angle.

[1]growing detector, up and down periods, etc.

Above the E_{sat}, $\epsilon_{SD}(E,\theta) = 1$ and hence

$$\eta(E) \;=\; \int_{t_i}^{t_f} dt \int d\Omega \; A(t) \; cos(\theta) \tag{5.3}$$

At a given time, the instantaneous aperture over the energy saturation of the array is a multiple of the elementary aperture of the unit cell shown in grey in fig. 5.2 corresponding to a detection area of $a_{cell} = 1.95 \; km^2$ which provides an aperture of $\mathcal{A} \approx 1.33 \; km^2 \; sr$ upon solid angle integration for events incoming with a zenith angle between 60° and 80°.

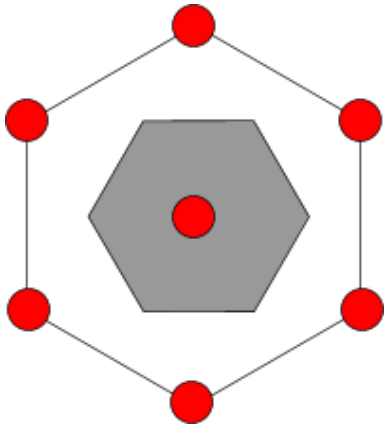

Figure 5.2: Schematic view of a unit cell of the surface detector array. Shaded region corresponds to the detection area accounted for if the first hexagon around the central tank is active.

The time integral necessary for the exposure calculation can be transformed into a sum over the instantaneous aperture of the array. Using the T2 files that monitor the changes in the array configuration with a time resolution of $1 \; s$, we can compute the number of active unitary cells in each second. The exposure will be:

$$\eta[km^2 \; sr \; s] \; = \mathcal{A}_{cell} \sum_{t_i}^{t_f} N_{cell} \; \Delta t \tag{5.4}$$

where $\mathcal{A}_{cell}$ is $1.33 \; km^2 \; sr$, t_i and t_f are the initial and final limits of the time interval we want to compute the exposure for, N_{cell} is the number of active cells in each second and Δt is $1 \; s$ as this is the time period that each array configuration is stored in the T2

files.

These T2 files are not enough to compute the effective area of the detector in each second as they provide only with information about single stations trigger rates but not on the performance of the *central trigger* (CT) and of the *central data acquisition system* (CDAS). Even if the local stations are sending data to the CDAS, the acquisition system can be stopped or not be taking and storing data properly. In these cases, only using the T2 files will overestimate the exposure. The up time of the whole detector must be taken into account to compute the effective area and to select events detected during uptime periods of the surface detector to avoid such problems. The estimate of this uptime is made on a T5 rate basis as described in [3] assuming that the T5 events follow a Poisson distribution and that the T5 daily rate per hexagon is constant. Periods having too large intervals between two consecutive T5 evens will be rejected. The choice of the time interval is done on a probability basis. This work is the responsibility of the Acceptance task[2] and we use here their results.

In table 5.2 the total exposure of the surface detector for each year of the data used in this to obtain the cosmic ray flux are given.

Year	Hexagon s $[s]$	Exposure $[km^{-2}\ sr^{-1}\ y^{-1}]$
2004	3776647205	159.28
2005	11437023959	482.35
2006	16954023241	715.02
2007	24890134062	1049.72
2008	6405449060	270.14

Table 5.1: Number of active hexagon-second (first column) and exposure (second column) per each year of data.

5.3 UHECR energy spectrum

With a total exposure from January 2004 to June 2008 of the surface detector of the Pierre Auger observatory between 60° and 80° of $\sim 2700\ km^2\ y\ sr$, the energy spectrum

[2] ipnweb.in2p3.fr/ auger/AugerProtected/AcceptWork.html

of the UHECR is shown in fig. 5.3. The number of selected events in each energy bin is also shown.

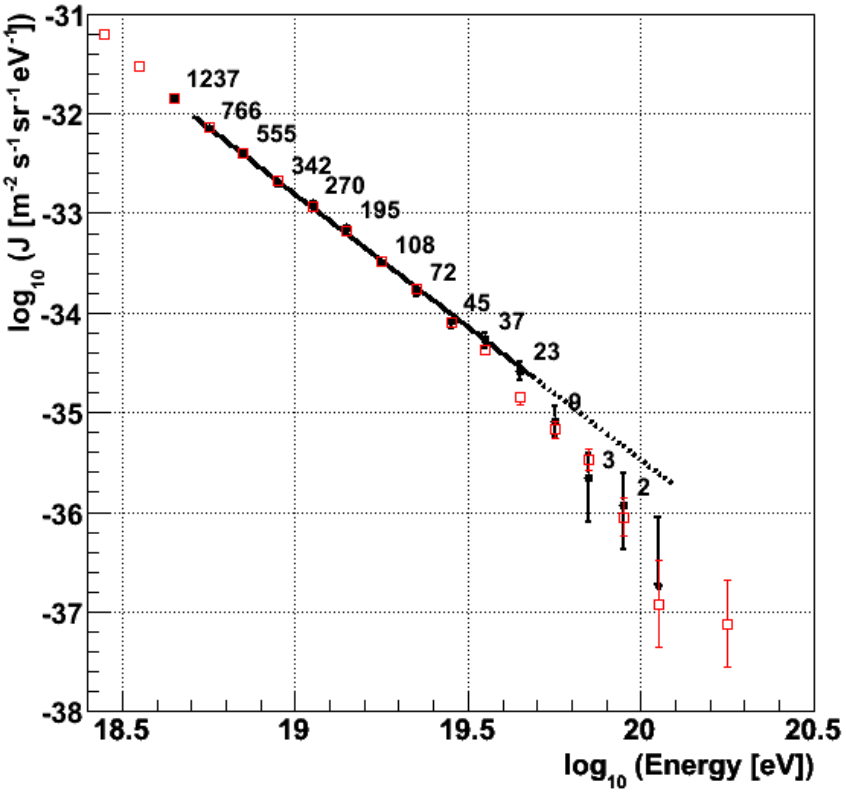

Figure 5.3: Differential cosmic ray flux as a function of energy. Error bars correspond only to statistical uncertainties. Filled black squares are the result of this work whereas empty red squares are the energy spectrum obtained using the vertical events and reconstruction methods. Number of events in each energy bin for this work is also given.

Error bars correspond only to statistical uncertainties of the 68% confidence level intervals calculated according to [4]. Upper limits in energy bins without detected events, are computed with the 95% confidence level intervals calculated according to [4]. In addition to these uncertainties there are systematic uncertainties due to the fluorescence energy reconstruction, 22%, as well as systematic uncertainties do to the calibration procedure. Both of these affect the energy scale and need to be considered.

A fit to a power law function between $E = 10^{18.7} eV$ and $E = 10^{19.7} V$ has been performed obtaining a spectral index of $\gamma = 2.70 \pm 0.05$. The expected number of events above $E > 10^{19.7}\ eV$ computed by an extrapolation of this power law fit is 53 ± 2 whereas only 14 events are observed.

The spectrum obtained with this analysis of inclined events is also compared with the one obtained with events of zenith below $60°$ of the Pierre Auger Observatory published in [5] showing a very good agreement.

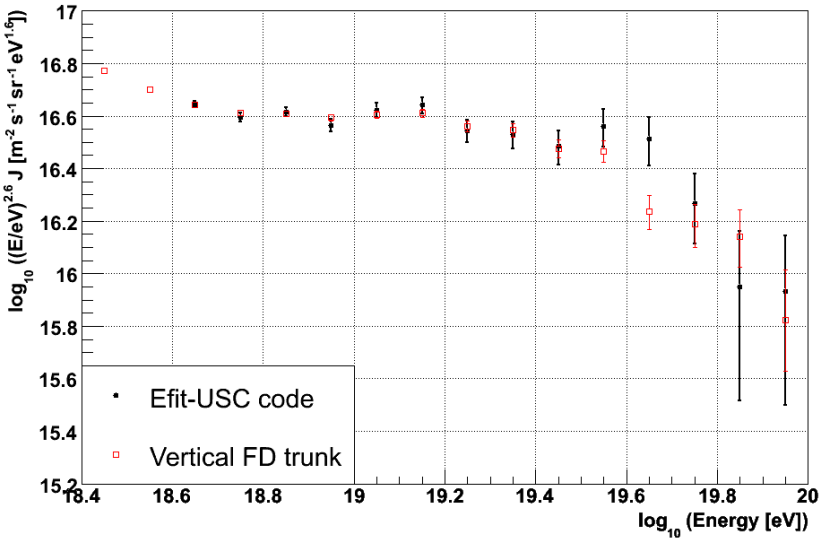

Figure 5.4: Energy spectrum multiplied by E^3. Error bars correspond only to statistical uncertainties. Filled black squares are the result of this work whereas empty red squares are the energy spectrum obtained using the vertical events and reconstruction methods.

5.4 Flux uncertainties

The flux uncertainty has contributions from the uncertainties in the normalization of the flux i.e. the acceptance and from the energy scale uncertainties. The uncertainties in the energy scale result from the calibration and from the determination of the size parameter $N19$.

Uncertainties in the normalization

The uncertainty in the acceptance has several contributions mainly from the trigger efficiency dependence, the detector response, the non regularity of the array or the rejection of unstable periods. All these contributions have a global effect that has be quantified below $\sim 1\%$ in the analysis of events below 60° [6] being the contribution of the non regularity of the array $\sim 0.05\%$ and that due to the rejection of bad periods of data taking $\sim 0.5\%$. We shall use this value in our results.

Besides, the reconstruction program fails to reconstruct less than 0.5% of the $T4$ events. These problems may be due to inefficiencies of the selection or reconstruction algorithms. In this work a 1% systematic uncertainty will be considered conservatively to account for this efficiency loss.

Uncertainties in energy

The uncertainty in the energy derived from the surface detector measurement E_{SD}, has two contributions. The first one arises from the calibration fit and the second one from the uncertainty in $N19$. Besides the uncertainties in $N19$ due to the maximum likelihood method, to the propagation of the uncertainty in the zenith angle reconstruction and to the shower to shower fluctuations that have been accounted for in the calibration procedure on an event by event basis, other sources of uncertainties have been identified. Those include the muon maps or the electromagnetic signal parameterization.

Calibration uncertainty

The uncertainty due to the calibration is obtained propagating uncertainties directly in eq. 4.32:

$$\frac{\sigma_E(cal)}{E} = \ln(10)\ \sqrt{\sigma_A^2 + \sigma_B^2 \log^2(N19) + 2\rho\sigma_A\sigma_B \log(N19)} \tag{5.5}$$

where σ_A and σ_B are the uncertainties in the fitted parameters and ρ is the correlation coefficient of the fit. As it is shown in fig. 5.5 this uncertainty amounts to less than 4% at $10^{20}\ eV$.

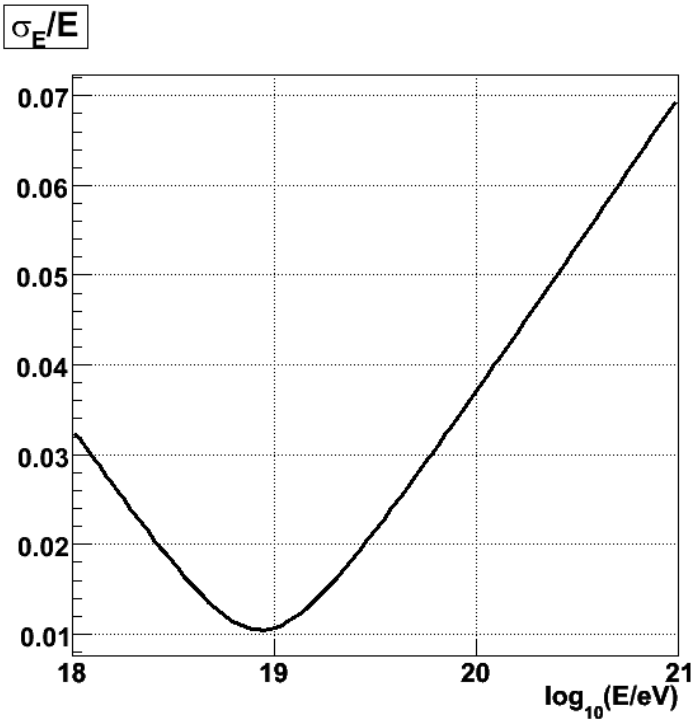

Figure 5.5: Relative uncertainty due to the calibration process.

Uncertainty due to muon maps

To evaluate the systematic uncertainty due to muon maps we have reconstructed the same set of events with the same reconstruction program but using a different set of muon maps. Comparing the $N19$ value obtained using the USC muon maps [7] with the value obtained using the Aachen muon maps [8], an uncertainty on $N19$ below 10% as shown in fig. 5.6 can be quoted.

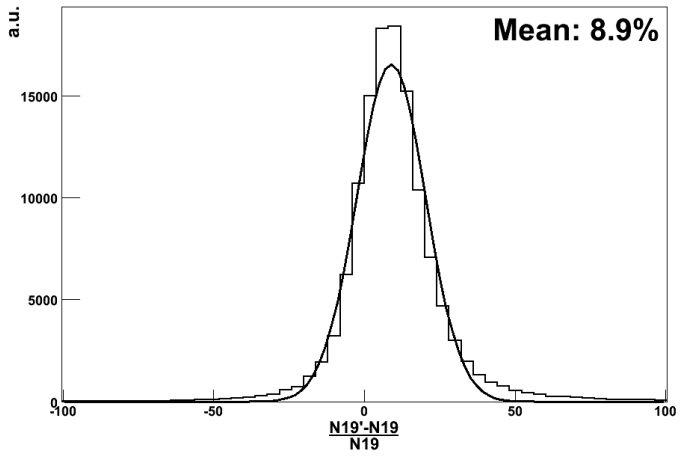

Figure 5.6: N19 uncertainty due to muon maps.

Most of this systematic uncertainty is practically reabsorbed during the calibration procedure as it is shown in fig. 5.7 where the $N19$ have been converted to energy using for each set their corresponding calibration curve. A systematic uncertainty below 0.5% is observed in the reconstructed energy although the distribution shows non-gaussian tails that should be studied with more detail. The energy spectrum should be insensitive to the choice of muon map after the calibration with hybrid events as it was already mentioned in [8]. However, the fact that the shower size is about 10% greater when measured with respect to one set of maps than when measured with respect to another, may be important to draw any conclusions about the number of muons in data compared to those predicted by simulations.

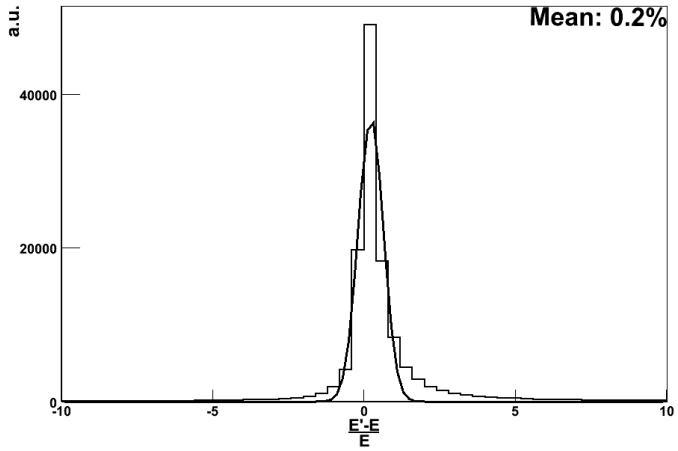

Figure 5.7: Systematic uncertainty in energy due to muon maps.

Uncertainty due to the electromagnetic correction of the signal

Proceeding in a similar way to evaluate the uncertainty introduced by the parameterization of the electromagnetic signal, we reconstruct a sample of events increasing or decreasing the electromagnetic contribution within the uncertainty of the parameterization quoted to be 10% in the parameterization of the Monte Carlo simulations that have been used [] The resulting uncertainty is below 5% in $N19$ as shown in fig. 5.8. This uncertainty should be pretty reabsorbed through a calibration procedure and it is thus expected to be small. Some additional studies are needed to evaluate effects of composition, model assumptions and energy.

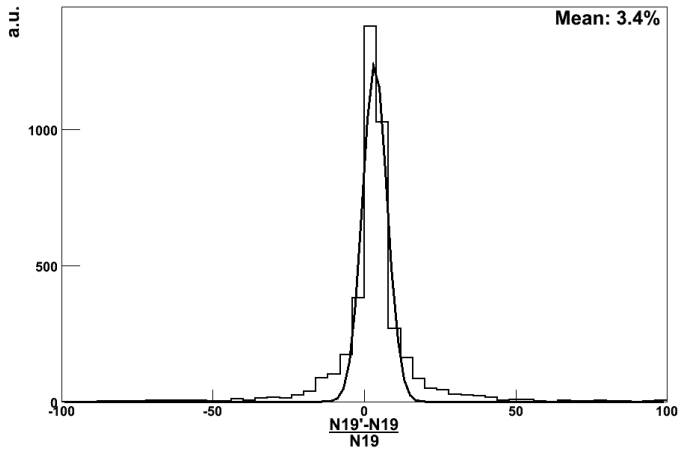

Figure 5.8: Systematic uncertainty in N19 due to the parameterization of the electromagnetic signal.

Table 5.4 summarizes the systematic uncertainties in the energy spectrum derived with inclined events from the surface detector.

Source	Uncertainty
Saturation of trigger efficiency	2%
Acceptance	1%
Reconstruction algorithms	1%
N19 uncertainty	$< 14\%$
Calibration	$< 5\%$
Maps	1%
Electromagnetic correction	5%
TOTAL	$< 16\%$

Table 5.2: Systematic uncertainties in the cosmic ray flux.

Some of these uncertainties are energy dependent so they do not affect the energy spectrum as a global factor but they have to be properly propagated to it.

Bibliography

[1] N. G. Busca PhD. Thesis, "The ultra high energy cosmic ray flux from the southern Pierre Auger observatory data", Pierre Auger Collaboration Internal Document, GAP Note 2006-108.

[2] I. C. Maris PhD. Thesis, "Measurement of the Ultra High Energy Cosmic Ray Flux using Data of the Pierre Auger Observatory", Pierre Auger Collaboration Internal Document, GAP Note 2008-026.

[3] C. Bonifazi & A. Letessier-Selvon, "Event selection using the T5 time distribution", Pierre Auger Collaboration Internal Document, GAP Note 2006-042.

C. Bonifazi & P. Ghia, "Selection of data periods and calculation of the SD geometrical acceptance", Pierre Auger Collaboration Internal Document, GAP Note 2006-101.

[4] G. J. Feldman & R. D. Cousins, Phys. Rev. D **57** (1997) 3873.

[5] J.Abraham *et al.*, Phys. Rev. Lett. **101** (2008) 061101.

[6] C. Bonifazi & P. Ghia, "Selection of data periods and calculation of the SD geometrical acceptance", Pierre Auger Collaboration Internal Document, GAP Note 2006-101.

D. Allard, "Determination of the aperture of the PAO surface detector", Proc. 29th International Cosmic Ray Conference, Pune-India,**7** (2005) 71.

[7] M. Ave, R. A. Vázquez & E. Zas, Astropart. Phys. **14** (2000) 91.

[8] H. Dembinski, T. Hebbeker & M. Leuthold, "A comparison of Monte-Carlo generated Muon Maps with near horizontal SD showers", Pierre Auger Collaboration Internal Document, GAP Note 2007-124.

Chapter 6

Conclusions

In this work, the complete reconstruction chain of events of the surface detector of the Pierre Auger Observatory with a zenith angle over 60° has been completely described and the the cosmic ray flux measured using those events has been presented. The high statistics of the surface detector allows a good estimate of the energy spectrum of UHECRs above $10^{18.7}\ eV$. It has been obtained using data collected from 1st January 2004 to 31st August 2008 accounting for an exposure of $\sim 2700\ km^2 sry$.

Regarding the reconstruction of the incoming direction of the cosmic ray, the time model for the distribution of the arrival time of muons in the shower front has been validated. This model predicts the distributions of the time delay of the particles in the shower front with respect to a plane moving at the speed of light in time with the primary cosmic ray. The mean time delay can be associated to the front curvature and the variance in the arrival time of the first particle can be also predicted.

The time variance predicted by the model has been compared to data making use of doublets. These are made of two tanks placed at practically the same location. The difference in the residuals of the time fit of the two stations has been compared to the predictions obtained from the model. The performance of the time variance has been shown to be in a very good agreement with data. The variance has been shown to agree with data up to a distance of $\sim 4000\ m$ to the shower core from and up to signals as large as $\sim 50\ VEM$ without any cuts. The agreement with data is much better than that presented by the model of time variance employed for the analysis of vertical events.

In the procedure to reconstruct the shower core position and the shower size, the shower size is estimated as the relative number of muons with respect to a reference

10^{19} eV proton shower. This parameter, called $N19$, has been shown to have a great correlation with the calorimetric measurement of the energy by the fluorescence detector in an analogous way to the calibration procedure for events below $60°$, playing $N19$ a role similar to S_{38}. $N19$ is used as an estimator of the energy and it is calibrated using hybrid events.

The energy of an event collected by the surface detector needs several assumptions about high energy interactions and about the cosmic ray primary. In this work $N19$ has been related to the energy measurement of the energy for a good quality sample of golden hybrid events to get rid of all of those assumptions. The calibration procedure requires a number of cuts to avoid biases due to threshold effects and noise due to badly reconstructed events. A set of quality cuts has been designed to have the calibration fit. They are:

- Cherenkov fraction below 50%.
- The tank with largest signal must be closer than 750 m to the shower axis.
- The reduced χ^2 of the Gaisser-Hillas fit must be below 4 and the χ^2 of a linear fit to the profile exceeds the χ^2 of the Gaisser-Hillas fit by at least 4.
- The shower maximum is required to be within the field of view and determined with an uncertainty below 50 g/cm^2.
- The uncertainty in the reconstructed energy must be below 40%.

for the fluorescence detector reconstruction and:

- The relative uncertainty in $N19$ must be below 40%.
- The inclined T5 quality trigger condition must be satisfied.

for the surface detector reconstruction.

This correlation has been used to obtain the relation between $N19$ and the calorimetric energy measured with the fluorescence detector using a linear fit in log scale ($\log_{10}(E[EeV]) = a + b\log_{10}(N19)$). This fit has been performed on a subsample of

almost 300 events assigning to each one the statistical uncertainties on both E_{FD} and $N19$. The values of the fitted parameters are:

$$\begin{aligned} a &= 0.84 \pm 0.01(stat) \\ b &= 1.01 \pm 0.03(stat) \end{aligned}$$

This correlation has been stable since the first presentation of this method when it was obtained with only 17 events. A study has been made of systematic effects of the cuts in the calibration curve.

Using this parameterization, the so-called calibration curve, the expected calorimetric energy of any event registered by the surface detector can be obtained. The energy resolution of the method has been estimated to be 21%. A global 22% of systematic uncertainty in the absolute scale must be kept in mind in spite of not being included in this analyses. It comes from the systematics in the FD energy measurement.

The energy saturation of the trigger efficiency that allows a geometrical calculation of the aperture has been evaluated from hybrid events. The threshold energy for full efficiency of the surface detector has been estimated in $10^{18.7}\ eV$.

The first energy spectrum using inclined events has been presented using more than 4 years of data with an incoming zenith angle between 60° and 80°. As a result, an evidence of a flux suppression around $5 \cdot 10^{19}\ eV$ has been found. The flux of cosmic rays has found to be not well described using an overall power-law. The first part of the spectrum ($18.7 < log(E[eV]) < 19.7$) has been fitted to a power-law ($J \propto E^{-\gamma}$) obtaining a spectral index of $\gamma = 2.70 \pm 0.02$. The number of events expected from the extrapolation of the power-law function $J \propto E^{-2.7}$ at higher energies has turned out to be 53 ± 2 for $log(E[eV]) > 19.7$ whereas the observed number has been 34 events. This flux suppression, combined with the correlation of arrival directions of the highest energy events with nearby AGN, supports the existence of the GZK cut-off but this claim will have to be confirmed with mass composition studies, a larger statistics and smaller systematic uncertainties.

Appendix A

Resumen de la tesis

Los rayos cósmicos son partículas relativistas que continuamente bombardean la Tierra desde todas las direcciones del Universo y con una energía que va desde $10^9\ eV$ hasta más de $10^{20}\ eV$. Fueron descubiertos a principios del siglo XX por Victor Hess quien tras una serie de vuelos en globo a gran altura, pudo comprobar que la velocidad de descarga de los electroscopios aumentaba con la altura en la atmósfera. Uno de los mayores retos para la física de astropartículas actual es el estudio de los rayos cósmicos de las más altas energías para descubrir su origen y su composición y medir con una alta precisión el espectro energético de estas partículas cuya energía supera en varios órdenes de magnitud la máxima energía alcanzable por los más modernos aceleradores de partículas.

El flujo de rayos cósmicos de ultra alta energía es extremadamente bajo (1 partícula por kilómetro cuadrado y por año por encima de $10^{19}\ eV$) y por tanto su detección conlleva grandes retos ya que la detección directa mediante detectores en globos o satélites es inviable. Ésta se realiza de forma indirecta a través de las cascadas de partículas que se producen por la interacción de los rayos cósmicos con la atmósfera que es usada como un calorímetro. En la colisión del rayo cósmico primario con una molécula del aire, la energía de aquél se distribuye entre las demás partículas generadas en la colisión. Éstas a su vez vuelven a interaccionar con la atmósfera y entre ellas produciéndose más y más partículas entre las que se distribuye una y otra vez la energía disponible. El conjunto de estas partículas que continuamente se propagan e interaccionan se conoce como cascada atmosférica. Las partículas viajan a una velocidad próxima a la de la luz en torno al eje de la cascada, que está definido por la dirección de incidencia del rayo cósmico que dio

lugar a la cascada, formando una estructura compleja denominada frente de la cascada.

Tradicionalmente se divide el conjunto de partículas que forman las cascadas atmosféricas en varias componentes: un zona central compuesta por hadrones de alta energía, una componente electromagnética formada por electrones, positrones y fotones, una componente muónica formada por los muones que provienen de la desintegración de mesones cargados y finalmente una componente de neutrinos. La detección de cascadas atmosféricas permite utilizar grandes áreas como detector salvando el escollo que supone el bajísimo flujo de rayos cósmicos de ultra-alta energía. Estas cascadas se pueden detectar haciendo uso de diferentes técnicas entre las que cabe destacar dos: la red de detectores de superficie y los detectores de fluorescencia. La primera técnica consiste en colocar una red de detectores en la superficie terrestre para así detectar las partículas de la cascada cuando llegan al suelo. La segunda técnica está basada en la observación de la tenue luz de fluorescencia emitida en el rango ultravioleta por las moléculas de nitrógeno atmosférico al desexcitarse después del paso de las partículas de la cascada atmosférica.

Los rayos cósmicos de ultra-alta energía generan diversos interrogantes como la existencia del llamado corte GZK. En 1996, poco después del descubrimiento del fondo de microondas, Greisen y Zatsepin y Kuzmin propusieron la existencia de un corte en el espectro energético de los rayos cósmicos en torno a $5 \cdot 10^{19}\ eV$ debido a su interacción con los fotones del mencionado fondo reduciendo así su energía en el camino desde sus fuentes a nuestro planeta. Una consecuencia inmediata de esta interacción con el fondo de microondas es la reducción de la distancia a la cual se pueden situar las fuentes de los rayos cósmicos de ultra alta energía. Éstas no se pueden situar a más de unos $50\ Mpc$ para protones de $10^{20}\ eV$ ya que la energía con la que llegarían a nuestros detectores desde mayores distancias sería mucho menor. Más aún, si las fuentes de estos rayos cósmicos están tan próximas a nosotros, los campos magnéticos presentes en la trayectoria de los mismos no podrían desviarlos notablemente desde su origen y deberían apuntar a sus fuentes dando lugar a una nueva astronomía de rayos cósmicos.

La zona del espectro relativa a las energías más altas ha sido estudiada por dos experimentos: AGASA en Japón y HiRes en los Estados Unidos. Cada uno ha usado una técnica de detección distinta: red de detectores en el primer caso y telescopios de fluorescencia en el segundo. Los resultados respecto a la existencia del mencionado corte GZK también han sido diferentes. De todos modos ninguno de los dos resultados puede

considerarse concluyente ya que ambos están limitados por los errores sistemáticos y por la baja estadística disponible. Con el fin de aumentar la misma de manera considerable y para reducir los errores sistemáticos asociados a la técnica de detección, nace a principios de los años 90 el enfoque híbrido presente en el observatorio de rayos cósmicos Pierre Auger.

A.1 El experimento Pierre Auger

El observatorio de rayos cósmicos Pierre Auger está dedicado a la detección de cascadas atmosféricas originadas por rayos cósmicos de ultra-alta energía con el objetivo de estudiar su dirección de llegada y su composición, así como a medir su espectro de energía. El experimento Pierre Auger es una colaboración internacional compuesta por más de 300 científicos pertenecientes a más de 30 instituciones de 16 países. El observatorio proporcionará una cobertura total del cielo mediante la construcción de dos detectores uno en cada hemisferio. El observatorio sur está ya construido en la provincia argentina de Mendoza y los primeros resultados científicos derivados del análisis de los sucesos detectados ya se han comenzado a presentar y a publicar. El observatorio norte se construirá en el estado de Colorado. El experimento Pierre Auger es un detector híbrido que hace uso simultáneo de las dos técnicas de detección mencionadas con anterioridad. La observación simultánea de las cascadas atmosféricas permite identificar los errores sistemáticos asociados a cada una así como realizar una intercalibración de las mediciones.

El detector de superficie está formado por una red de 1600 tanques de agua dispuestos en una red hexagonal con una distancia entre sí de $1500\ m$. Ocupa por tanto una superficie total de $3000\ Km^2$. Cada detector es un tanque de $3.6\ m$ de diámetro y $1.55\ m$ de altura lleno de $12000\ l$ de agua ultra pura. Cuando las partículas de la cascada llegan al suelo y atraviesan estos tanques emiten luz Cherenkov dentro de ellos que es detectada por tres fotomultiplicadores. La electrónica alimentada por un sistema de paneles solares y baterías digitaliza la señal y la envía por radio al sistema central de adquisición de datos en el que se decide si se ha detectado un suceso mediante la coincidencia espacio-temporal de las señales enviadas por cada uno de los tanques.

El detector de fluorescencia está formado por cuatro edificios u ojos que contiene cada uno 6 telescopios de fluorescencia y están situados alrededor del detector de superficie

observando la atmósfera sobre éste. Cada telescopio tiene una apertura de 28.6° en cenit y 30° en azimut. La luz de fluorescencia entra en el telescopio a través de un filtro y es reflejada en un espejo que la focaliza sobre una cámara formada por 440 fotomultiplicadores.

El concepto de detector híbrido que se plantea en el observatorio Pierre Auger permite usar medidas simultáneas de ambos detectores proporcionando medidas independientes de determinadas propiedades del rayo cósmico primario para controlar los errores sistemáticos de cada técnica por separado. Además, ambas técnicas se podrán usar de manera complementaria para obtener medidas más precisas de dichas magnitudes. El detector de fluorescencia, tiene un ciclo útil muy corto ya que sólo se puede usar en noches claras sin luna pero proporciona una medida calorimétrica de la energía del rayo cósmico primario que no requiere ninguna suposición sobre la naturaleza de la partícula primaria. Por el contrario, el detector de superficie, con un ciclo útil próximo al 100% proporcionará la alta estadística necesaria para reducir los errores estadísticos debidos al bajo flujo de los rayos cósmicos de ultra-alta energía.

Dependiendo del ángulo respecto a la vertical con que llegue la cascada atmosférica detectada se hace una clasificación en sucesos verticales (ángulo cenital menor de 60°) y sucesos inclinados (ángulo cenital mayor de 60°). Las diferencias entre ambas se deben básicamente a la profundidad atmosférica que tienen que atravesar hasta llegar a la superficie y que hace que la composición del frente de la cascada sea muy diferente en uno y otro caso. En el primero de ellos, la mayoría de las partículas son electrones, positrones y fotones y las señales mantienen una simetría radial respecto del centro de la cascada que permite definir una función que mide la dependencia de la señal respecto a la distancia al core de la cascada. Esta función se denomina función de distribución lateral. Por el contrario, para sucesos inclinados, el frente de la cascada está compuesto principalmente por muones debido a la atenuación sufrida por la componente electromagnética de la cascada. Además, y debido a las grandes distancias recorridas por las partículas desde su punto de producción, el campo magnético terrestre actúa como un espectroscopio curvando sus trayectorias y haciendo que se pierda la simetría radial de la señal en torno al eje de la cascada. La función de distribución lateral no tiene sentido y una función bidimensional es necesaria para describir el comportamiento del número de partículas (o de la señal) con la distancia.

Esta y otras diferencias, hacen que los métodos de reconstrucción de la dirección de

llegada, del punto de impacto y de la energía sean diferentes para cascadas inclinadas que los tradicionalmente empleados en cascadas verticales. En esta tesis se ha expuesto un método completo de reconstrucción y análisis de sucesos inclinados detectados con el detector de superficie del observatorio Pierre Auger. En el capítulo 3 se muestra un método para la reconstrucción de la dirección de llegada así como un análisis del modelo utilizado para la varianza de los tiempos de llegada de las partículas a los tanques. El capítulo 4 está dedicado a la reconstrucción del punto de impacto de la cascada y de su energía. Se muestran las dos técnicas utilizadas y se dedica una sección a la importante tarea de la calibración del parámetro que mide el tamaño de la cascada con la energía medida calorimétricamente con el detector de fluorescencia. En el capítulo 5 se obtiene el flujo de rayos cósmicos a partir de sucesos inclinados y en el capítulo 6 se muestran las conclusiones de este trabajo.

A.2 Reconstrucción angular de sucesos inclinados

La reconstrucción de la dirección de llegada del rayo cósmico con el detector de superficies se realiza a partir de los tiempos de llegada del frente de la cascada a las estaciones del detector de superficie. Para ello se ajustan los tiempos de llegada a unos tiempos esperados según un modelo dado para el frente de la cascada. Este ajuste se realiza mediante una minimización de la función χ^2 en la cual es de crucial importancia la varianza en los tiempos de llegada ya que puede introducir sesgos en la dirección de llegada reconstruida.

Para estudiar esta varianza se ha hecho uso de pares de estaciones presentes en la red de tanques que forman el detector de superficie y que al estar colocados muy próximos (unos $10\ m$) se puede asegurar que miden la misma zona del frente de la cascada atmosférica. Al medir la misma zona de la cascada, las diferencias entre los residuos del ajuste para estas dos estaciones no dependen del modelo del frente usado en el mismo, sino que dependen en exclusiva de la varianza en los tiempos de llegada del frente a los tanques. Estudiando estas diferencias se ha validado el modelo para la varianza usado en este trabajo.

En el capítulo 3 de este trabajo se encuentra descrito todo este proceso, así como el análisis y la validación del modelo utilizado para la varianza en los tiempos de llegada de la señal a los tanques del detector y una primera evaluación de la resolución angular

del detector de superficie con sucesos inclinados haciendo uso de sucesos híbridos.

A.3 Reconstrucción del punto de impacto y de la energía de sucesos inclinados

Al igual que la dirección de llegada del rayo cósmico primario se obtiene mediante una comparación entre los tiempos de llegada del frente de la cascada a los tanques del detector de superficie y un tiempo teórico obtenido de un modelo para la propagación de este frente, el punto de impacto de la cascada y su energía se obtienen mediante la comparación de las señales medidas en los tanques con unas señales esperadas. Estas señales teóricas, que dependen de los dos parámetros que queremos reconstruir, se obtienen a partir de simulaciones de la distribución del número de partículas en torno al eje de la cascada y de la simulación de la señal producida por el paso de las mismas a través de un tanque del detector de superficie.

Como ya se ha comentado, debido al gran espesor de atmósfera que atraviesan las cascadas horizontales hasta llegar al suelo, su componente electromagnética es atenuada prácticamente en su totalidad siendo la componente muónica la que domina la señal producida en los tanques. Se utilizarán por tanto a la hora de calcular las señales esperadas distribuciones de la densidad de muones alrededor del eje de la cascada denominándose estas distribuciones mapas de muones. La forma de estos mapas es prácticamente independiente de la naturaleza del rayo cósmico primario y de su energía y sólo su normalización global depende de estos parámetros. Este factor de normalización denominado N19 será el que mida el tamaño de la cascada detectada y será correlacionado con la medida calorimétrica de la energía que proporciona el detector de fluorescencia mediante el uso de sucesos detectados simultáneamente con ambas técnicas.

Para obtener el factor de normalización $N19$, en primer lugar obtenemos la señal que producirían estos muones al atravesar un tanque del detector de superficie. Hecho esto, añadiremos a esta señal la correción debida a la componente electromagnética. Ésta se debe a la parte de la componente electromagnética de la cascada que no se ha atenuado y a otros procesos como puede ser la desintegración de los muones. De este modo obtendremos la señal total esperada. Por último compararemos esta señal esperada con la que se mide en cada uno de los tanques. Además, se utilizan en estas

comparaciones una serie de tanques que no han detectado ninguna señal para confinar de manera adecuada la posición del punto de impacto. Dos técnicas son utilizadas de manera consecutiva para la obtención de $N19$. En primer lugar, se elige como punto de impacto la posición en una red en torno al baricentro de las señales detectadas que minimice una función χ^2. El valor de $N19$ se obtiene sin más que buscar un mínimo de dicha función con respecto a $N19$. En segundo lugar, se maximiza la función *Likelihood* que nos da la probabilidad de que cada estación tenga la señal medida cuando se espera otra que viene dada por los valores de $N19$ y de la posición del tantque con respecto al punto de impacto de la cascada. Estos dos procesos están explicados detalladamente en el capítulo 4 de este trabajo.

A.3.1 Calibración en energía

Una mención propia se merece el proceso de calibración en energía. Éste permite asignar a cada suceso recogido por el detector de superficie la energía que le correspondería de haber sido detectado por el detector de fluorescencia. La medida de la energía por el detector de fluorescencia es una medida calorimétrica y por tanto no necesita hipótesis sobre la composición de la partícula primaria ni depende de modelos hadrónicos. Su mayor fuente de incertidumbre es el denominado *fluorescence yield* que da el número de fotones emitidos por energía depositada.

Para realizar el proceso de calibración, se ha hecho uso de una serie de sucesos híbridos (que son detectados y reconstruidos por cada detector de forma independiente) de alta calidad y se ha correlacionado la medida de la energía del detector de fluorescencia con el tamaño de la cascada reconstruido por el detector de superficie (N19). Esta correlación entre ambas magnitudes se denomina curva de calibración y para su obtención se ha realizado una serie de cortes para garantizar la alta calidad de los sucesos así como para evitar la introducción de un sesgo debido a los sucesos de baja energía que puede alterar todo el proceso de calibración. Este sesgo es producido por el hecho de que la saturación de la eficiencia de detección es menor para el detector de fluorescencia que para el detector de superficie, haciendo que en la zona de bajas energías sólo estén presentes fluctuaciones hacia arriba del tamaño de la cascada.

La resolución en energía del proceso se ha estimado en un 21% y su estabilidad ha sido estudiada frente a diversos factores como el detector de fluorescencia que mide la

energía del suceso o los cortes empleados para la selección de los mismos.

A.4 Espectro de energía de los rayos cósmicos usando sucesos inclinados

Para la determinación del flujo de rayos cósmicos una vez establecida la energía de cada suceso detectado, sólo es necesario calcular la exposición del detector de superficie. Por encima de la energía de saturación del trigger (energía para la que el detector es 100% eficiente), la exposición se vuelve totalmente geométrica y sólo es necesario calcular el área del detector y el tiempo que está activo. Este cálculo es muy sencillo gracias a unos archivos de trigger local que guardan la información sobre las estaciones del detector activas en cada segundo. A partir de esta información podemos calcular directamente el área total activa cada segundo y sumando para todo el periodo de tiempo en el que se recogen datos, podemos calcular la exposición total.

La parte del flujo de rayos cósmicos correspondiente a las energías más bajas, parece ajustarse a una ley de potencias ($J\ E^{\gamma}$) con un índice espectral de $\gamma = -2.7$. Si extrapolamos esta ley a las energías más altas, se observa una deficiencia de sucesos con respecto a los que cabría esperar. Esta supresión es una evidencia de la existencia del mencionado corte GZK.